A GAUSSIAN PROCESS-BASED MULTI-SENSOR METROLOGY SYSTEM FOR PRECISION MEASUREMENT OF FREEFORM SURFACES

LIU MINGYU

Ph.D

The Hong Kong Polytechnic University

2018

The Hong Kong Polytechnic University

Department of Industrial and Systems Engineering

A Gaussian Process-Based Multi-Sensor Metrology System for Precision Measurement of Freeform Surfaces

Liu Mingyu

A thesis submitted in partial fulfilment of the requirements for the degree of Doctor of Philosophy

July 2017

CERTIFICATE OF ORIGINALITY

I hereby declare that this thesis is my own work and that, to the best of my knowledge and belief, it reproduces no material previously published or written, nor material that has been accepted for the award of any other degree or diploma, except where due acknowledgement has been made in the text.

_____(Signed)

Liu Mingyu (Name of student)

Abstract

Nowadays, precision freeform surfaces play an important role since they have superior performance and indispensable functionalities. Due to their geometrical complexity, high form accuracy and low surface roughness, precision freeform surfaces introduce a lot of research challenges in precision manufacturing and measurement processes. This is particularly true when the measurement is performed on traditional off-line single-sensor instruments such as white light interferometers (WLIs) and coordinate measuring machines (CMMs) whose measurement abilities are limited.

For a single-sensor instrument, the measurement range and measurement resolution always need to strike a balance since the two terms appear to be contradictory. Moreover, when the workpiece is extremely large and error compensation procedure is needed to correct the form error of the workpiece, it is necessary to perform the measurement on machining facilities since repositioning error is unacceptable. However, off-line based measurement instruments cannot fulfil the in-situ measurement requirement.

To address the above issues, this research firstly established a generic Gaussian process data modelling and image registration-based stitching method for the measurement of precision freeform surfaces based on traditional single-sensor surface measurement instruments using multiple measurement methods. With the proposed method, a dataset with a large measurement range and high resolution can be obtained. The proposed stitching method provides a turn-key solution for high dynamic range measurement using single-sensor instruments with a multiple measurement method.

For multi-sensor instruments such as multi-sensor coordinate measuring machines (CMMs), this study proposes a Gaussian process-based data modelling and maximum likelihood data fusion method for the measurement of freeform surfaces for multi-sensor CMMs. The method utilizes an optical sensor such as laser sensor and a touch trigger probe mounted on the multi-sensor coordinate measuring machine for the measurement of freeform surfaces, and the measurement data are modelled using the Gaussian process modelling method. The combination of different kinds of sensors balances the measurement efficiency and accuracy since most optical sensors have a fast measurement speed and high density but low accuracy while contact sensors have an accurate measurement result but low efficiency. The measurement datasets from the laser sensor and touch trigger probe were fused with a maximum likelihood method so as to reduce the overall measurement uncertainty.

To address the in-situ measurement issue, this thesis proposes an autonomous multi-sensor in-situ metrology system for high dynamic range measurement of freeform surfaces for precision machine tools. The system utilizes a laser scanner and a motion sensor together with a designed trajectory so as to perform in-situ measurement on the machining facilities. The proposed system is independent of the machining facilities which makes it extendable to a wide range of industrial applications. Based on the theory developed for the autonomous multi-sensor in-situ metrology system, a homogeneous multi-sensor in-situ measurement metrology system was developed equipped with a laser line sensor and laser point sensor. The laser line sensor provides high lateral resolution data while the laser point sensor gives accurate data. The measurement data from these two kinds of sensors are fused to obtain a more accurate result without losing the high lateral resolution.

The present study has very large potential applications in industry. The successful development of the Gaussian process and image registration-based stitching method provides an important means for high dynamic range measurement, while the Gaussian process-based data modelling and maximum likelihood-based data fusion method establishes a generic measurement strategy for multi-sensor coordinate measuring machines so as to improve the measurement accuracy for precision freeform surfaces. The proposed in-situ multi-sensor high dynamic range measurement method and hence the homogeneous multi-sensor in-situ metrology system enable the measurement ability of machine tools so as to improve the efficiency and accuracy of the precision manufacture of complex freeform surfaces. The outcome of the research contributes significantly to the measurement science and technology, especially in the field of multi-sensor measurement and in-situ measurement of precision freeform surfaces.

Publications arising from this study

Refereed Journal papers

Liu, M. Y., Cheung, C. F., Ren, M. J., & Cheng, C. H. (2015). Estimation of Measurement Uncertainty Caused by Surface Gradient for a White Light Interferometer. *Applied optics, 54*(29), 8670-8677. (SCI Indexed)

Liu, M. Y., Cheung, C. F., Whitehouse, D. J., & Cheng, C. H. (2016). An Autonomous Multisensor in Situ Metrology System for Enabling High Dynamic Range Measurement of 3D Surfaces on Precision Machine Tools. *Measurement Science and Technology, 27*(11), 115015. (SCI Indexed)

Liu, M. Y., Cheung, C. F., Cheng, C. H., & Lee, W. B. (2016). A Gaussian Process Data Modelling and Maximum Likelihood Data Fusion Method for Multi-Sensor CMM Measurement of Freeform Surfaces. *Applied Sciences, 6*(12), 409. (SCI Indexed)

Liu, M. Y., Cheung, C. F., Ren, M. J., Cheng, C. H., Kong, L. B., & Lee, W. B. (2016). A Framework of Data Fusion Algorithm for Precision Measurement of Multiscale Surfaces. *Key Engineering Materials, 679*, 155-161. (EI Indexed)

Liu, M. Y., Cheung, C. F., Cheng, C. H., Su, R., & Leach, R. K. (2017). A Gaussian Process and Image Registration Based Stitching Method for High Dynamic Range Measurement of Precision Surfaces. *Precision Engineering – Journal of the International Societies for Precision Engineering and Nanotechnology*, 50, 99-106. (SCI Indexed)

Refereed International Conference papers

Liu, M. Y., Cheung, C. F., & Ren, M. J. (2015). Characterization of Directional Features for Precision Surfaces using Curvelet. *Proceedings of the American Society for Precision Engineering's 30th Annual Meeting (ASPE2015)*, November 1-6, Austin, Texas, USA, 515-520.

Liu, M. Y., Cheung, C. F., & Ren, M. J. (2015). A Study of Gaussian Process and Image Registration based Stitching for High Dynamic Range Measurement of Precision Surfaces. *Proceedings of 6th International Conference of the Asian Society for Precision Engineering and Nanotechnology (ASPEN2015)*, August 15–20, Harbin, China, CD version.

Liu, M. Y., Cheung, C. F., & Li, Z. (2016). A Gaussian Process based Data Modelling and Fusion Method for Multisensor Coordinate Measuring Machines. *Proceedings of the American Society for Precision Engineering's 31th Annual Meeting (ASPE2016)*, October 23-28, Portland, Oregon, USA, 179-183.

Liu, M. Y., Cheung, C. F., & Chen, S. S. (2016). A Rotational Stitching Method for Measuring Cylindrical Surfaces. *Proceedings of the 15th International Conference of the European Society for Precision Engineering and Nanotechnology*, May 31-June 3, Nottingham, UK, CD version.

Liu, M. Y., Cheung, C. F., & Zhao, C. Y. (2016). Multi-sensor CMM Measurement of Freeform Objects with Sharp Features. *Proceedings of the 5th International Conference on Nanomanufacturing (nanoMan2016)*, August 15-17, Macau, electronic version.

Liu, M. Y., Cheung, C. F., & Yang, S. M. (2017). A Study of Extrapolation of Freeform Surfaces to Improve the Edge Effect in Surface Filtering. *Proceedings of ASPEN/ASPE Spring 2017 Topical Meeting Manufacture and Metrology of Structured*

and Freeform Surfaces for Functional Applications. March 14-17, Hong Kong, electronic version.

Patents

Liu, M. Y., Cheung, C. F., Lai, K. T., & Ho, L. T. (2016). A Method for On-machine Multi-sensor High Dynamic Range Measurement of Freeform Surfaces, Chinese patent, filed, Application no: 201610044554.0.

Acknowledgement

First of all, I would like to express my sincerely thanks to my chief supervisor - Prof. Benny Cheung for providing me the chance to pursuit of my Ph.D. study and his continuous guidance and support for the research work. Prof. Cheung taught me a lot of things including how to formulate research problems, how to conduct experiments, how to solve problems and how to deal with uncertainties (both in measurements and in life). Most importantly, his rigorousness and high standards have influenced me not only in research but also in my everyday life.

The work could not have been completed as smoothly as it was without the guidance from Dr. C. H. Cheng and Prof. W. B. Lee, who are my co-supervisors. The discussions with them were very enjoyable and I would like to take this opportunity to express my sincere thanks to them. I would also like to thank Dr. Johnny M. J. Ren, Lecturer in Shanghai Jiaotong University and Prof. Boby L. B. Kong, Professor of Fudan University for their support and help provided for my research. Special thanks are also given to Prof. Richard Leach and Dr. Rong Su from the University of Nottingham, UK for their support and concerns, especially for their help when I was an exchange student in their laboratory. I thank the Research Office of Hong Kong Polytechnic University for its financial support (account code: RTHC).

Deepest thanks are also given to my wife, Dr. Lily H. L. Cao, who always understands and supports me by my side no matter what happens. I would also like to thank my parents, and my sister for their kind understanding despite having spent little time with them in the busy research life.

Table of contents

List of figures

List of tables

Chapter 1 Introduction

1.1 Background of the study

Manufacturing and measurement of workpieces with complex freeform surfaces has long been a focus of study especially in the industries of die moulds (Altan et al., 2001), turbine blades (Veers et al., 2003), automotive (Chen et al., 2002), aerospace (Campbell, 2011), bio medical (Murr et al., 2009) and optics (Fang et al., 2013b). This is due to the fact that complex freeform surfaces provide significant improvement in terms of energy efficiency, optical performance, compact size and superb functional achievement, etc. (Savio et al., 2007). With increasing demands of the industries and the development of science and technology, the requirement of the freeform parts is becoming more and more stringent including larger size, higher form accuracy, better surface roughness and more complex surface features such as multiscale features (Jiang et al., 2007c).

The stringent requirements of freeform surfaces bring a lot of challenges not only to the machining process but also to the measurement process. For a large workpiece which may be metres large in size but with small features of several micrometres (Shore and Morantz, 2012), it is necessary to measure the whole workpiece and the small features at the same time. This raises a great challenge in a high dynamic range (HDR) measurement where the measurement should have a large measurement range and a high lateral resolution (Leach et al., 2013). For traditional measurement instruments, especially for those optical instruments that use CCD/CMOS as a capturing device, these two requirements are contradictory since the spatial resolution of the CCD/CMOS in the instruments is fixed; when the measurement range is increased, the lateral resolution is reduced, and vice versa. To

meet the high dynamic range requirement, one possible method is to perform the measurement multiple times and stitch the data together to form a holistic surface which covers the whole workpiece without losing the required resolution at the same time (Wang et al., 2015).

For surface stitching, most of the traditional stitching methods have large rotational stitching error especially when the number of the original measurement datasets is large since the rotational error accumulates significantly with increasing measurement data. The measurement noise of the original measurement dataset also largely affects the stitching accuracy while the transition area always has discontinuity which may be caused by the lack of a suitable data fusion process. On the other hand, most of the traditional dimensional measurement instruments only have a single sensor installed and its measurement ability is largely affected by the sensor's characteristics. For example, the CMM machine with a touch trigger probe has slow measurement speed, although the measurement accuracy is supposed to be high and reliable. A laser sensor, which has a fast measurement speed, is a convenient measurement device as it measures workpieces using a non-contact measurement method. Combining multiple sensors in a measurement task can make use of the strength of different sensors, and the measurement ability, reliability and accuracy are significantly improved.

Nowadays, there are many commercially available multi-sensor CMM machines which are equipped with many different kinds of sensors such as touch trigger probe, image sensor, laser scanner, fibre probe, white light distance sensor, etc. (Hexagon, 2016, Carl Zeiss Industrial Metrology, 2016, Werth Messtechnik GmbH, 2016). The measurement ability has been largely improved by integrating different kinds of sensors to perform holistic measurement. However, most of the measurement methods only enhance the performance improvement according to the characteristic

of the sensor itself. Only few studies focus on the multi-sensor measurement strategy to further improve the overall accuracy, which is a research trend towards higher measurement accuracy. Moreover, a generic data modelling and data fusion method is much needed for multi-sensor measurement machines. The limitations need to be highlighted during the development of a multi-sensor data fusion method for dimensional measurement.

To address the in-situ measurement and high dynamic range measurement issues, one solution is to install the measurement instruments onto the machining facilities to perform the measurement task (GF AgieCharmilles, 2015, Zeeko Ltd, 2010). With the measurement instruments installed on the machining facilities, the measurement can be performed in situ on the machines and there is no need to take the workpiece for offline measurement. By incorporating the measurement process onto the machining facilities, the instruments can be moved along with the motion axes of the machine, and the measurement range can be significantly enlarged by the motion of the axes. Since most of the motion control systems of the machines are closed and cannot be accessed by most of the users and researchers, it is difficult to obtain the coordinate information of the axes and it is difficult or sometimes impossible to perform holistic measurement for workpieces. As a result, it would be a great advantage to accurately estimate the coordinate information of the axes without accessing the motion control system of the machines.

Although some researchers have studied the position estimation by using motion sensors (Latt et al., 2011), the implementation for precision machines is seldom seen in the literature and the accuracy is still in question. With the development of an autonomous in-situ metrology system, the position estimation method is convenient for research and development, considering that the measurement method is

independent of the machine control system. It provides solutions to an ultra-wide range of applications which can enhance the measurement ability of the machines. To estimate the position information, additional sensors and special motions should be investigated. Moreover, a more sophisticated method should be studied and developed to improve the accuracy of the estimated position.

Moreover, most of the multi-sensor instruments are off-line measurement instruments while most of the in-situ measurement instruments are single-sensor measurement instruments. There is a large research gap regarding research on in-situ multi-sensor measurement instruments especially when the data modelling method and data fusion method are considered. The research trends toward in-situ measurement and multi-sensor data fusion technology are a promising research area to develop multi-sensor in-situ surface measurement instruments which can possibly meet all the most challenging measurement requirements such as high accuracy, high resolution, high speed and high robustness.

1.2 Research objectives and significance

To address the issues for the measurement of precision freeform surfaces with high dynamic range requirement and specially for multi-sensor CMM machines and for the in-situ high dynamic range measurement for precision freeform surfaces, this research aimed to study the new stitching and data fusion method for surface measurement and develop a measurement method for multi-sensor CMM measurement and in-situ measurement method for precision machine tools, together with the development of a multi-sensor in-situ surface measurement instrument. The objectives of this study are given as follows:

(i) To develop a stitching method for high dynamic range measurement of precision freeform surfaces for multiple measurement of single-sensor instruments.

(ii) To develop a Gaussian process data modelling and maximum likelihood data fusion method to model the measurement data and fuse them together to further increase the measurement accuracy.

(iii) To develop an in-situ metrology system for high dynamic range measurement for precision freeform surfaces on precision machine tools.

(iv) To develop a multi-sensor in-situ surface measurement instrument equipped with the proposed data modelling and data fusion method together with in-situ measurement ability.

As the research and development aimed to achieve the above objectives, the significance of this study is summarised as follows:

(i) Development of a generalized data modelling and stitching method for high dynamic range measurement of precision freeform surfaces for multiple measurement with single sensor instruments. This work is published as in Liu et al. 2017 in Precision Engineering.

(ii) Development of a generic data modelling and data fusion method for multi-sensor measurement for precision freeform surfaces. This work is published as in Liu et al. 2016 in Applied Sciences.

(iii) Establishment of an in-situ multi-sensor metrology system which is capable of high dynamic range measurement of precision freeform surfaces without the need of communicating with the motion controller of the machine tool. This work is published as in Liu et al. 2016 in Measurement Science and Technology.

(iv) Establishment of a multi-sensor metrology system to fill the research gap of the implementation of in-situ measurement principle of multi-sensor data fusion.

1.3 Organization of the thesis

The thesis is composed of six chapters. Chapter 1 is the introduction of the whole thesis which introduces the background of this study and states the aims and objectives of this research, and it gives an overview of the organization of this thesis. Chapter 2 gives a thorough literature review related to the research including the development of precision freeform surfaces and their applications, the machining technologies for precision freeform surfaces, the measurement technologies for precision freeform surfaces. The review of the measurement technologies is divided into single-sensor measurement systems, multi-sensor measurement systems, in-situ/in-process measurement systems and high dynamic range measurement systems. The measurement uncertainty and traceability are also reviewed and followed by a summary section at the end.

In Chapter 3, a Gaussian process and image registration-based stitching method is proposed for high dynamic range measurement of precision freeform surfaces. The method utilizes the Gaussian process data modelling method to model the original measurement dataset which aims to increase the registration accuracy in the following step. Hence, the datasets are projected to the X-Y plane, and the original measurement datasets are thus transformed to 2D images. An image registration method is used to register the 2D images and *z* axis alignment is performed. The overlapped area is fused together by using an edge intensity method so as to obtain a smooth transition.

Chapter 4 introduces a Gaussian process-based data modelling and maximum likelihood-based data fusion method for multi-sensor instruments purposely developed

for multi-sensor CMMs. The method starts with the measurement of the workpiece by the laser sensor and the touch trigger probe. The measurement data are then modelled by using the Gaussian process. The mean surfaces and the associated uncertainties for both measurements are obtained and the datasets are fused with the maximum likelihood principle to generate a more accurate result. A series of experiments were conducted to verify the proposed method and the limitation of the proposed method is also discussed.

Chapter 5 reports an in-situ metrology system developed for high dynamic range measurement of freeform surface on precision machine tools. The system was designed, developed and demonstrated on a precision polishing machine tool. Experiment shows that the metrology system measures freeform surface with high resolution. The measurement range is large since the metrology system can be moved with the motion axes of the machine tool. Moreover, the system is independent of the control system of the machine tool which makes it widely expandable to industry where most of the interface of the machine tools is not open to users and researchers.

Chapter 5 also presents a homogenous multi-sensor in-situ metrology system which incorporates two kinds of developed in-situ metrology systems which are line sensor-based and point sensor-based, together with the proposed Gaussian process data modelling and maximum likelihood data fusion method. Experimental procedures are given in detail to demonstrate that the fusion result has better measurement accuracy and high lateral resolution. The establishment of the newly proposed metrology system also successfully demonstrates the promising multi-sensor data fusion technology implemented in an in-situ measurement environment. Finally, an overall conclusion of the thesis and some suggestions for future studies are discussed in Chapter 6.

Chapter 2 Literature review

2.1 Introduction

In this chapter, an extensive literature review is presented which includes the evolution of freeform surfaces and their applications, the machining techniques of precision freeform surfaces and the development of metrology technology for the measurement of freeform surfaces. The review of the measurement technology is discussed in detail which is divided into single-sensor measurement systems, multi-sensor measurement systems, in-situ/in-process measurement systems and high dynamic range measurement. The methods for measurement uncertainty and traceability are also reviewed. The development trends and the limitations of the current measurement technology are discussed and a summary is given at the end.

2.2 Precision freeform surfaces and their applications

Simple geometrical shapes such as planes, spheres and cylinders are the basic components of traditional industrial parts which provide the functionalities for products. Unlike conventional simple surfaces which usually possess rotational and translational symmetry, by definition, freeform surfaces or complex surfaces are surfaces without rotational or translational invariance (ISO/TS 17450-1, 2005). Structured surfaces such as V-grooves, micro-lens arrays and micro-pyramids are also freeform surfaces (Jiang et al., 2007a). The freeform surfaces are introduced along with the development of science and technology and have a long history. Compared with a simple surface, freeform surfaces provide superior functionality and performance (Jiang et al., 2007b) and they are now widely used in many industries such as aerospace, automotive, optics, biomedical, etc.

One of the most important attributes of freeform surfaces is their aerodynamic performance for moving objects such as airplanes, cars and wind turbine blades. With careful design with computational simulation together with the technologies for manufacturing and measurement of precision freeform surface, the drag coefficient is significantly reduced since the flow condition can be significantly improved with purposely-designed continuous freeform surfaces. The use of freeform surface in these industries has been proven to be of great significance to reduce cost and carbon dioxide emissions.

Moreover, a lot of research has been focused on the design and optimization of freeform surfaces to improve aerodynamic performance. For instance, one of the most challenging goals in airplane design is to increase aerodynamic performance (Jameson, 1989). In order to reduce the aerodynamic resistance which results in better economic and environmental friendliness, the design of the wings and the fuselage are freeform parts with complex surfaces. The aerodynamic design of an airplane usually takes partly in computational fluid dynamics (CFD) simulations and experiments in wind tunnels to test the performance. Figure 2.1 shows a complete model in a wind tunnel for experimental evaluation of the design of the mega liner A380 from Airbus.

Figure 2.1 A complete model of airplane in the wind tunnel (Reckzeh, 2003)

For automobiles, it has been reported that 40%, which is a significant amount of drag coefficient, comes from the shape of the vehicle (Hucho and Sovran, 1993). Improvement of the aerodynamic design can greatly reduce the drag coefficient. As a result, research on this area has become a hot topic in car design. To improve aerodynamic performance, freeform car shapes' design and optimization are much needed and this was commonly seen in the high-end car market in the past. However, most of the cars, even the economy class, have freeform designed shapes to improve aerodynamic performance and this has significant impact on reducing carbon dioxide emissions. Figure 2.2 shows the simulation result of streamlines around a stock car.

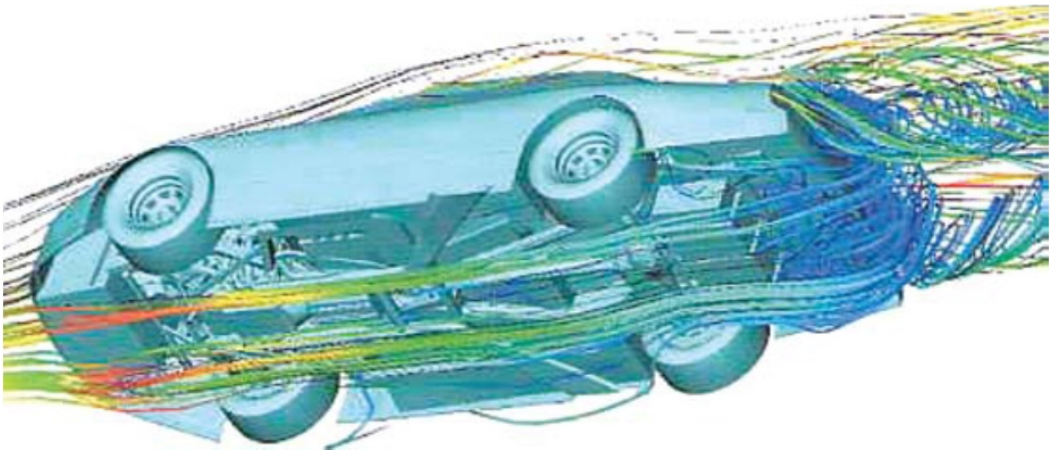

Figure 2.2 Aerodynamic simulation of cars (Katz, 2006)

It is reported that about 15-20% of the wind turbine production cost comes from the cost of manufacturing the wind turbine blades (Jureczko et al., 2005). The shape of the wind turbine blade is designed to be a freeform surface so as to increase its aerodynamic efficiency. Due to the large size of wind turbine blades, the design, manufacturing, measurement and testing are a challenge. Figure 2.3(a) shows a picture of a modern wind turbine from Siemens and Figure 2.3(b) shows the testing environment for a wind turbine.

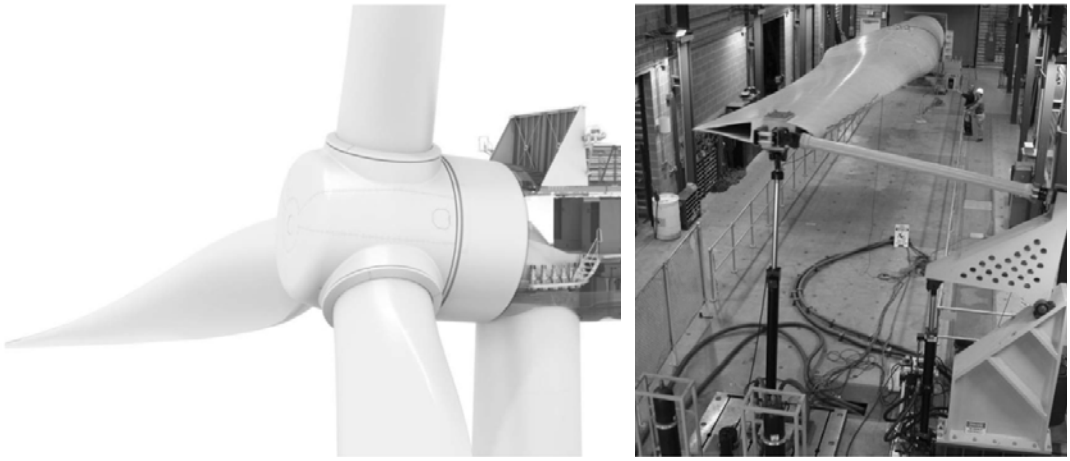

(a) A modern Siemens wind turbine *(b) Testing of a wind turbine*

Figure 2.3 Freeform surfaces of the wind turbines (Hansen, 2015, Veers et al., 2003)

Freeform surfaces are also widely used in biomedical implant applications since most of the parts of the human body are freeform shapes (Curodeau et al., 2000). For example, the replacement of hip and knee in biomedical applications requires the polishing and correction of freeform surfaces since these surfaces in the human body are typically freeform shapes (Charlton and Blunt, 2008). The surface accuracy and surface finishing of these implants impose stringent requirements and they are usually made of difficult-to-machine material due to their bio-capability. Figure 2.4 shows total hip replacement and total knee replacement.

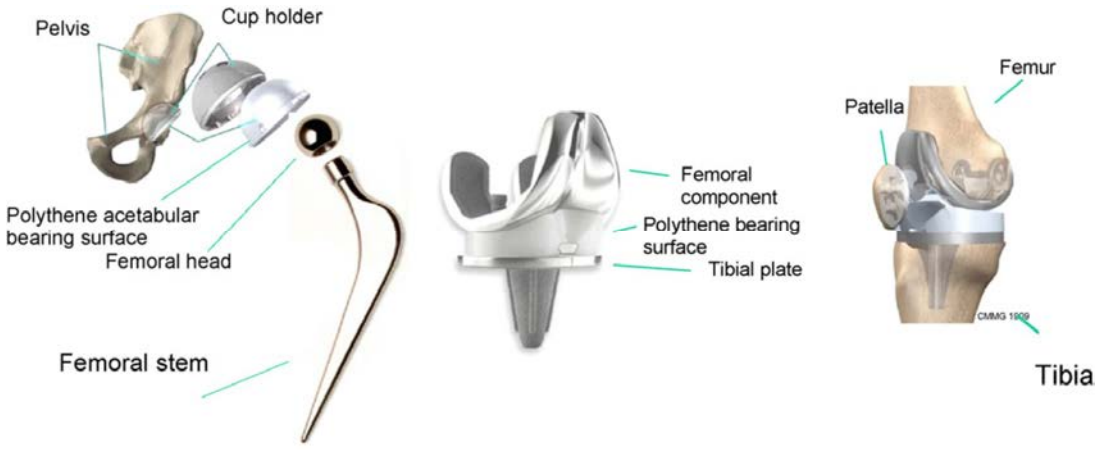

Figure 2.4 Total hip and total knee replacement (Blunt et al., 2009)

Moreover, freeform surfaces are widely used in advanced optics since optical performance can be significantly improved and the size of the optical system can be greatly reduced. There are a lot of applications of freeform surfaces in optics. One example is the imaging system. The Polaroid SX-70 folding Single Lens Reflex camera (Plummer, 2005) was a well-known successful commercial product in the early days which deployed freeform optic design in 1972 to correct the field tilt, the astigmatic error across the view scene and localize the apparent power. Figure 2.5(a) shows the system and Figure 2.5(b) shows the optical path of the camera.

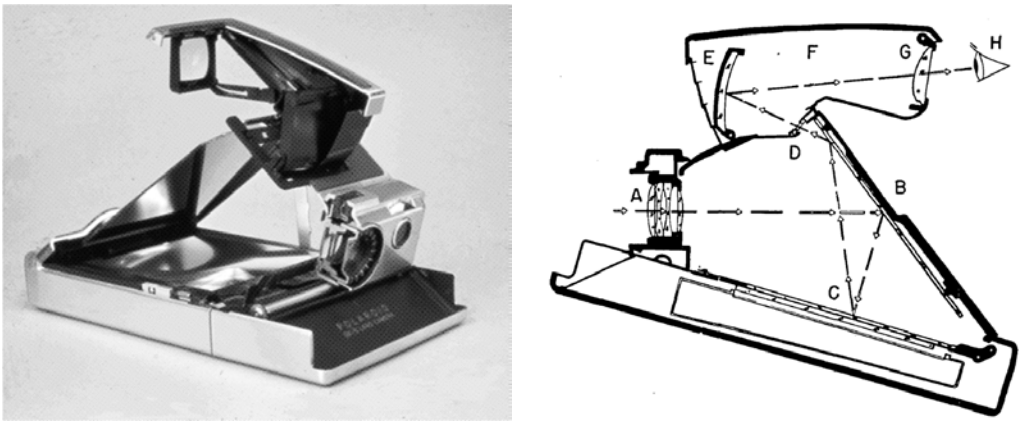

(a) The system *(b) Diagram of the optical route*

Figure 2.5 Polaroid SX-70 folding Single Lens Reflex camera (Plummer, 2005, Plummer, 1982)

Another example of advanced optics is the f-theta lens which is a freeform surface widely used in high-end scanners (Takahashi et al., 2005), 3D displays (Wang et al., 2010), 3D imaging (Jin et al., 2014), and laser machining (Araki et al., 2009). Figure 2.6 shows some of the applications of the f-theta lens. Figure 2.6(a) shows a volumetric 3D display utilizing a diode laser to project a fast scanning X-Y galvanometer with an f-theta lens. Figure 2.6(b) shows a high-speed THz reflection tomography system which makes uses of a telocentric f-theta lens for beam steering

while Figure 2.6(c) shows a 2D optical lens scanner with an integrated f-theta lens. Figure 2.6(d) shows an f-theta lens used for UV laser machining which has diffraction-limited performance.

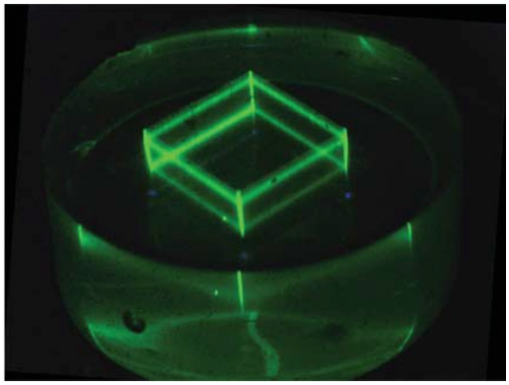

(a) 3D display

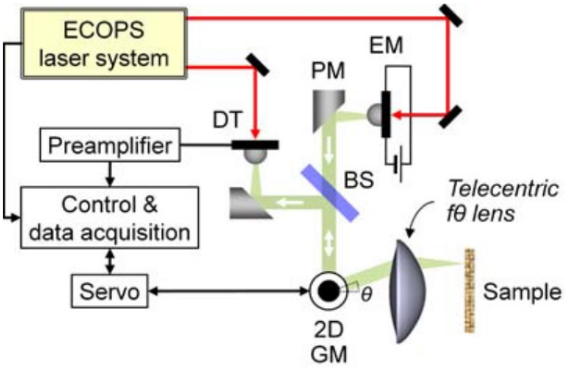

(b) 3D imaging

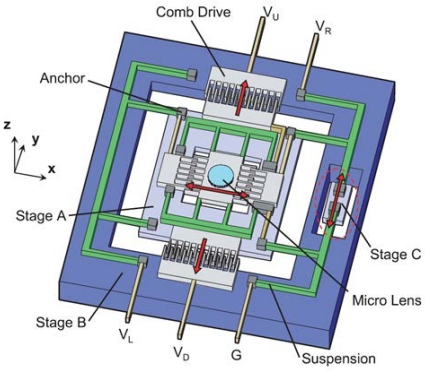

(c) Scanner

(d) Laser drilling

Figure 2.6 Applications of f-theta lens (Wang et al., 2010, Jin et al., 2014, Takahashi et al., 2005, Araki et al., 2009)

Freeform optics also have applications in the optometric field. One example is the freeform progressive addition lens (PAL) which contains a far view zone, a near zone and a progressive zone between the far and near zones (Kong et al., 2014, Li et al., 2013). It is becoming popular in the market for optometric applications. Figure 2.7

shows the machined PAL mould inserts with a freeform surface (Figure 2.7(a)) and an aspheric surface (Figure 2.7(b)).

(a) A freeform mould insert

(b) An aspheric mould insert

Figure 2.7 Machining of PAL mould inserts (Kong et al., 2014)

Freeform optics are also widely used in the illumination systems to improve the efficiency of light transfer or reduce the number of optical elements (Jiang et al., 2006). One of the most powerful design methods for the illumination method is the 3D simultaneous multiple surfaces (3D SMS) method (Miñano et al., 2009). Given the input and output wavefronts, the freeform surface can be calculated simultaneously point by point. Figure 2.8(a) shows the design of a freeform condenser with the 3D SMS method while Figure 2.8(b) shows an example of the Kohler surfaces design of the freeform surface for illumination applications.

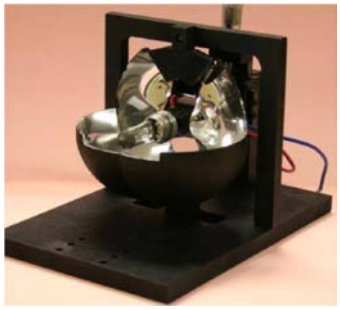

(a) Freeform condenser design with the 3D SMS method

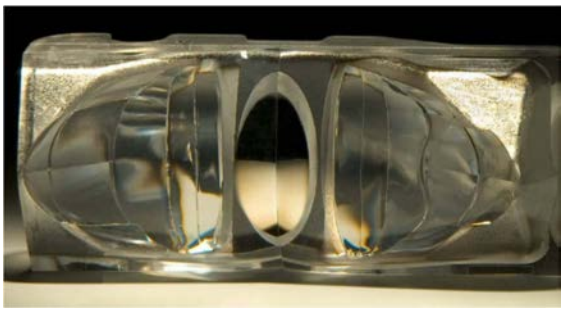

(b) Design of free-form Kohler surfaces for integration of the illumination distribution

Figure 2.8 Freeform illumination systems (Miñano et al., 2009)

Freeform lenses are also widely used in lighting systems, e.g. LED lighting systems. The freeform lenses are used to redistribute the light flux from the LED to meet the needs for lighting. Figure 2.9 shows two examples of the freeform lens for LED lighting. For the design as shown in Figure 2.9(a), the lens is used for

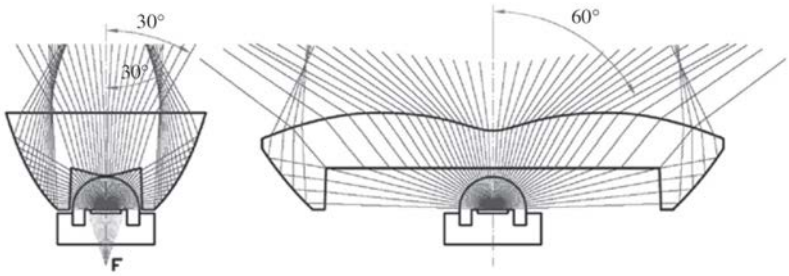

(a) Design principles on Y and X sections for one LED lens

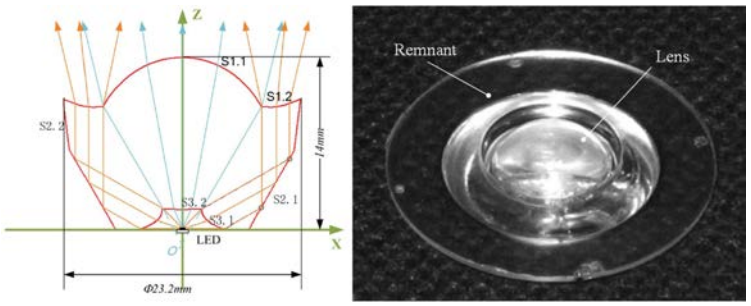

(b) Ray trace model and the molding lens for another LED lens

Figure 2.9 Freeform lens for LED lighting (Jiang et al., 2010, Zheng et al., 2009)

streetlighting and the lighting has a rectangular pattern to appropriately cover the roadway without excessive spill light into other areas to increase the lighting efficiency (Jiang et al., 2010). The design as shown in Figure 2.9(b) utilizes a freeform lens to generate a uniform illumination with a divergence half-angle of 6° and the efficiency is as high as 78.6% (Zheng et al., 2009).

Freeform surfaces with micro structures such as microlens array (Cheung et al., 2010), surface with Frustum ridge structures (Kong et al., 2013), micro-grooves (Fang et al., 2003), and micro-pyramids (Yan et al., 2010a) are widely used in advanced optics to improve performance which provides irreplaceable functionalities. Figure 2.10 shows a variety of freeform surfaces with microstructures. Microlens

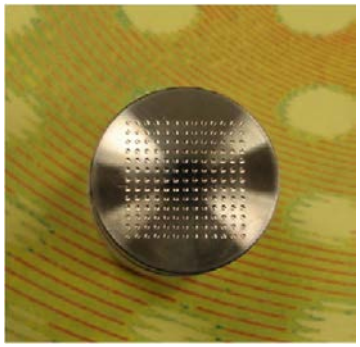

(a) Micro-lens array

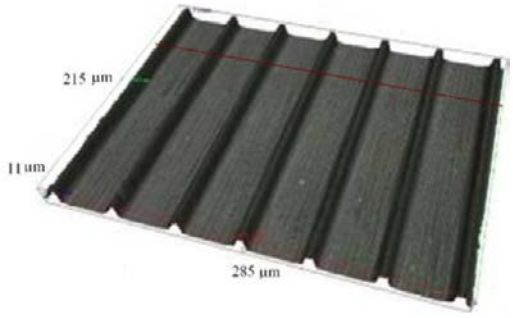

(b) Micro-ridge

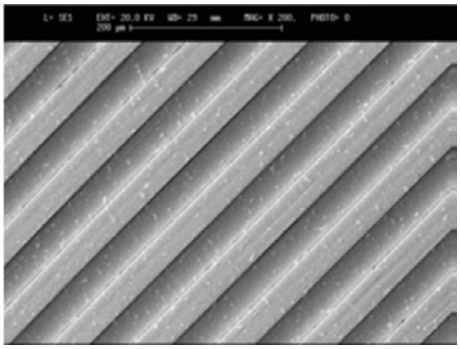

(c) Micro-grooves

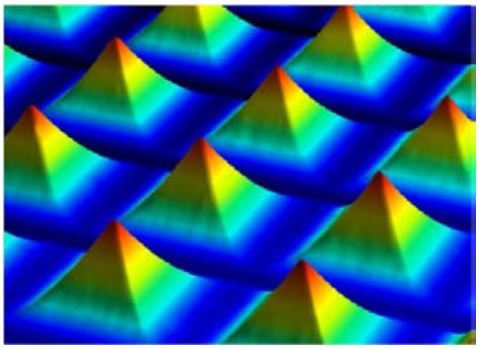

(d) Micro-pyramids

Figure 2.10 Freeform surfaces with micro structures (Cheung et al., 2010, Kong et al., 2013, Fang et al., 2003, Yan et al., 2010a)

arrays have various applications for focusing, illuminating and imaging. The micro-ridge has self-cleaning and special imaging functionalities. Micro-grooves have a wide range of applications in mechanical, electronic, photonic and bio-medical fields. The applications of microstructures are becoming more important and attracting more attention. There is a lot of applications in the roll-to-roll industry for mass production of everyday-life products incorporating microstructures. Since the dimensional scale of the microstructures is small, down to several micrometres or even smaller, the manufacturing and measurement of these features are challenging.

Roll-to-roll manufacturing of microstructure is a promising technique to achieve mass production. Figure 2.11 shows one of the examples of a roll-to-roll process and the machined prism film. The prism file was fabricated on a 100 μm-thick film substrate. The experiment showed that the film had high refractive indices which made it possess a better on-axis luminous gain.

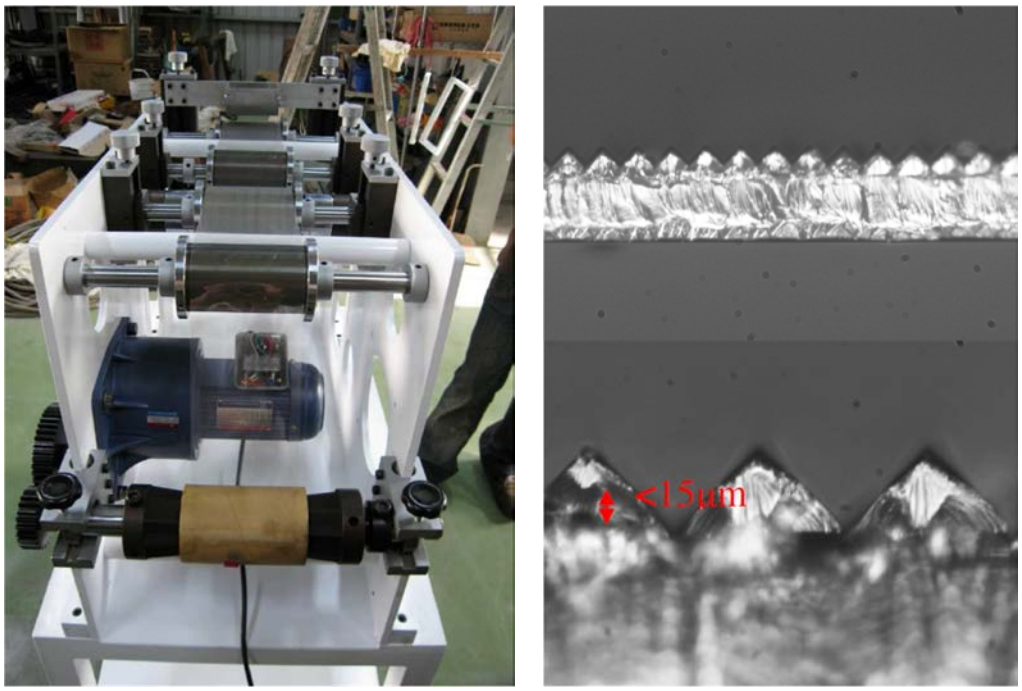

(a) The roll-to-roll equipment *(b) Image of the prism structures*

Figure 2.11 Roll-to-roll fabrication process (Wang and Tseng, 2009)

2.3 Machining of precision freeform surfaces

Ultra-precision machining technologies enable the manufacturing of precision freeform surfaces. With the development of science and technology, there are a lot of machining technologies which are capable of machining precision surfaces which include focused ion beam technology, single point diamond turning, precision grinding and polishing, etc. One of the most commonly used and powerful technologies for ultra-precision machining is single point diamond turning (SPDT) which enables the machining to have high form accuracy and super smooth surface finishing. With its flexibility and relatively low cost, these machines are equipped in many precision machining centres. Along with the development of science and technology for manufacturing, the definition of precision varies.

Nowadays, ultra-precision machining can produce components with form accuracy better than 0.1 μm and surface roughness better than 0.01 nm. The trends of machining accuracy are predicted (Taniguchi, 1983) and shown in Figure 2.12 In

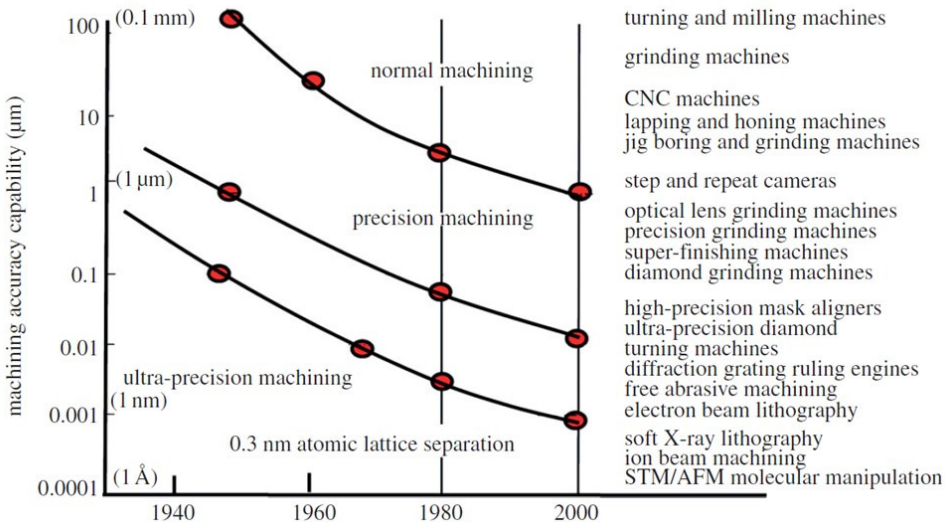

Figure 2.12 An interpretation of the Taniguchi curves, depicting the general improvement of machine accuracy capability with time during much of the twentieth century (Shore and Morantz, 2012)

the past few decades, the machining accuracy of normal machining technologies such as CNC machines has increased from 0.1 mm to 1 μm while the accuracy for ultra-precision diamond turning machines has increased from 1 μm to 0.01 μm. For soft X-ray lithography, ion beam machining and STM/AFM molecular manipulation technologies, the accuracy has achieved the atomic level.

The ultimate achievement for ultra-precision machining is to machine workpieces at atomic level. In fact, this was achieved first by IBM in the work to move atoms using the tips of scanning tunnelling microscopy (STM) (Eigler and Schweizer, 1990) and later atomic force microscopy (AFM) by other research groups (Blackman et al., 1990, Leung and Goh, 1992, Yan et al., 2010b). However, machining a workpiece per atom has ultra-low efficiency and can only be conducted at a very small scale. The motion of the tip is controlled by the piezoelectric components to ensure the motion accuracy. If a large machining area is required, the accuracy of the motion with a large moving range is a problem regarding ensuring the overall machining accuracy. Nowadays, this kind of technology is still limited due to these shortages. Figure 2.13 shows series of STM images taken for the construction of an array of xenon atoms showing “IBM” on a nickel (110) surface conducted by IBM (International Business Machines Corporation). Since this technology relies on the STM/AFM instruments, the limitations depend mainly on the specifications of the STM/AFM, e.g. the work developed by Harbin Institute of Technology (Yan et al., 2010b) has the motion range and resolution of 100 μm±5 nm, 100 μm±5 nm, and 20 μm±2 nm for the x, y and z directions, respectively, while the machining speed is 10 μms^{-1}. Figure 2.14 shows the schematic illustration of the system to perform 3D mechanical machining at the nanometre scale.

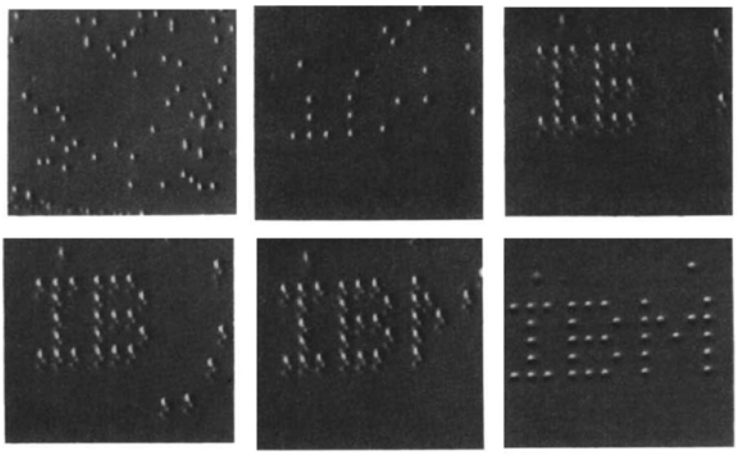

Figure 2.13 A sequence of STM images taken during the construction of a patterned array of xenon atoms on a nickel (110) surface (Eigler and Schweizer, 1990)

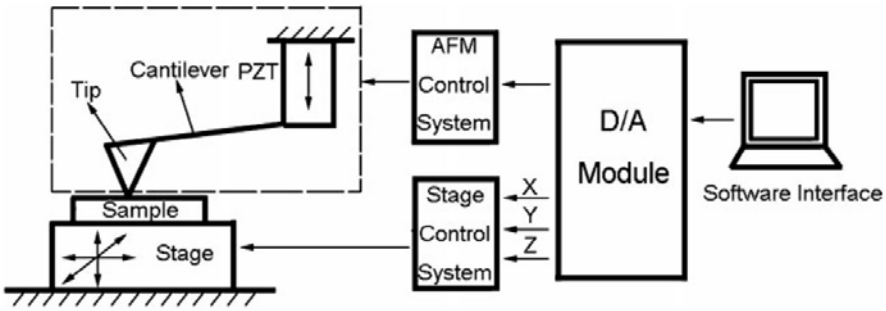

Figure 2.14 Schematic illustrating the integration of a closed-loop nanoscale precision stage with an AFM to perform 3D mechanical machining at the nanometre scale (Yan et al., 2010b)

Focused ion beam technology is a promising technology for ultra-precision machining (Ampere, 2004). Applications using focused ion beam technology are increasing due to its advantages over other technologies especially in the micro-machining area. A focused ion beam has high machining resolution and accuracy. It can machine without masks and is able to machine many different materials and geometrical features. The focused ion beam technology has the ability to machine small features at a size smaller than 1 μm, which makes it popular in the ultra-precision machining field. Figure 2.15 shows a SEM image of a sinusoidal wave surface

machined by focused ion-beam milling. It is concluded (Ampere, 2004) that with a small beam diameter of the order of 10 nm and small currents of the order of 1 pA, the machining resolution of the order of 1 nm can be achieved. Figure 2.16(a) shows one of the focused ion-beam machines in the National University of Defense Technology of China and Figure 2.16(b) shows the flow of the focused ion-beam machining process.

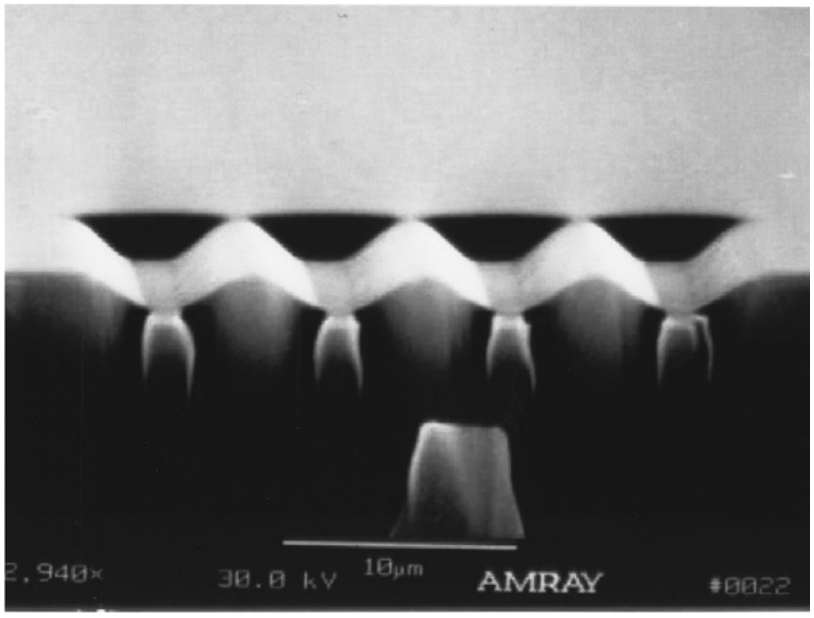

Figure 2.15 SEM image of the sinusoidal wave machined by focused ion-beam milling (Vasile et al., 1999)

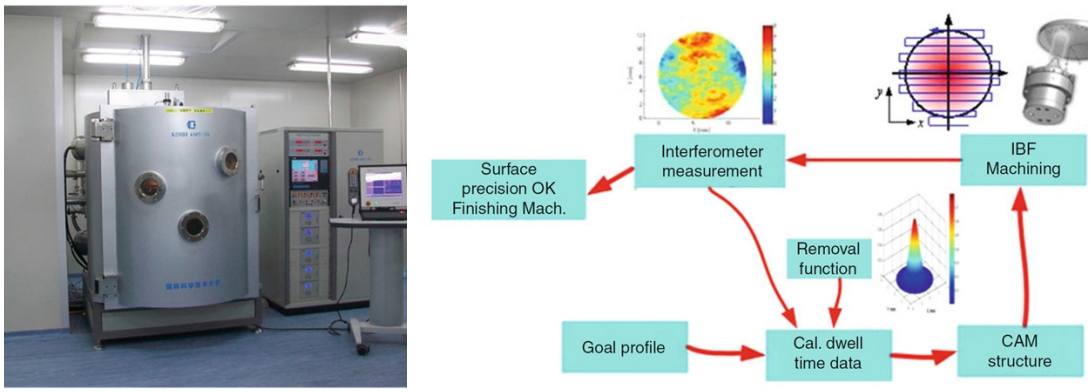

(a) The machine *(b) The flow of the process*

Figure 2.16 Focused ion-beam machining (Xie and Li, 2015)

With the development of the precision technologies for machine tools, diamond cutting is the most widely used precision machining method. The Large Optics Diamond Turning Machine (LODTM) (Hale, 1999) from Lawrence Livermore National Laboratory (LLNL) of the USA is considered to be the world's most accurate lathe. Figure 2.17 shows a cut-away view of the Large Optics Diamond Turning Machine. The machine has a vertical axis and it can machine workpieces as large as 64 inches in diameter, 20 inches in height and 3,000 pounds in weight. The moving range of the cutting tool in the X-Z plane is 37 by 20 inches. The machining accuracy of the LODTM is 28 nm root mean square (RMS) while the surface finish is 5 to 10 nm depending on the machining conditions. To achieve the highest accuracy, the metrology loop and structural loop were designed to be separated and only the spindle belongs to both loops. The specifications of the LODTM are shown in Table 2.1.

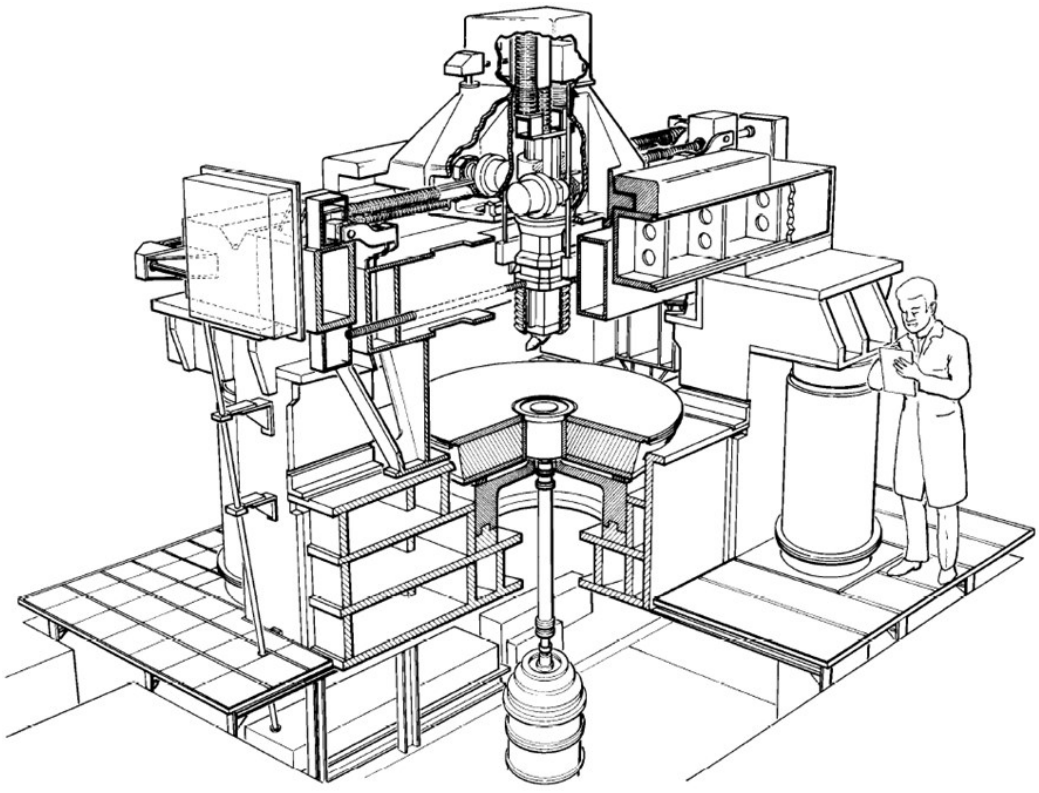

Figure 2.17 Cut-away view of the Large Optics Diamond Turning Machine (Hale, 1999)

Table 2.1 Specifications of the LODTM

Maximum workpiece size	64 inches in diameter by 20 inches high
Maximum workpiece weight	3000 pounds
Cutting tool movement range	37 by 20 inches in X-Z plane
Form error	28 nm RMS
Surface finish	5 to 10 nm RMS

For diamond turning, the workpiece is mounted on the spindle while the diamond tool moves along the workpiece surface for precision machining. There is another kind of machining method called raster milling where the diamond tool is installed on the spindle while the workpiece moves to achieve machining of the desired surface. Ultra-precision raster milling allows for direct machining of the freeform surfaces with sub-micrometre form accuracy and surface finish in the nanometre range (Kong and Cheung, 2012). Figure 2.18 shows the freeform 705G ultra-precision raster

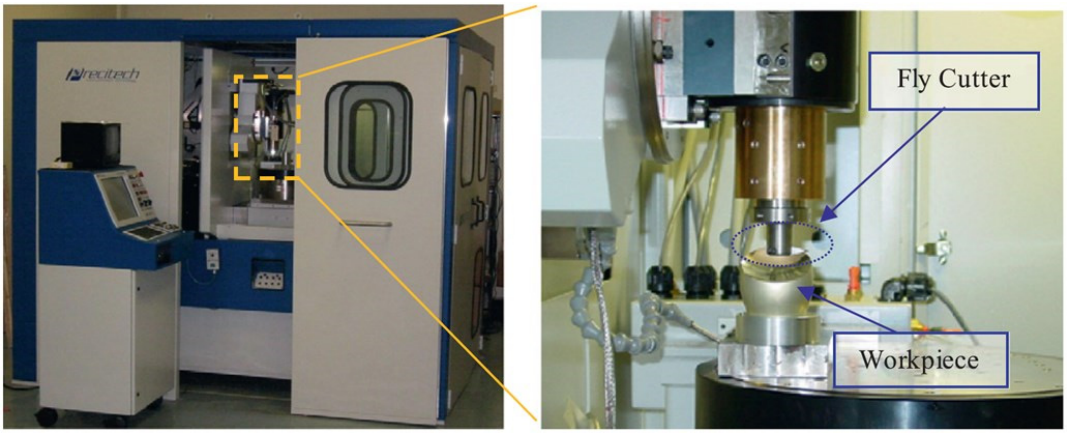

Figure 2.18 Freeform 705G ultra-precision raster milling machine tool (Kong and Cheung, 2012)

milling machine tool. However, the machining efficiency of raster milling is relatively low as compared with diamond turning since the cutting process only happens in a small period in every cycle of the movement of the diamond tool.

Although diamond cutting has very high accuracy and is widely used in precision machining, it is difficult to machine some hard and special materials. For difficult-to-machine material, precision grinding is one of the promising machining technologies (Brinksmeier et al., 2010), especially in the optics manufacturing industry since many of the optical materials are hard materials. Researchers in the Hong Kong Polytechnic University (Zhang et al., 2016, Chen et al., 2016) used ultra-precision grinding to machine hard material such as TiC-based cermet and Silicon Carbide. Figure 2.19 shows the 450UPL ultra-precision grinding machine and its setup.

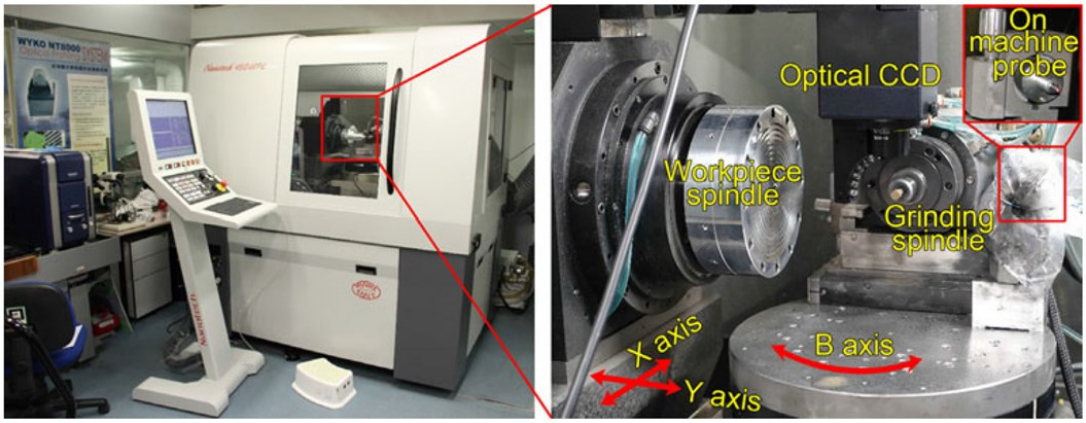

Figure 2.19 Ultra-precision grinding machine (450UPL, Moore nanotech. USA) (Zhang et al., 2016)

Compared with diamond cutting, the cutting force for machining of hard material is large and this requires the machine to be highly stiff. To address this issue, some special machine structures were designed. Figure 2.20 shows a grinding machine with the design of Tetraform C devised around the NPL Tetraform machine concept. With the special designed structure, the stiffness of the machine is large and the

experimental result showed that hardened bearing steel M50 can be machined to achieve optical surface with less than 10 nm Ra surface roughness (Stephenson et al., 2001).

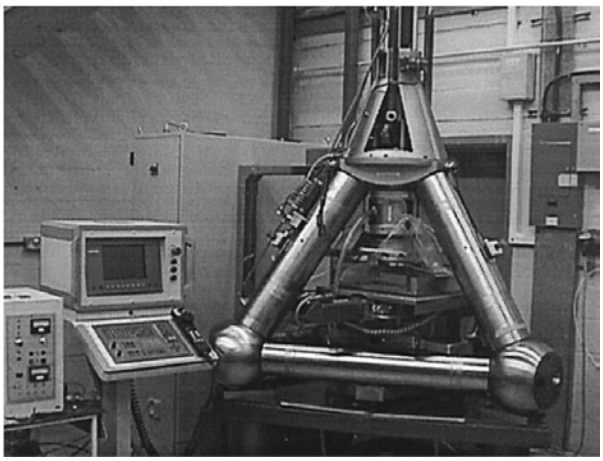

Figure 2.20 Photograph of Tetraform C (Stephenson et al., 2001)

Another issue for diamond turning or cutting is that there are tool marks left on the surface, while polishing is a post-processing machining technology to remove the tool marks. Figure 2.21 shows a 7-axis Zeeko IRP200 ultra-precision freeform polishing machine from the UK. The machine has the moving range of 300 mm along the X axis, 260 mm along the Y axis, 130 mm along the Z axis, ±90° along the A axis and ±180° along the B axis. It has a C axis for mounting of the workpiece and an

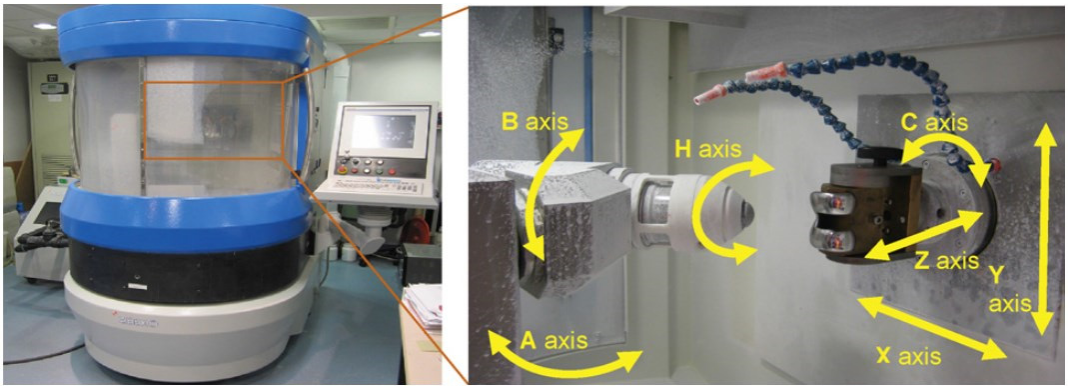

Figure 2.21 Ultra-precision freeform polishing machine (Zeeko IRP200 from UK) (Cheung et al., 2011)

additional H axis for the polishing head. The surface finish can be achieved to several nanometres after the polishing process.

2.4 Measurement of precision freeform surfaces

As mentioned in the previous sections, freeform-shaped surfaces have a large range of applications. Different applications have different sizes and tolerance requirements as shown in Figure 2.22 (Savio et al., 2007). This requires the measurement process to be able to determine if the machined parts meet the requirements of the design specifications. In order to meet different measurement requirements for different sizes and different measurement uncertainties, different kinds of measurement technologies have been developed for the evaluation procedures.

The measurement instruments can be classified as contact measurement instruments and non-contact measurement instruments regarding their measurement concepts of whether the instrument is touching the workpiece during the measurement process. One of the most important measurement instruments for measuring geometrical features is the coordinate measuring machine (CMM) and it has become one of the industrial standards due to its high accuracy and flexibility. Most of the traditional CMMs use contact measurement methods since the machine is usually equipped with a touch trigger probe. Nowadays, many advanced CMMs are also equipped with non-contact sensors such as laser scanners and 2D cameras. Most of the non-contact measurement instruments are optical-based instruments but there are also some which are based on force or current such as AFM (atomic force microscopy) and STM (scanning tunnelling microscopy). On the other hand, most of the measurement instruments are offline measuring instruments since the measurement processes are off the machine facilities and most of them require a clear and vibration-isolated environment.

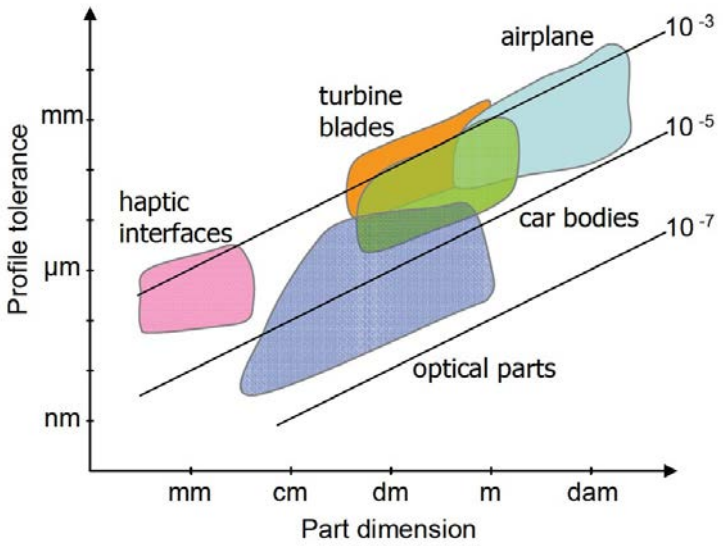

Figure 2.22 Typical values of tolerances vs. dimensions (Savio et al., 2007)

Determined by the number of sensors involved in relation to the measurement principle, the measurement systems can be classified as single-sensor measurement systems and multi-sensor measurement systems. After many years of development, there are many kinds of measurement principles for the single-sensor measurement instruments while multi-sensor measurement instruments are relatively new in the field.

2.4.1 Single-sensor measurement systems

Most of the traditional measurement systems are single-sensor instruments which are solely based on a single sensor or a single measurement principle. According to the measurement method in terms of contact with the workpiece, they can be classified by contact measurement and non-contact measurement, e.g. CMM machines and laser interferometers. In this section, the common single measurement systems are reviewed and the main advantages and disadvantages are discussed. Instead of giving a general description of the instruments, the most advanced or commonly available commercialized products are given as examples.

2.4.1.1 Coordinate measuring machines (CMMs)

Coordinate measuring machines (CMMs) are the most widely used measurement instruments for surface measurement (Hocken and Pereira, 2016) which have become the actual industry standards for geometrical measurement. After several decades of development, the accuracy of the CMMs are ensured by the sophisticated designed hardware and software together with equipping a high repeatability touch trigger probe. ZEISS XENOS (ZEISS, 2016) shown in Figure 2.23 is one of the most accurate commercialized CMM machines which has the measurement range of 900 mm × 1500 mm × 700 mm and MPE of 0.3 μm. The ZEISS XENOS has a new design Y axis which has a lower moving mass that enables the optimal positioning of the Y coordinate. It also has a virtual central drive to ensure the optimal force distribution according to the position of the X axis to maximize the accuracy. The probe equipped

(a) The machine *(b) The equipped VAST probe*

Figure 2.23 ZEISS XENOS CMM (ZEISS, 2016)

with the ZEISS XENOS is the powerful sensor-VAST gold reference probe (Wozniak, 2007). Figure 2.23(a) shows a snapshot of the ZEISS XENOS CMM and Figure 2.23(b) shows the equipped VAST probing system. The specifications of the ZEISS XENOS CMM are shown in Table 2.2.

Table 2.2 Specifications of the ZEISS XENOS CMM

Measuring range of X axis	900 mm
Measuring range of Y axis	1,500 mm
Measuring range of Z axis	700 mm
length measurement error E0	0.3 + L/1000 μm

(L is the length to be measured in mm)

The ISARA400 (Widdershoven et al., 2011) as shown in Figure 2.24(a) is an ultra-precision CMM developed by IBS with a measurement range of 400 mm × 400 mm × 100 mm and one-dimensional (1D) measurement uncertainty (k=2) of 50 nm, two-dimensional (2D) measurement uncertainty (k=2) of 70 nm and three-dimensional (3D) measurement uncertainty (k=2) of 109 nm. The system was designed to be Abbe error-free in which three laser beams are always aligned with the centre of the probe tip. The laser interferometers measure the coordinates of the probe tip along all X, Y and Z axes with temperature, pressure and humidity compensation. The ISARA400 is equipped with a Triskelion probe system as shown in Figure 2.24(b). The probe itself can detect the deflections of the probe tip in all X, Y and Z directions and the absolute measurement error is less than 15 nm in 3D (Donker et al., 2010). Table 2.3 shows the specifications of the ISAR400.

(a) ISARA400 *(b) Ultra-precision touch probe*

Figure 2.24 ISARA400 Next generation ultra-precision coordinate measuring machine (IBS Precision Engineering, 2016)

Table 2.3 Specifications of the ISARA400

Measuring range of X axis	400 mm
Measuring range of Y axis	400 mm
Measuring range of Z axis	100 mm
Positioning accuracy	Better than ± 0.5 μm (x,y,z) during standstill
3D measurement uncertainty (k=2)	109 nm

A non-contact measurement machine was developed (Henselmans, 2009) for measuring freeform optics. The machine was installed with an optical sensor (Cacace, 2009). The measurement machine has the universal measurement ability that it can measure flat, spherical, aspherical, freeform and off-axis surfaces, convex and concave

surfaces, transmission and reflection optics. The measurement range is up to 500 mm in diameter and 100 mm in height. The measurement uncertainty is within 30 nm (k=2). The developed measurement machine and the optical sensor are shown in Figure 2.25 and Figure 2.26.

Figure 2.25 Non-contact freeform optics measurement machine prototype (Henselmans, 2009)

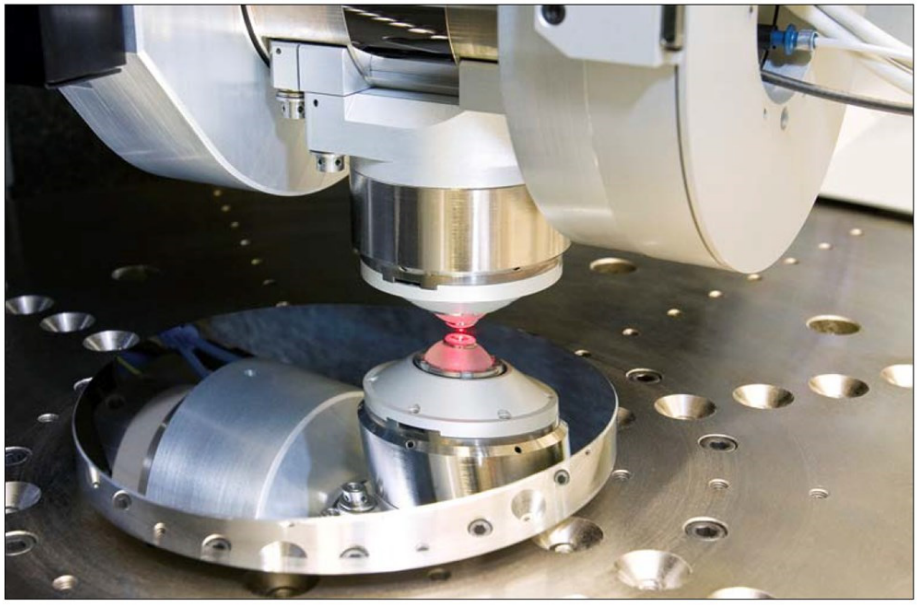

Figure 2.26 The optical sensor installed in the machine (Cacace, 2009)

Probing systems are the most important components for CMMs. The accuracy and repeatability of the probing systems is one of the important factors to determine the measurement uncertainty of CMMs. Depending on the measurement principle, there are many kinds of measurement probes available. Figure 2.27 shows various kinds of probing systems such as the Zeiss MT probe, Zeiss VAST prove, Leitz TRAX probe, Renishaw probe SP80, etc.

(a) Zeiss MT probe

(b) Zeiss VAST probe

(c) Leitz TRAX probe

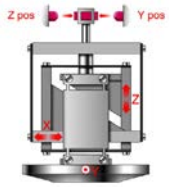

(d) Renishaw probe SP80

(e) Renishaw SP25M probe

(f) NPL microprobe

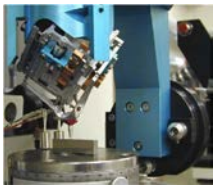

(g) METAS 3D touch probe

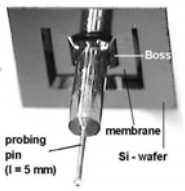

(h) Silicon membrane probe

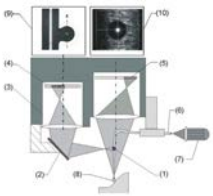

(i) Opto-tactile probe from PTB

Figure 2.27 Varies kinds of probing systems (Weckenmann et al., 2004)

The most widely used probing system for CMMs is the touch trigger probe at a much lower cost such as the TP200 from (Renishaw, 2014). With this kind of probing system, since the probe only generates a trigger signal to the CMM, the probing direction needs to be the same as the surface's normal direction to precisely compensate for the radius of the probe tip. If the probing direction is not aligned along

the normal direction, there is error in determining the actual point to measure (Chiang and Chen, 1999). This phenomenon is described in Figure 2.28 which clearly shows that there is a deviation from the target point to the compensated point (measurement result). This is especially true when the normal vectors are diverse largely from the actual proving directions. In practice, a CAD file is used to calculate the normal vectors of the measured workpiece at different positions to ensure the accuracy of the measurement.

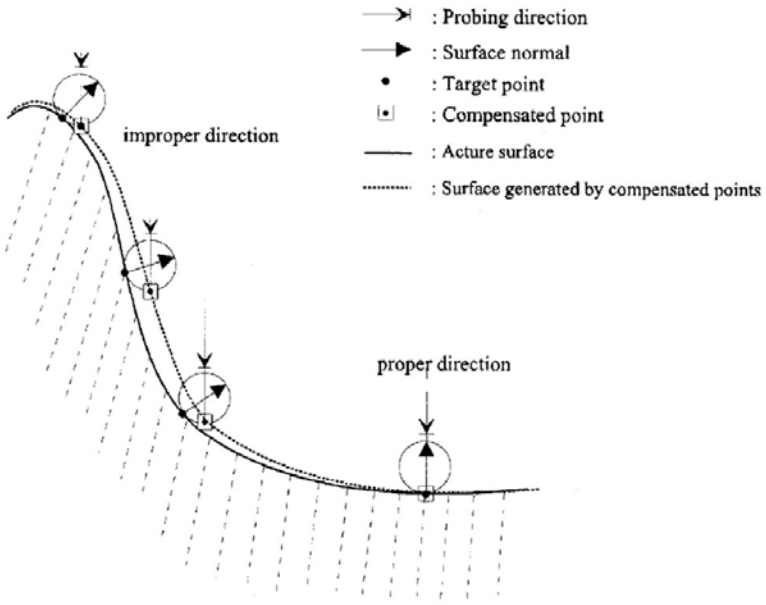

Figure 2.28 Surface generated by improper probing directions (Chiang and Chen, 1999)

However, in the presence of form error, the actual normal vectors are not exactly the same as the designed ones, and this is not known in advance since the true surface is not known. Moreover, the CAD model needs to align to the measured workpiece; this work is usually done manually and there is an alignment error in the process. There are sometimes no reference features in the design or the reference features come from rough machining, which introduces a large alignment error and thus influences the final measurement result.

2.4.1.2 Profilometer

Profilometers are another kind of instrument for surface measurement. One of the most advanced profilometers is the Ultrahigh-Accurate 3-D Profilometer (UA3P) (Takeuchi et al., 2004). The UA3P utilizes an atomic force probe as the touching element and the measurement accuracy is in the order of 10 nm. The measurement range of the model of UA3P-700H is 500 mm × 500 mm × 120 mm. The machine can also measure high slope surface up to 75°. The construction of the UA3P is shown in Figure 2.29. The AFM probe tip is utilized as the sensor and three laser interferometers are used to detect the coordinate information of the probe so as to avoid the Abbe error (Zhang, 1989), which is the principle of achieving such highly accurate measurement result. The measuring force is about 0.15 mN - 0.30 mN and the tip angle is 30° while the radius of the tip is 2 µm. Since the UA3P measures the workpiece using an AFM such as probe tip, with a high lateral resolution measurement, the measurement speed is slow, i.e. as low as 0.005 mm/s. Table 2.4 shows the specifications of the UA3P-700H.

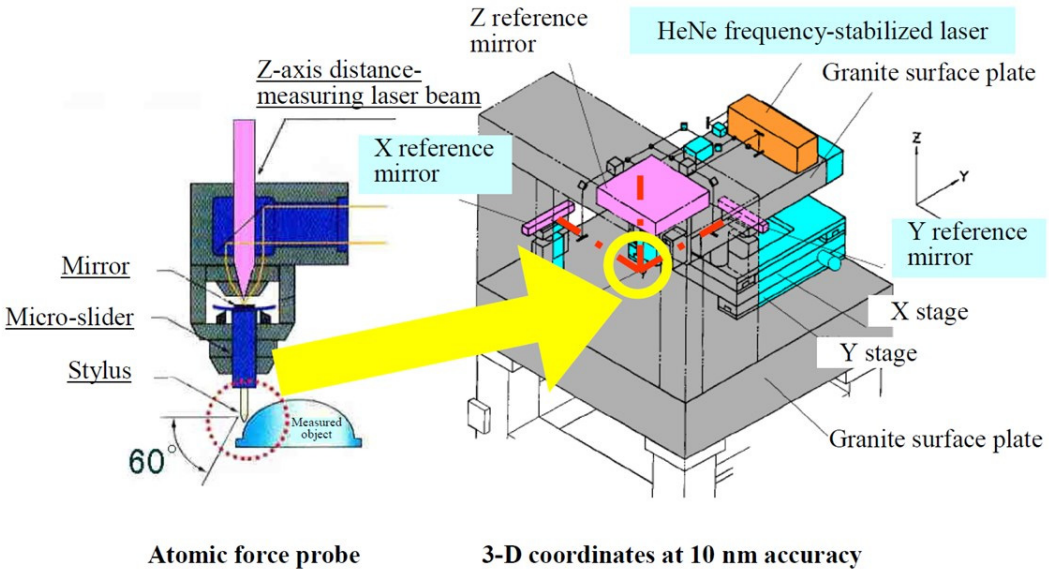

Figure 2.29 Construction of ultrahigh-accuracy 3-D measuring machine (Takeuchi et al., 2004)

Table 2.4 Specifications of the UA3P-700H

Measuring range (X, Y, Z axes)	500×500×120 mm
Resolution	0.3 nm
Angle for side-surface measurement	75°
Measurement accuracy	30° max: ±0.05 μm 45° max: ±0.08 μm 60° max: ±0.1 μm
Measurement speed	0.01-30 mm/s

Taylor Hobson has provided a wide range of surface profilometers over its long history and they have become the industrial standard. The core of the profilometer is a Phase Grating Interferometer (PGI) which provides form repeatability of less than 100 nm (Taylor Hobson, 2016). The measurement resolution of the gauge is down to 0.3 nm while the measurement range is up to 20 mm. For contour measurement, the form error is less than 0.2 μm. For roughness measurement, the noise level of root-mean-square roughness measurement (Rq) is less than 2 nm. Figure 2.30 shows the working principle of the PGI. Although the PGI has high measurement accuracy, it is not suitable for soft material such as copper and aluminium since the diamond measurement tip may damage the surface of the workpiece.

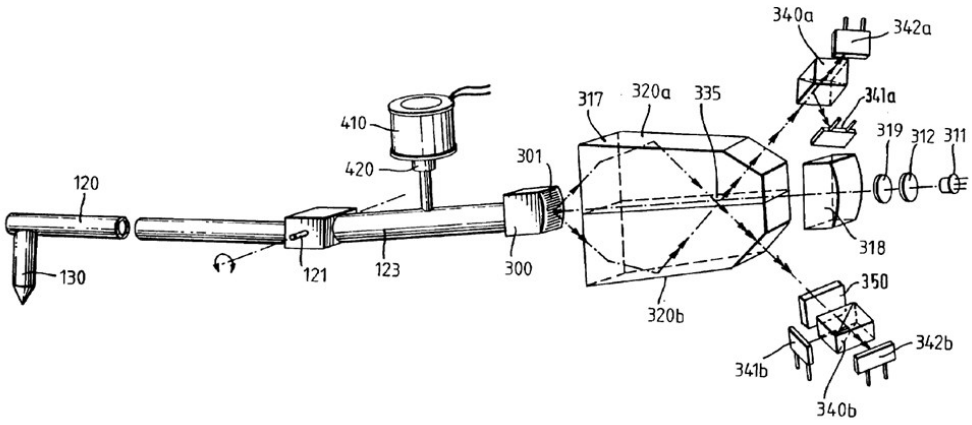

Figure 2.30 Operation principle of PGI (Buehring and Mansfield, 1996)

2.4.1.3 Scanning probe microscopy

Nowadays, the most accurate surface measurement instruments may be the famous Atomic force microscope (AFM) and Scanning tunnelling microscope (STM) (Binnig and Rohrer, 1982, Binnig and Rohrer, 1983, Binnig et al., 1986). The original design of an AFM also utilizes a STM to detect the position of the AFM tip. The vertical resolution of the AFM can be less than 0.1 nm. However, the measurement range of the AFM is as small as the order of dozens of micrometres and the measurement speed is slow. Figure 2.31 shows the measurement principle of the STM

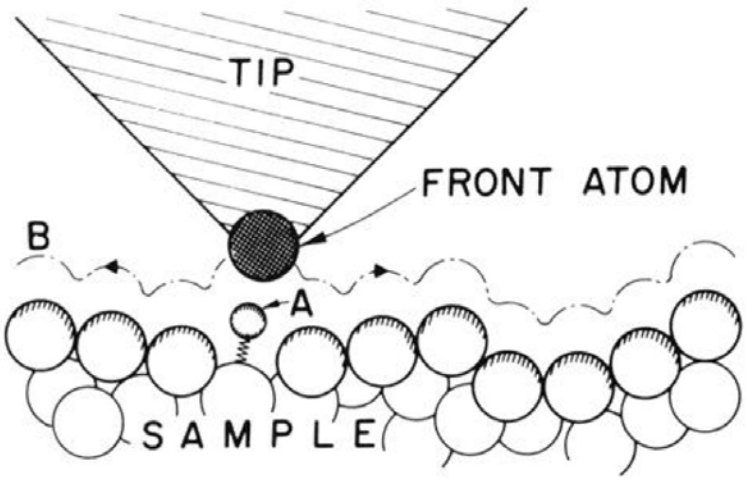

Figure 2.31 Principle of the operation of the STM as well as that of an AFM (Binnig et al., 1986)

and AFM. In order to extend the measurement range of the AFM/STM, some studies use the AFM/STM as a measure probe in the measurement machine, e.g. the UA3P (Takeuchi et al., 2004) and for on-machine measurement (Ju et al., 2014).

2.4.1.4 Interference microscopy

Phase Shifting Interferometry (PSI) (de Groot, 2011b) and Coherence Scanning Interferometry (CSI) (de Groot, 2011a) play important roles in non-contact surface metrology (de Groot, 2015). Figure 2.32 shows the working principle of the PSI. A PSI is an upgraded version of a Michelson interferometer which turns distance measurement into a surface topography measurement. A stable laser enables the Michelson interferometer to have ultra-high precision measurement accuracy and resolution, and it is widely used in industry and research, e.g. the laser interferometer gravitational-wave observatory (LIGO) (Abbott et al., 2016). The basic setup of a Michelson interferometer is shown in Figure 2.33. The interference signal obtained at

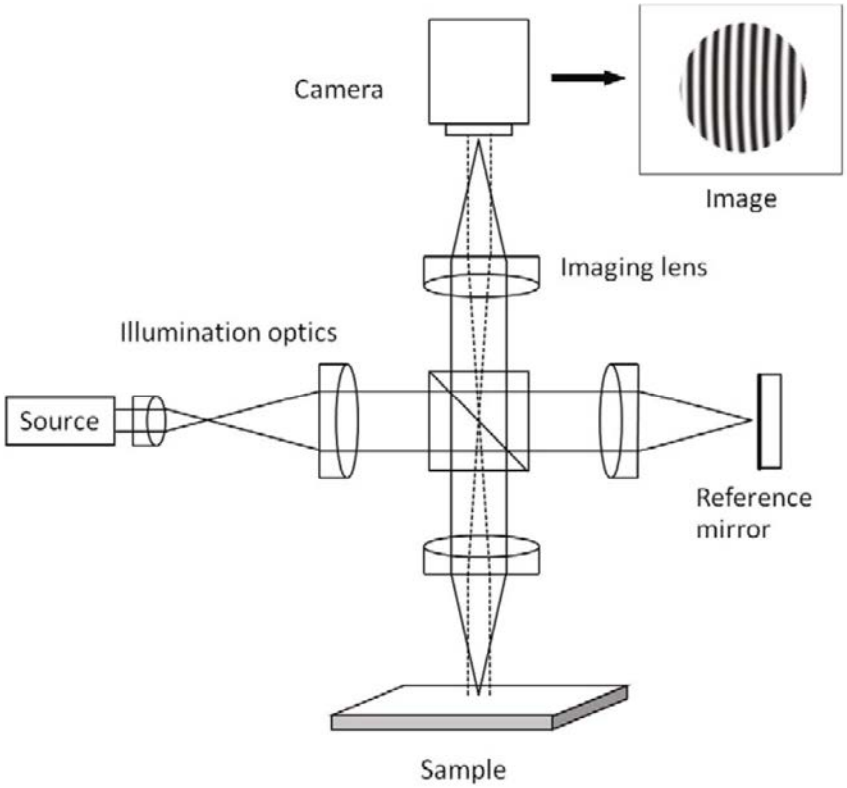

Figure 2.32 Imaging interferometer for areal surface profiling (de Groot, 2011b)

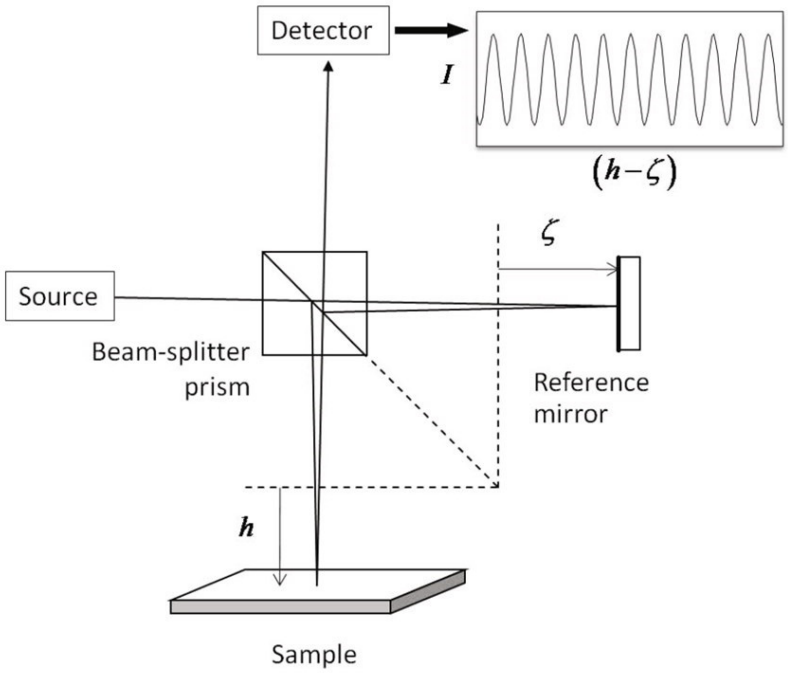

Figure 2.33 Michelson interferometer (de Groot, 2011b)

the detector can be determined as:

$$I(h,\zeta) = I_{DC} + I_{AC}\cos\left[K(h-\zeta)+\xi\right], \tag{2.1}$$

where I_{DC} and I_{AC} are fixed coefficients and K is the fringe frequency, h is the sample surface height and ζ is the position of the reference mirror, and ξ is a phase offset of the reflection and transmission properties of the optical components. The fringe frequency K can be determined as:

$$K = 4\pi / \lambda \tag{2.2}$$

where λ is the wavelength of the high coherence light source, e.g. laser.

Equation (2.1) shows that the detected intensity is a function of the difference $(h-\zeta)$, and the characteristic of the intensity is periodic. One cycle modulation of the intensity corresponds to a half-wavelength change of the distance difference of

$(h-\zeta)$. As shown in Figure 2.32, with an additional lens and a camera to measure the areal signal of the interferometric pattern, the Michelson interferometer can be upgraded to a surface topography measurement instrument. Every pixel of the camera corresponds to a specific location of the measured surface and the corresponding surface height is then measured using the concept of the Michelson interferometer. This method has a long history for visual interpretation of the fringe pattern to determine the surface characteristics of the measured surface. To digitalize the method for high-accuracy surface measurement, data processing is needed to estimate the phase:

$$\theta = Kh + \xi \tag{2.3}$$

Since the offset ξ is constant, it can be set to zero and the surface height can be determined as:

$$h = \theta / K \tag{2.4}$$

With the accurate estimation of the phase of the fringe pattern, the surface feature and the surface roughness can be measured accurately. The resolution of the phase determines the measurement resolution with regard to the wavelength of the light source. Extensive review of the PSI technology can be found elsewhere (Schmit et al., 2007, Schreiber and Bruning, 2006).

Another kind of widely used interferometry is the Coherence Scanning Interferometry (CSI). The working principle of a CSI is shown in Figure 2.34. Different from Phase Shifting Interferometry (PSI), where the interference fringes are only visible in a small range of surface height difference, the CSI provides a variation of fringe contrast according to different surface heights. This can be explained by the phenomenon as shown in Figure 2.35 where a curved surface is measured by using a

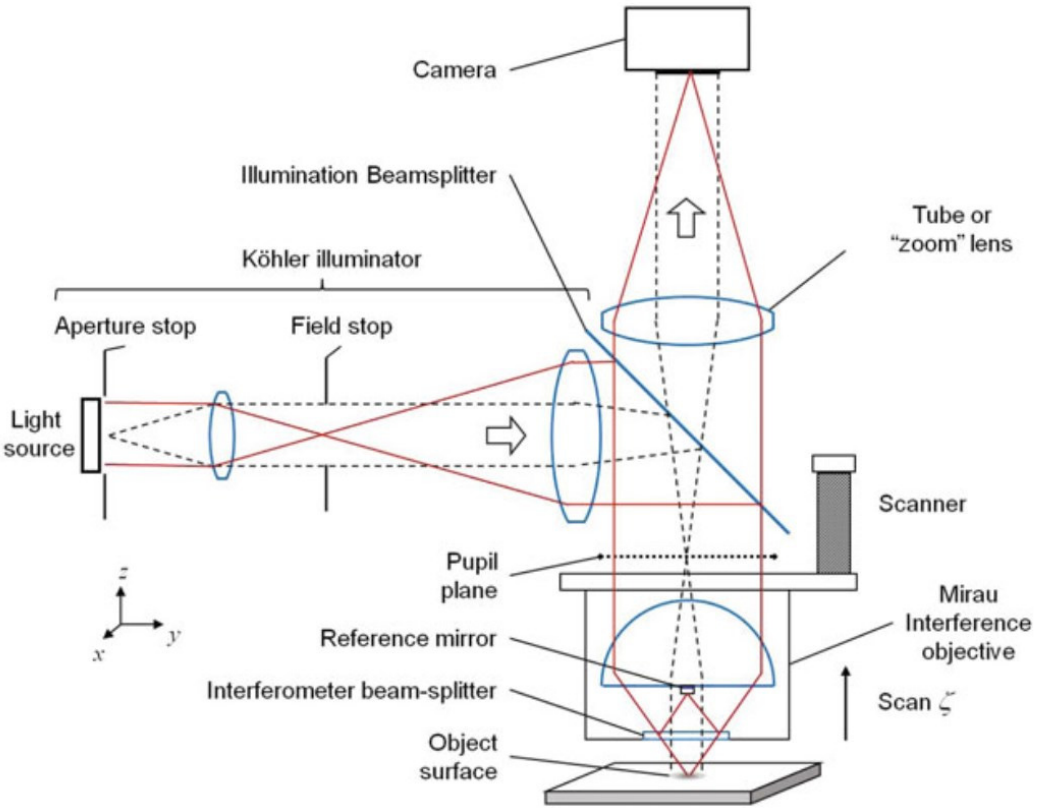

Figure 2.34 Working principle of a CSI (de Groot, 2011a)

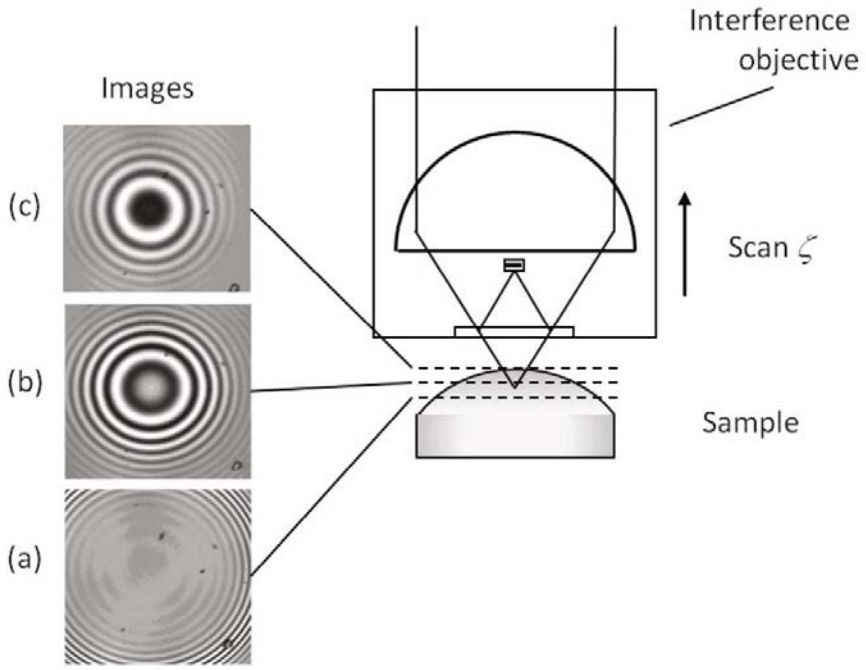

Figure 2.35 Images of interference fringes on a curved surface with low coherence illumination (de Groot, 2011a)

CSI. The contrast of the fringes varies at different heights. Combined with vertical scanning along the optical axis, the pattern determines the measured surface to be a convex surface. Figure 2.37 also shows that there is an advantage for a CSI as compared with a PSI in that there is no 2π error for the fringe pattern even for a large surface height difference.

Calculation of the surface height needs the data processing of the images of the scanned fringe pattern. Since the CSI utilizes a low coherent light source with a broadband spectrum (white light), the fringe pattern is actually a combination of interferences from light with different wavelength. Unlike the PSI which utilize the coherent light source that has a precise and stable wavelength, the CSI needs to be calibrated for the scale which is usually accomplished with a step height artefact.

The measurement resolution of optical interferometry can be very high at the nanometre level with the advanced image processing technology. However, the measurement accuracy is affected by many factors such as stability of the light source, characterization of the workpiece such as surface roughness (Pavliček and Hýbl, 2008) and surface local gradient (Liu et al., 2015).

2.4.1.5 Confocal microscopy

Confocal microscopy is another kind of widely used method of optical measurement. Compared with other kinds of optical instruments, the confocal microscope has a large numerical aperture which leads to a high lateral resolution and high ability to measure slope surface. According to the actual setup of the microscope, there are three types of confocal instruments, i.e. disc scanning, microdisplay scanning and laser scanning.

Figure 2.36 shows the basic setup of a laser scanning confocal microscope. The laser light source is projected to the surface of the measured sample through the

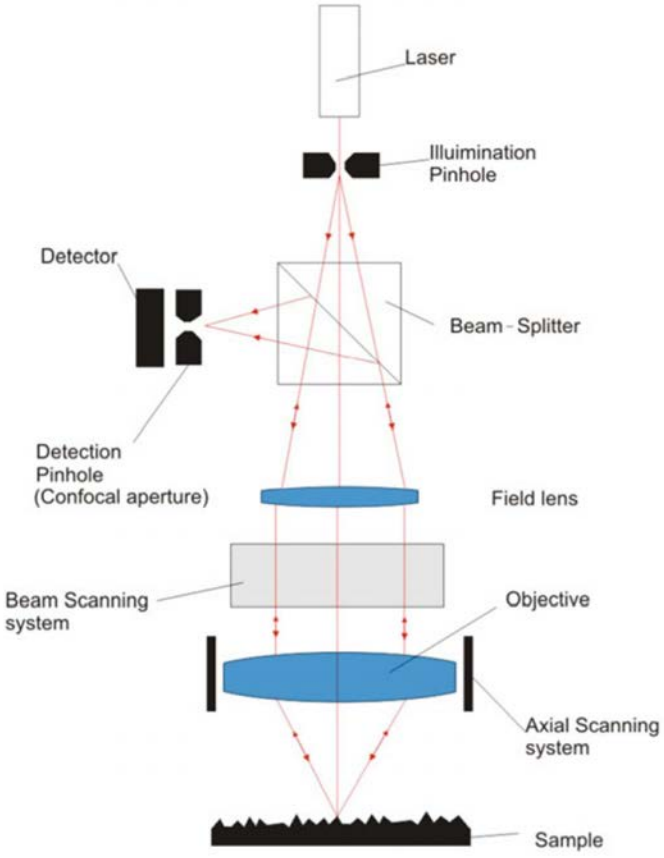

Figure 2.36 Basic setup of a laser scanning microscope with the sample in focus position (Artigas, 2011)

illumination pinhole and the objective. The light reflects back through the objective and another pinhole to the detector and this pinhole is called the confocal aperture. Since the pinhole is very small, only the light reflected from the focal plane can go through the pinhole and be detected by the detector. The image of the focal plane is obtained by scanning a laser beam on the measured surface point by point and the 3D surface is reconstructed by scanning in the vertical optical axis layer by layer. By analyzing the signal of each pixel along the z axis, the one with the strongest signal is determined to be the optimal position regarded as the focal plane. The scanning method in the lateral and vertical directions results in the measurement speed of the confocal being slow. As a result, the disc scanning and microdisplay scanning methods are introduced to improve the efficiency of the measurement which measures multiple

points at the same time. One of the advantages of the confocal microscope is that it can measure high slope surfaces. For example, a 0.95 numerical aperture can measure surface with a slope of up to 72°. Moreover, measurement with a higher slope is possible with a larger numerical aperture.

2.4.2 Multi-sensor measurement systems

Multi-sensor measurement systems can be divided into two categories, i.e. multiple measurements with single-sensor metrology systems and multiple measurement with multi-sensor metrology systems. Generally, the multiple measurement with single-sensor instruments is homogeneous data which are widely found in stitching measurement systems and repeat measurement methods. For multiple measurement with multi-sensor instruments, the datasets can be inhomogeneous or homogeneous, while the data fusion method is usually implemented with the expectation that the fused data improve the result.

2.4.2.1 Multiple measurement with a single sensor

All the surface measurement instruments have a limited field of view (FOV) and lateral resolution. To obtain a measurement result with a large lateral range and high resolution, multiple measurement is usually needed and the sub-surfaces are stitched together to form a holistic result. The stitching method can largely expand the measurement range of the instrument. As a result, a lot of work has been done to investigate different stitching methods. Many of them comprise stitching interferometry (Murphy et al., 2003). The outline of the stitching interferometry process is shown in Figure 2.37. The full aperture measurement and the sub-aperture stitching measurement of a spherical surface is shown in Figure 2.38 and the result shows that the stitching result is very close to the full aperture measured result.

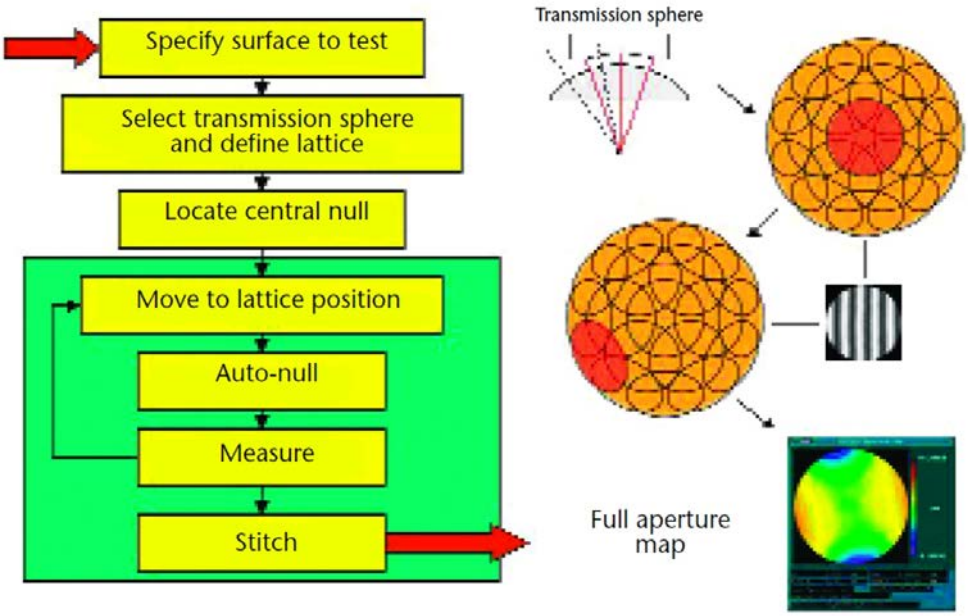

Figure 2.37 Outline of the stitching interferometry process (Murphy et al., 2003)

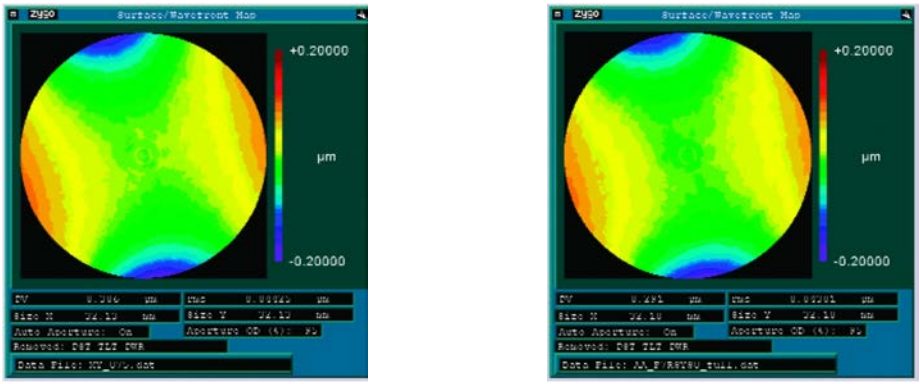

(a) Full aperture measurement with f/0.75 transmission sphere

(b) Sub-aperture stitched map with f/1.5 transmission sphere

Figure 2.38 Sub-aperture stitching (Murphy et al., 2003)

A non-null test for aspheric surfaces was developed (Zhao et al., 2014) using an elliptical sub-aperture stitching technique as shown in Figure 2.39. The testing results for a concave ellipsoid and a convex hyperboloid are shown in Figure 2.40 with residual error of peak-to-valley value (PV) = 0.0929 wave, root-mean-square (RMS) = 0.0117 wave and PV = 0.062 wave, RMS = 0.065 wave, respectively.

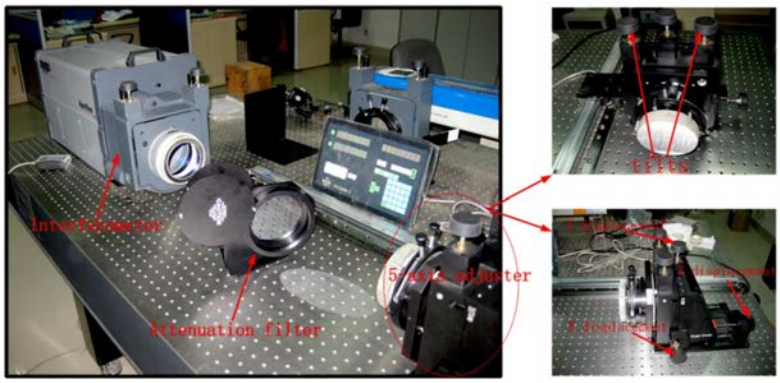

Figure 2.39 Experimental setup for the non-null testing for aspheric surfaces using elliptical sub-aperture stitching technique (Zhao et al., 2014)

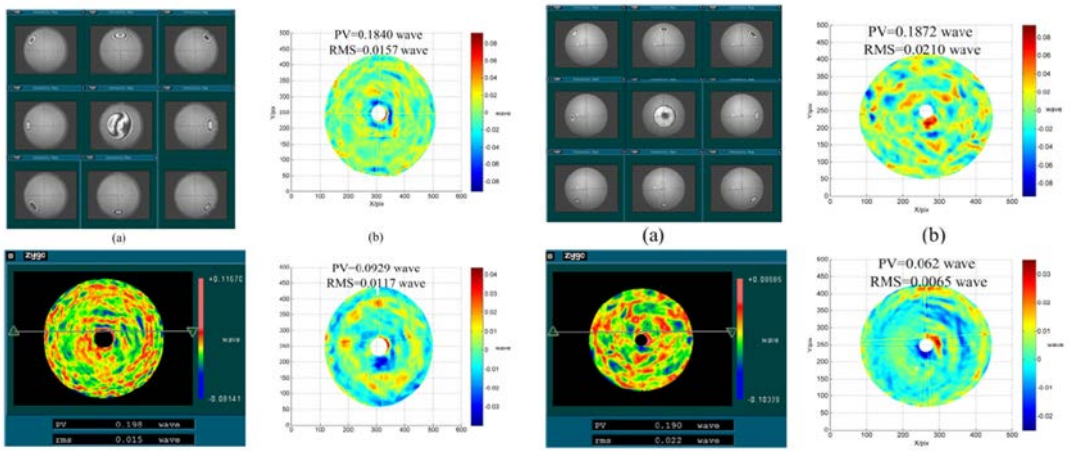

(a) Concave ellipsoid *(b) Convex hyperboloid*

Figure 2.40 Testing results for concave ellipsoid and convex hyperboloid (Zhao et al., 2014)

A four-axis fixture and a commercial profiler to perform stitching measurement was utilized (Yang et al., 2017, Ye et al., 2016) for large aspheric surfaces. To obtain an accurate stitching result, the multi-body theory, invariability of curvature radiuses and the least square principle was implemented in the stitching algorithm. The measurement system is shown in Figure 2.41. Figure 2.42 shows a measurement setup for the stitching measurement experiment for an off-axis parabolic surface and the stitching error is shown in Figure 2.42(b).

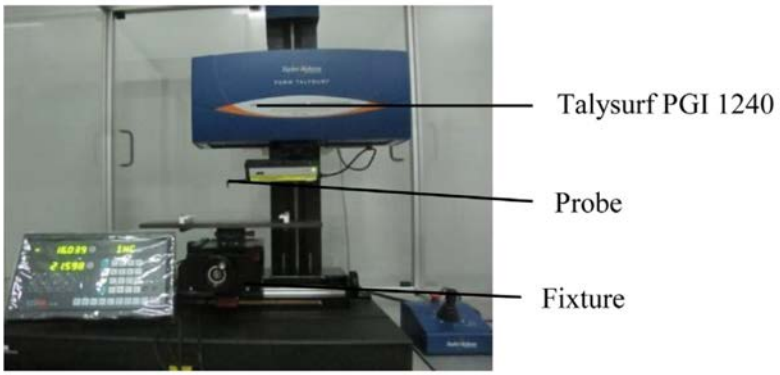

Figure 2.41 Stitching measurement system with the help of an additional 4-axis fixture (Ye et al., 2016)

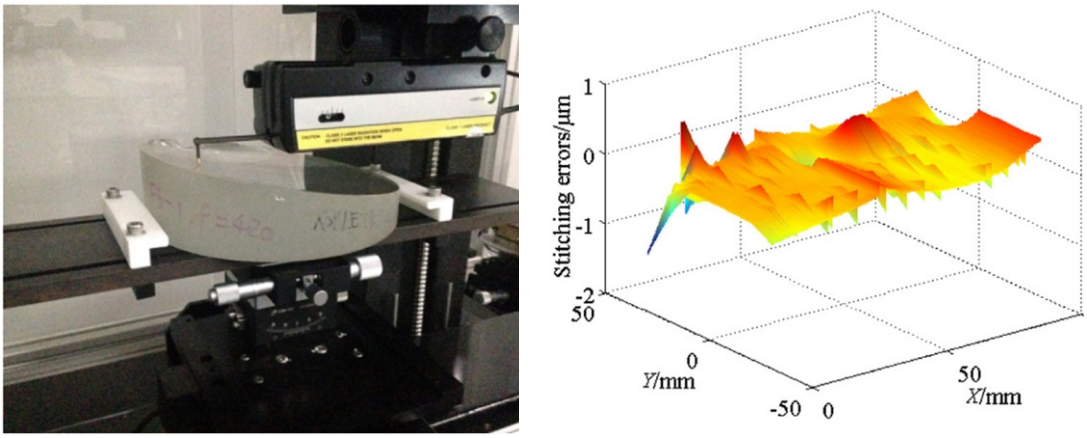

(a) Measurement setup *(b) Stitching error*

Figure 2.42 Stitching measurement of an off-axis parabolic surface (Yang et al., 2017)

2.4.2.2 Multiple measurement with multiple sensors

Nowadays, there is a development trend towards multi-sensor measurement systems since the single-sensor measurement systems can hardly meet the highly stringent requirements. There are several commercialized multi-sensor CMM machines available in the high-end market. For instance, ZEISS O-INSPECT (Carl Zeiss Industrial Metrology, 2016) is equipped with a contact sensor, imaging sensor and white light distance sensor, and is able to provide fast inspection by the image

sensor and high-accuracy 3D measurement results by the contact sensor and white light distance sensor. Werth VideoCheck (Werth Messtechnik GmbH, 2016) is designed to be equipped with many kinds of sensors such as trigger probe, fibre probe and video sensor and provides the measurement ability of small features with the help of the small-diameter fibre probe in a scale down to 20 µm, as well as quick checking with the fast trigger probe and image sensor. Hexagon Optiv Classic (Hexagon, 2016) provides a vision sensor and a touch trigger probe, while Nikon (Nikon Metrology NV, 2016) enhances true 3D multi-sensor measurement by combining a vision sensor, laser auto-focus sensor, tactile sensor and rotary indexer. Figure 2.43 shows some of the commercially available multi-sensor CMM machines. The measurement

(a) Hexagon Optiv Classic

(b) Werth VideoCheck

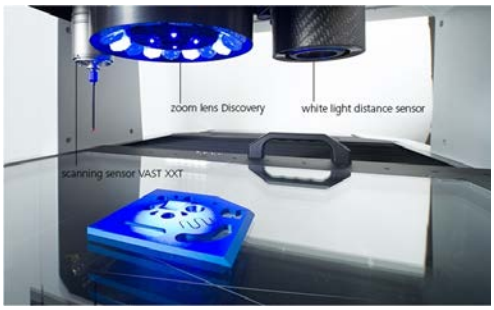

(c) ZEISS O-INSPECT

Figure 2.43 Multi-sensor CMM machines (Hexagon, 2016, Werth Messtechnik GmbH, 2016, Carl Zeiss Industrial Metrology, 2016)

range, resolution and flexibility are largely enhanced by the complementarity of the different characteristics of various sensors. The combination of different types of sensors extends the measurement ability such as accuracy and measurement range of the CMMs. However, most multi-sensor CMMs lack an optimal strategy to perform multi-sensor measurement and fusion of data from different sensors.

Multi-sensor data fusion is an emerging research area and there is a lot of research focused on the measurement strategy and algorithms for data fusion, especially in the areas of target tracking, decision-making and image processing (Raol, 2009). There is also some research on surface metrology but it is not commonly seen, relatively, especially in practice. A cooperative fusion method was developed (Galetto et al., 2015) for a distributed multi-sensor large-volume metrology system which combines datasets from angular and distance measurements. The setup of the system is shown in Figure 2.44. However, it only works for measurement by using angular and distance sensors to determine the 3D positions of the measured points and cannot be used for CMMs.

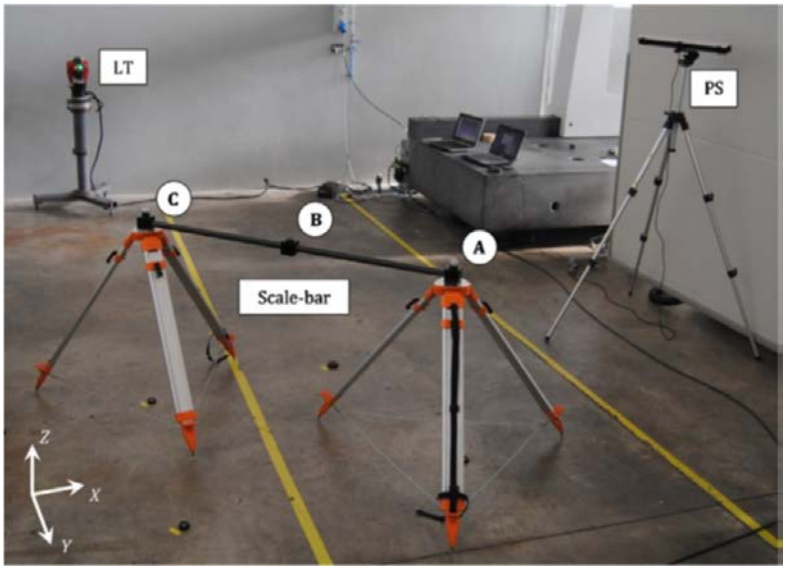

Figure 2.44 Measurement layout of the distributed multi-sensor large volume metrology system (Galetto et al., 2015)

A Gaussian process modelling method was used (Colosimo et al., 2014) to combine high-accuracy low-density CMM data with low-accuracy high-density data from the laser scanner. One of the measurement examples is shown in Figure 2.45. The two datasets were linked together by using a "linkage" model by introducing the scaling and shifting factors to correct the systemic error. The result showed that the measurement uncertainty of the fused data was reduced as compared with the results from the single measurement. This method is similar to the one proposed (Qian and Wu, 2008), but it deals with surface metrology problems instead of mechanical material design and modelling of food processors.

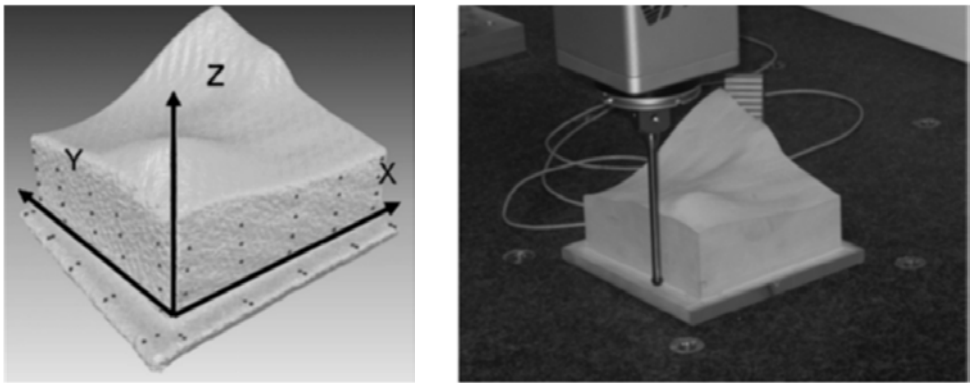

(a) Measured freeform workpiece *(b) Sampling using CMM*

Figure 2.45 Gaussian process modelling of the measurement (Colosimo et al., 2014)

The Gaussian process is a machine learning process (Williams and Rasmussen, 2006) which is largely used in research areas such as image processing. Recently, it has been used in surface metrology. The Gaussian process was utilized (Xia et al., 2008) to form error assessment for CMM machines. The procedure of the proposed method is shown in Figure 2.46. With the proposed Gaussian modelling method, the designed geometric form, systematic manufacturing errors and random manufacturing errors were decomposed. Simulation and actual measurement data demonstrated the improvement compared to the traditional method.

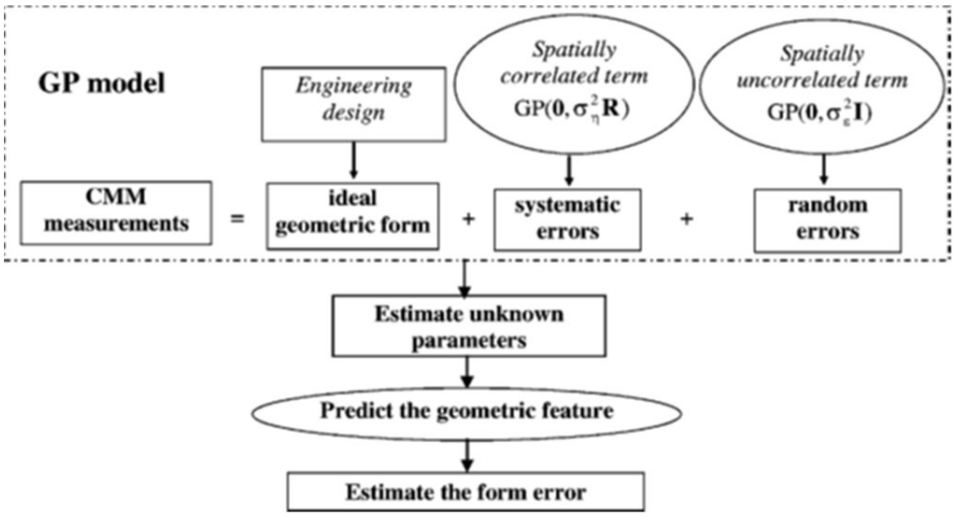

Figure 2.46 GP modelling and form error assessment (Xia et al., 2008)

A Gaussian process-based modelling method and data fusion method were developed (Yin et al., 2016) for the measurement of complex surfaces. An adaptive sampling strategy was also introduced in their work. Figure 2.47 shows one of the results for the estimated uncertainty before and after data fusion. The result showed that the measurement uncertainty of the fused dataset was smaller than the original datasets. However, the systematic error was not considered in the proposed method.

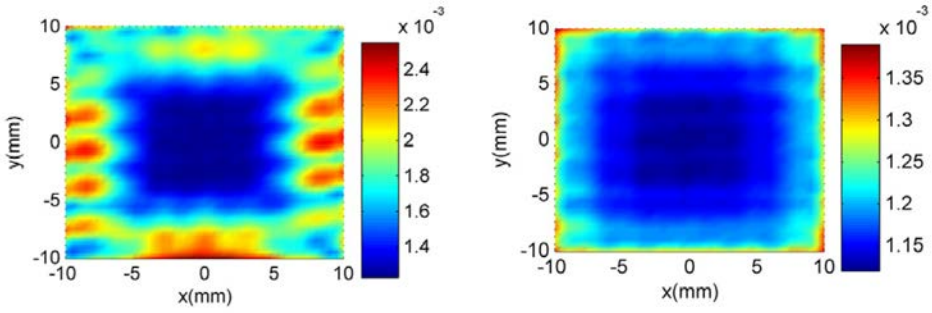

(a) Before fusion *(b) After fusion*

Figure 2.47 Comparison of uncertainty in Gaussian process fusion (Yin et al., 2016)

A one-to-one linkage model to the one-to-many neighbourhood linkage model was extended (Xia et al., 2011) to improve the misalignment problem. Figure 2.48

shows the measurement setup of the proposed data fusion method. Simulation and actual measurement results both showed significant improvement.

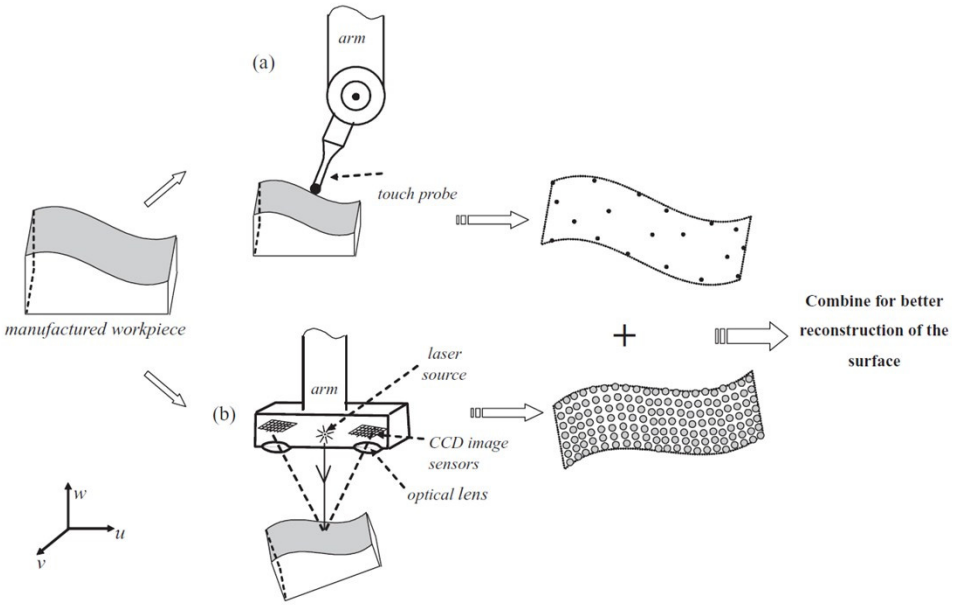

Figure 2.48 Fusion of two resolution data from a CMM using a tough probe and laser scanner (Xia et al., 2011)

2.4.3 In-situ/In-process measurement systems

In some circumstances, when the workpiece is extremely large and heavy, or re-machining of the workpiece is required to correct the machining error, in-situ or on-machine measurement of the workpiece is greatly needed, since it is not possible to take the huge and heavy workpiece off the machining facility and put it on a metrology instrument; another reason is that the re-alignment error is not acceptable. In-situ or on-machine measurement is a challenge to metrology since most of the measurement instruments have a stringent requirement for the environment while this is incompatible with the machining environment. This requires the in-situ measurement instrument to be fast, robust and adaptive to the machining facilities. An in-situ real-time measurement instrument was developed (Jiang, 2011) for microstructured surfaces. The system was based on the wavelength division multiplexing (WDM) and

graphics processing unit (GPU) technologies. The WDM technology implemented phase-to-depth conversion with large measurement ratios in terms of range to resolution. The GPU technology speeded up the analysis of the optical interferograms to realize real-time calculation. Figure 2.49 shows the schematic diagram and the prototype of the system.

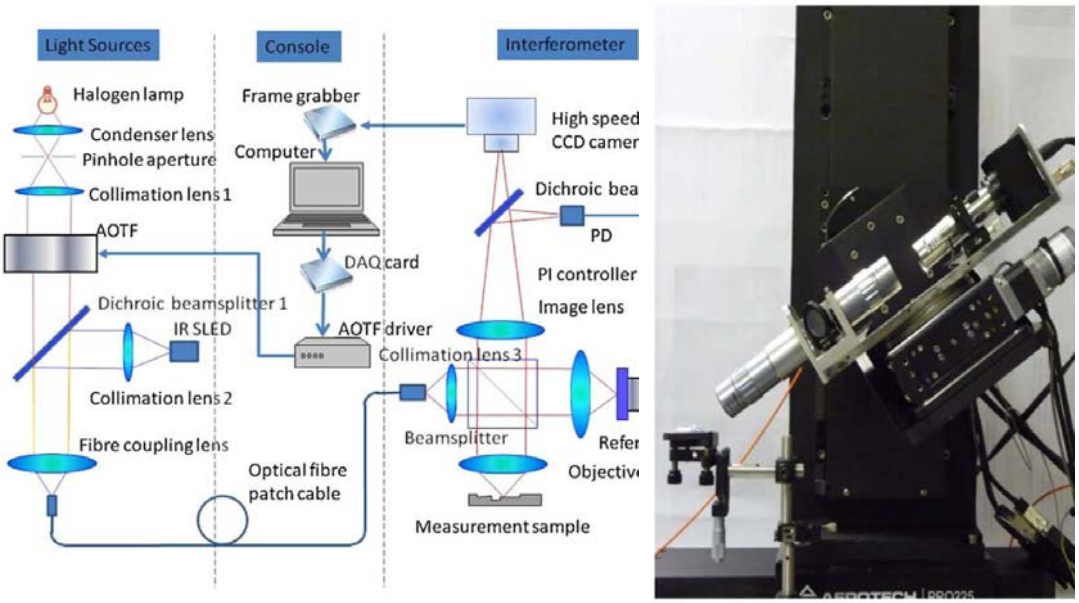

(a) The schematic diagram *(b) The prototype system*

Figure 2.49 The wavelength scanning interferometry system (Jiang, 2011)

An in-situ measurement instrument based on scanning tunnelling microscopy (STM) was developed (Ju et al., 2014). The system can be used to measure the machine surface and correct the form error by using the fast tool servo (FTS) on the machine. The tool tip of the FTS and the tip of the STM are aligned to avoid distortion of the machined and measured surface. The STM measures the surface of the workpiece by using the spiral scanning method which is efficient. The highly accurate measurement principle of the STM and the accurate motion of the machine tool ensure the accuracy of the measurement result. Figure 2.50 shows the measurement device built in the machine tool and the schematic of the system.

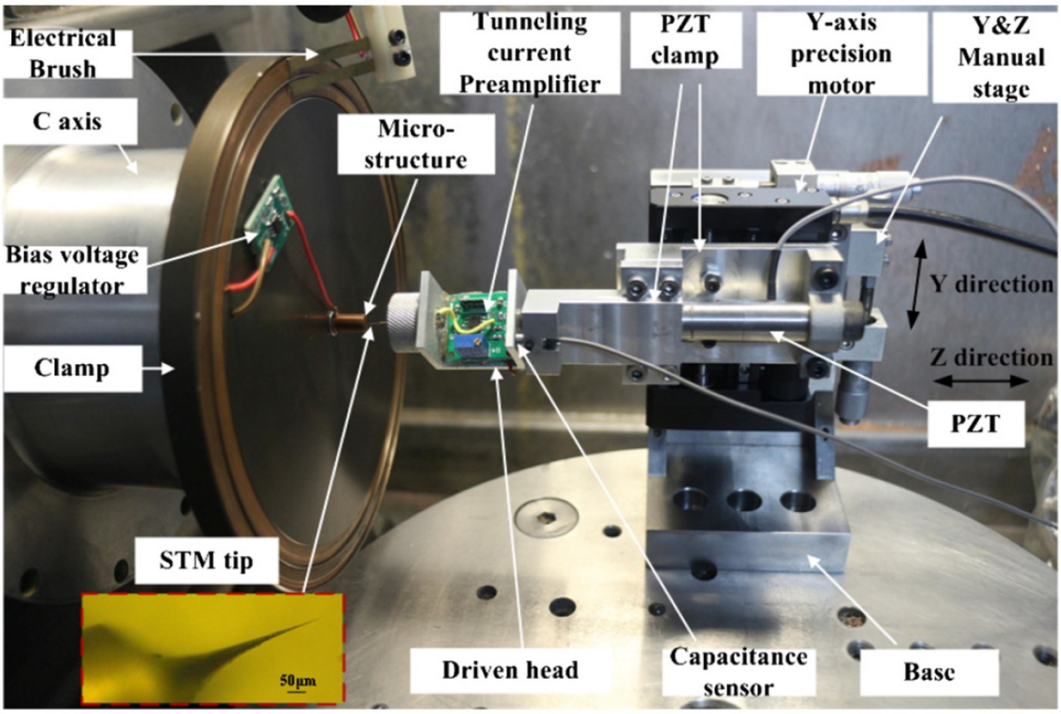

(a) Photograph of the built-in STM measurement device

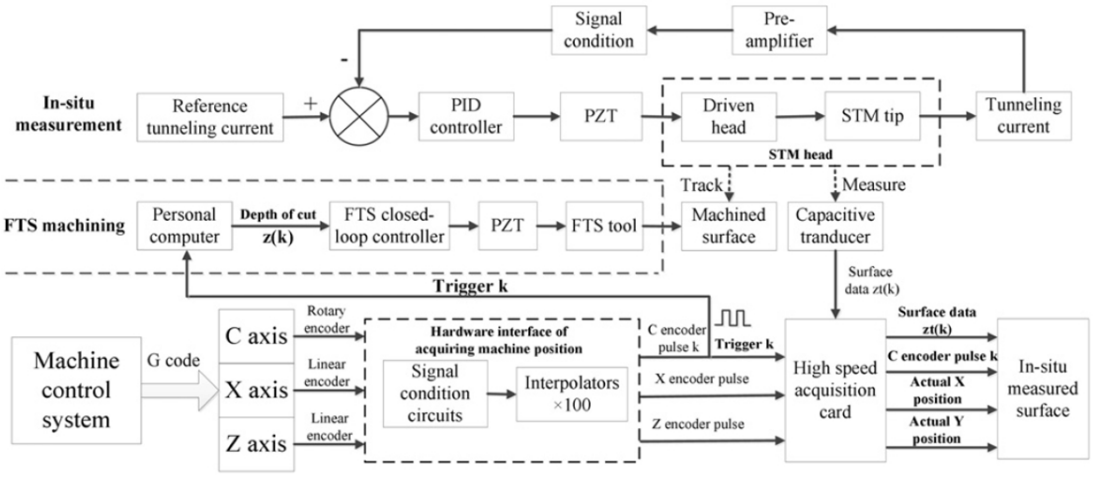

(b) Schematic view of the system

Figure 2.50 The STM in situ measurement system (Ju et al., 2014)

In-situ metrology systems are also available for some commercial machining facilities. One example is the on-machine Stitching Interferometer (OMSI) mounted on the IRP 200 ultra-precision polishing machine as shown in Figure 2.51. The OMSI is mounted on the H-axis parallel to the axis of the polishing head to conduct the on-

machine measurement. The OMSI utilizes a compact simultaneous-phase interferometer from 4D Technologies to overcome the vibration issue in the environment. The workpiece is mounted on the C axis of the polishing machine. The measurement process follows the tool path in the same way as the polishing one since this can make the OMSI follow the workpiece's surface according to its local slope. Since the OMSI can only measure a small part of the surface of the workpiece, i.e. perform the sub-aperture measurement, the sub-aperture measurement is then stitched to generate a holistic measurement result of the whole surface. As a result, the accuracy of the measurement result is not dependent on the accuracy of the motion axes.

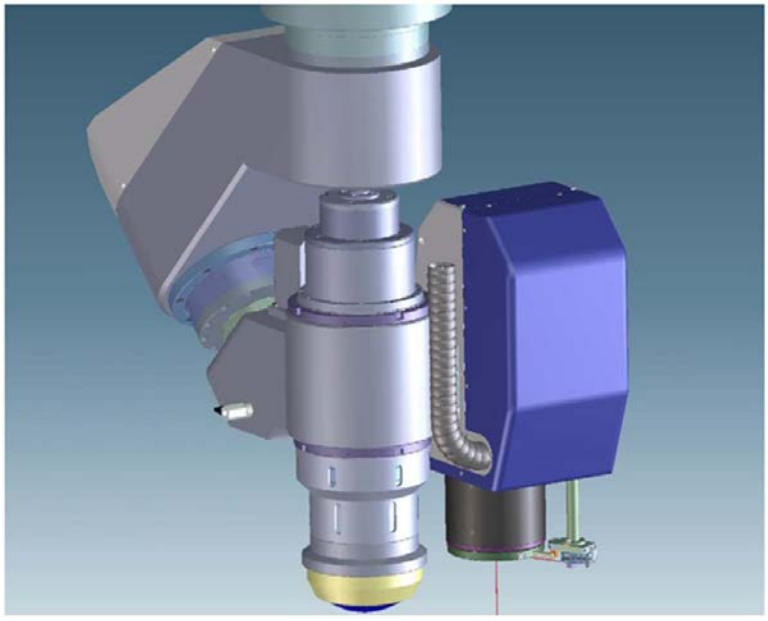

Figure 2.51 The OMSI – On Machine Stitching Interferometer Mounted to the H-axis (polishing head) of an IRP 1200 (Zeeko, 2010)

For some advanced commercial CNC machines such as the MIKRON HPM 600U/HPM 800U (GF AgieCharmilles, 2015), a touch probe is selectable as an option which can perform in-situ measurement. However, the in-situ measurement system has to be installed by the machine tool developer since the electrical interface of the machine tool is not open to users and researchers. Moreover, further development of

the machine tools is forbidden or it will violate the operational conditions of the machines.

2.4.4 High dynamic range measurement

Many optical components have large dimensional size and small feature size, while the accuracy requirement of both the large form and the small features are stringent. One of the examples is the roller in the roll-to-roll industry where the roller is up to 2 metres in size and has microstructure with a size of about 10 µm. Figure 2.52 shows one of the ultra-precision lathes (Oh et al., 2013) that can machine rollers with

Figure 2.52 Photograph of the ultra-precision lathe (Oh et al., 2013)

a diameter of 600 mm and a length of 2,500 mm, while the minimum pitch is 20 µm as shown in Figure 2.53. Measurement of both large-scale features and small-scale features poses the high dynamic range challenge. This is because most of the measurement instruments have to strike a balance between measurement range and resolution. Figure 2.54 shows the relationship of the measurement area to the resolution and where the high dynamic range measurement requirement falls into.

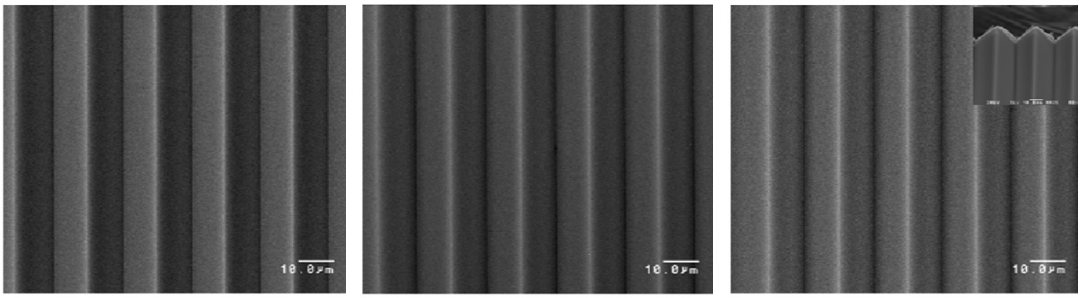

(a) Near the head stock *(b) At the centre* *(c) Near the tail stock*

Figure 2.53 Machined 20 µm pitch prism microstructure on the roll: (a) near the head stock, (b) at the centre, and (c) near the tail stock (Oh et al., 2013)

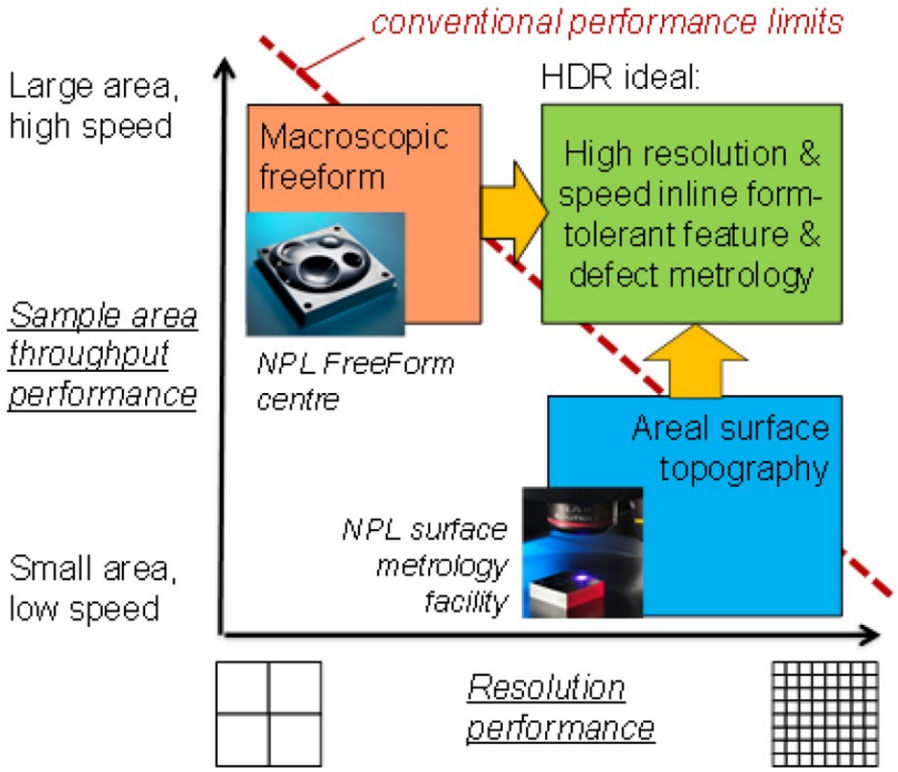

Figure 2.54 Space representing the challenges of high dynamic range metrology (Leach et al., 2013)

2.5 Measurement uncertainty and traceability

All measurements have associated uncertainty. According to the Guide to the Expression of Uncertainty in Measurement (GUM) (BIPM, 2008), the measurement

uncertainty can be classified as type A and type B. Type A evaluation of standard uncertainty can be regarded as an experimental method, where the experimental standard deviation is determined by:

$$s(q_k) = \sqrt{\frac{1}{n}\sum_{j=1}^{n}(q_j - \bar{q})^2} \tag{2.5}$$

Type B evaluation of standard uncertainty is not obtained from repeated measurements and it is determined by scientific judgment, which is based on all the available information. The information includes previous measurement data, the experience or general knowledge of the material and instruments, manufacturer's specifications, data provided in calibration and other certificates and uncertainties assigned to reference data taken from handbooks (BIPM, 2008).

The measurement uncertainties for different sensors are different. The approaching direction and speed, probe indexing angle and spring pressure are affected by the measurement uncertainty of the touch trigger probe (Cauchick-Miguel and King, 1998). The surface roughness and surface local gradient are influenced by the measurement uncertainty for the scanning white light interferometer (Liu et al., 2015). For the laser scanning method, the measurement uncertainty is largely affected by the surface reflection (Liu et al., 2016) and incident angle of the sensor (Mahmud et al., 2011). For the CCD camera used in 2D measurement, the measurement noise of the sensor chip and the measurement algorithm such as edge detection are also affected by the measurement uncertainty.

In a multi-sensor measurement environment, the measurement uncertainties of different kinds of sensors need to be determined in advance. The evaluation method can be done by experiments or the sensors' specifications. This can be determined by

using a mathematical model such as the Gaussian process machine learning method (Williams and Rasmussen, 2006). The advantage of using mathematical modelling is that it is more efficient and it can determine the measurement uncertainty according to the environmental conditions since they may have an influence on the measurement result. However, the accuracy of the modelling and its influencing factors need to be determined in depth.

The Monte Carlo method was firstly developed by Stanislaw Ulam (Metropolis, 1987) and has become an important tool. It utilizes random sampling to obtain numerical results and is powerful in determining the propagation of uncertainty especially in non-linear complex systems. The method has also become one of the standards for the determination of measurement uncertainty (JCGM, 2008b). The Monte Carlo method was utilized (Ren et al., 2012a, Cheung et al., 2012) to develop a task-specific uncertainty analysis method for least-squares-based form characterization of ultra-precision freeform surfaces. This method was also extended to evaluate the uncertainty in the form characterization of ultra-precision freeform surfaces on coordinate measuring machines (Cheung et al., 2014).

Traceability measurement relies heavily on a standard artefact which is traceable to the SI unit. An artefact for traceable freeform measurements on coordinate measuring machines was developed (Savio and De Chiffre, 2002) which is based on a Modular Freeform Gauge (MFG) concept. The MFG configuration is shown in Figure 2.55. NPL (McCarthy et al., 2011) developed a freeform artefact for verification of non-contact measuring systems as shown in Figure 2.56.

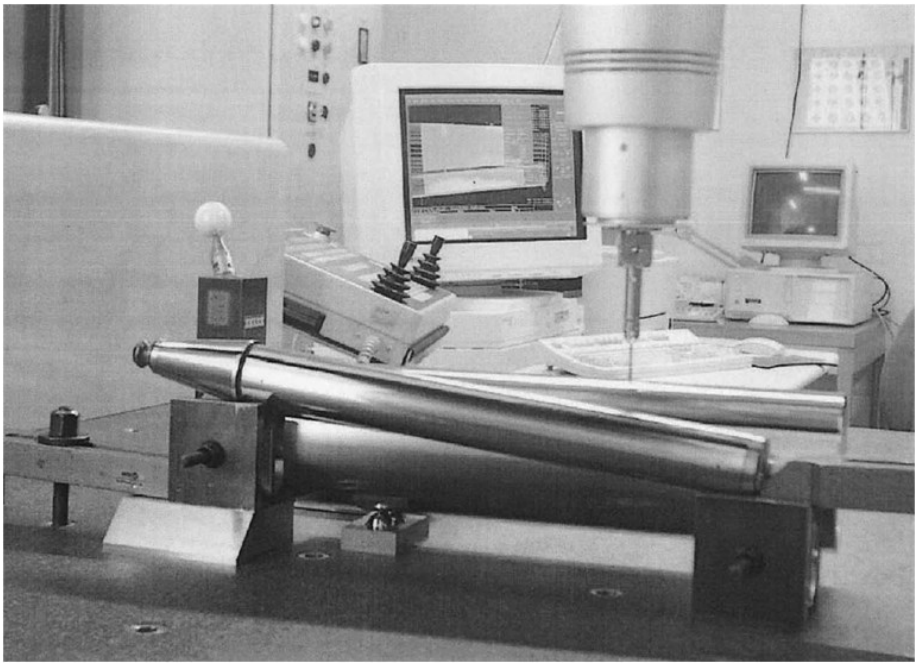

Figure 2.55 MFG configuration on a CMM during the uncertainty assessment procedure (Savio and De Chiffre, 2002)

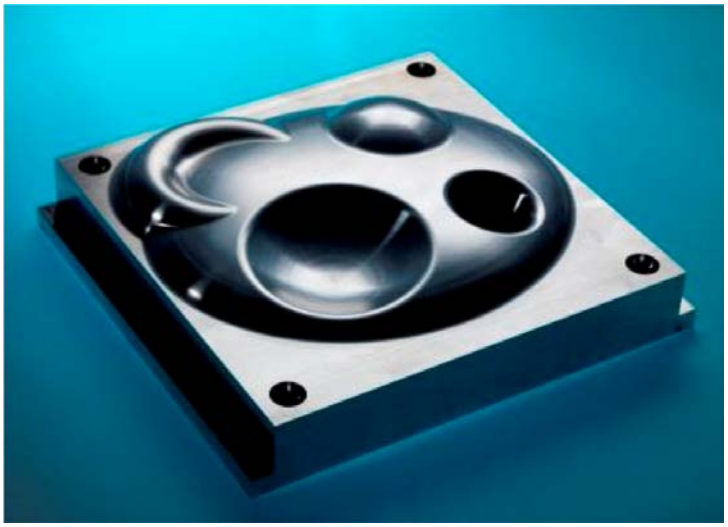

Figure 2.56 Photograph of NPL freeform artefact (McCarthy et al., 2011)

2.6 Summary

Nowadays, freeform surfaces are widely used in many areas such as optics, aerospace, biomedical, etc. They have been playing an important role in the past decades. The research and development trend is paying more attention to the study of

freeform surfaces. With the development of science and technology, the freeform surfaces are more complex, higher in accuracy, and smaller in surface finish. This poses a lot of challenges not only for the design and manufacturing process, but also for the measurement process, since the measurement is greatly needed to determine conformity with the design.

According to the literature review in the previous sections, the large amount of applications of freeform surfaces determine the intensive needs for manufacturing and measurement of freeform surfaces. The development of the design of freeform surface is on one hand pushing the development of the techniques of manufacturing and measurement of freeform surfaces. On the other hand, it is also limited by the capability of manufacturing and measurement of freeform surfaces.

Nowadays, there are a lot of techniques which are capable of manufacturing and measurement of freeform surfaces and these techniques are also developing fast towards greater accuracy, volume, efficiency, etc. Nevertheless, there are still a lot of problems in the manufacturing and measurement of freeform surfaces since the requirements of the freeform surfaces are becoming more and more stringent. This is particularly true for their measurement due to the reason that the accuracy of the measurement is usually required to be one order better than that of manufacturing. There is a large amount of research work focused on the study of single-sensor measurement of freeform surfaces. However, there is relatively little research focused on the multi-sensor measurement for surface metrology. Moreover, most of the measurement methods are offline measurements, so how to incorporate the measurement device to perform in-situ measurement on the machining facilities is a research trend and challenge in the industry.

Based on the intensive review of the literature, there is a need to develop a generic data modelling method for the multi-sensor CMM measurement of freeform surfaces. Moreover, a data fusion algorithm is greatly needed to combine the measurement data from different sensors to generate a fused dataset with higher accuracy. A generic in-situ measurement method is essential for measuring the freeform surface without taking off the workpiece from the machining facilities. At the current status, there is still a large research gap to fill regarding the implementation of the multi-sensor data fusion measurement method with the in-situ measurement instruments. The development of a generic method which is applicable to in-situ measurement combining the multi-sensor data fusion algorithm is most significant for the further development of precision surface measurement.

Chapter 3 Gaussian process-based stitching measurement of freeform surfaces

3.1 Introduction

In precision metrology, one of the challenges is the high dynamic range measurement of precision surfaces, which requires both large measurement area and high-resolution data (Leach et al., 2013). This is particularly true for the measurement of surfaces with multi-scale characteristics which possess large-scale topography and small-scale microstructured features. Due to the limited field of view (FOV) and resolution of the camera, it is difficult to obtain a result under a satisfactory range in a single measurement when multi-scale information is acquired. One of the possible solutions is to perform multiple measurements and stitch the results together to form a dataset with a larger area to reveal the large topographic information without losing the high-resolution information so as to characterize the microstructure pattern (Bray, 1997).

Stitching has been reported for a sub-aperture stitching interferometer for both spherical and flat surface measurements (Liang et al., 2013, Chen et al., 2005, Chen et al., 2015, Jansen et al., 2006). A phase-correlation method was used (Preibisch et al., 2009) to find the translation matrix between image pairs and perform global optimal stitching. A sub-aperture stitching and localization algorithm was proposed (Chen et al., 2007) for spherical and planar surfaces. Moreover, they developed a coarse-to-fine stitching strategy. A simultaneous reverse optimizing reconstruction method was developed (Zhang et al., 2015) which is based on a system modelling technique for aspheric sub-aperture stitching interferometers. An optimal stitching planning method

was used (Ye et al., 2016) to measure large aspheric optical surface with a ±4 mm range of probe and 20% of overlapped region. The accuracy of the sub-aperture stitching method was evaluated (Wiegmann et al., 2011) by using virtual experiments and they found that the overall accuracy of stitching result outperformed the direct measurement method by a factor of about 3. For surface measurement instruments such as coherence scanning interferometers, which are widely used for precision surface measurement, some commercial products can provide a stitching function for relatively flat surfaces (Fleig et al., 2003).

However, most of the stitching methods make use of six degrees of freedom for registration in the overlapped regions and the computational complexity is relatively high. For instance, the Iterative Closest Point (ICP) algorithm (Besl and McKay, 1992) has $O(N_p N_x)$ complexity for a single iteration. For a registration with N_t and N_q initial translations and rotations, the total complexity is $O(N_p N_x N_t N_q)$ which is considerably high. Moreover, the error caused by the stitching algorithm is accumulated when the number of sub-surface measurements is increasing, especially for the rotational error, which is difficult to be compensated. It was pointed out (Marinello et al., 2007) that the translational error is the biggest source of error, while the Roll, Pitch and Yaw error can be as small as several arc-secs. With the help of high-precision linear stages in which the rotational error can be considered to be minimal or negligible, the registration can be simplified to a three degrees of freedom translation problem with the complexity being reduced to $O(N_p N_x N_t)$.

In this chapter, a stitching method is developed based on the Gaussian process and image registration together with edge intensity data fusion. The working principle of the Gaussian process and image registration-based stitching method is discussed. A

simulation and actual measurement were conducted to verify the performance of the method. Some technical aspects are also discussed and the edge effect was found to be improved as compared with the traditional method. The results of the experiments show that the proposed method is suitable for stitching the measurement results of areal measurement instruments, which provides a technically feasible solution for high dynamic range optical measurement of precision surfaces.

3.2 The principle of the Gaussian process and image registration-based stitching method

A framework of the proposed Gaussian process and image registration-based stitching method is shown in Figure 3.1. First, the sub-aperture measurement datasets are modelled using a Gaussian process (Williams and Rasmussen, 2006) so as to obtain the mean surfaces, which can reduce the registration error caused by measurement noise and outliers. The datasets are converted to two-dimensional images and the images are registered by using an intensity-based algorithm, which can determine the (x, y) translation parameters. The MATLAB Image Registration Toolbox (Gonzalez et al., 2004) was used to implement this algorithm. In this study, 20% overlapped area was determined for the measurement datasets and chosen for the best balance between efficiency and accuracy (Wyant and Schmit, 1998). After the (x, y) translation, the z axis translation was calculated by using the least-squares error method so as to minimize the z distance between the two mean surfaces. The next step was to calculate the data in the overlapped region with an edge intensity data fusion method. Finally, the datasets were stitched together to form a dataset combining all the (x, y, z) translation information, and the overlapped data were fused.

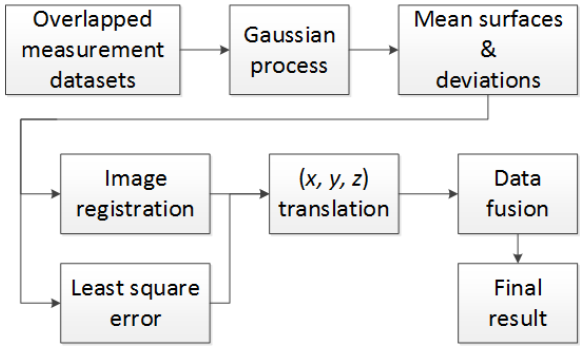

Figure 3.1 Diagram of the Gaussian process-based stitching method

3.2.1 Gaussian process modelling of original surfaces

Noise in the measurement processes and outliers in the result may affect the registration accuracy. It is pointed out that both the standard deviation of the noise and the mean error of the noise have influence on the registration error (Huang et al., 2016). Traditional methods utilize filtering techniques to remove noise and outliers in the original measurement results. However, filtering is limited by distortion and edge effects (Brinkmann et al., 2001). The Gaussian process modelling involved in the proposed stitching method aims to improve the registration accuracy (Liu et al., 2016b). The original measurement results can be described as a discrete function of $z(x_i, y_i)$, which means the z-coordinate of the i-th point is a function of the lateral position (x_i, y_i). Let $\mathbf{v}_i = (x_i, y_i)$, the measured datasets can be represented as $z(\mathbf{v}_i)$, $i = 1, 2, \ldots, N$, where N is the number of points. The measurement process can be considered as a Gaussian process which is a stochastic process, with underlying surface and measurement noise, which can be expressed as:

$$z(\mathbf{v}_i) = f(\mathbf{v}_i) + \varepsilon \tag{3.1}$$

where $f(\mathbf{v}_i)$ is the underlying surface and ε is the measurement noise, which is assumed to have a Gaussian distribution $\varepsilon \sim N(0, \sigma_\varepsilon^2)$, with zero mean and σ_ε^2

variance. It should be noted that the mean and variance for the measurement noise denote the systematic error and random error of the measurement. With a carefully calibrated measurement instrument, the systematic error is negligible thus it is set to zero.

In order to model the underlying surface, Gaussian process modelling was used in this study. A Gaussian process is a random process where the probability distribution function in regard to the associated observation is normal and the joint probability distributions associated with any finite subset of the observations are also normal. A Gaussian process can be modelled as a mean function and a covariance function, which are expressed as:

$$f(\mathbf{v}_i) = GP(m_z(\mathbf{v}_i), k_z(\mathbf{v}_i, \mathbf{v}_j)) \tag{3.2}$$

where $m_z(\mathbf{v}_i)$ is the mean function, $k_z(\mathbf{v}_i, \mathbf{v}_j)$ is the covariance function with $m_z(\mathbf{v}_i) = E[z(\mathbf{v}_i)]$ and $k_z(\mathbf{v}_i, \mathbf{v}_j) = E[(z(\mathbf{v}_i) - m_z(\mathbf{v}_i))(z(\mathbf{v}_j) - m_z(\mathbf{v}_j))]$. The mean function represents the expected z value at $\mathbf{v}_i$ while the covariance function represents the variance of the z value when $\mathbf{v}_i = \mathbf{v}_j$ and the covariance between the z values when $\mathbf{v}_i \neq \mathbf{v}_j$.

In this study, the mean function was designed to be zero function since the measured surface is unknown. Moreover, a squared exponential function is used to represent the covariance of the Gaussian process model:

$$k_z(\mathbf{v}_i, \mathbf{v}_j) = \sigma_z^2 \exp\left(-\frac{\left\| \mathbf{v}_i - \mathbf{v}_j \right\|^2}{2l^2} \right) \tag{3.3}$$

where $\|\mathbf{v}_i - \mathbf{v}_j\|$ is the distance between $\mathbf{v}_i$ and $\mathbf{v}_j$, σ_z^2 is the constant variance of the Gaussian process model and l is the characteristic length-scale.

The parameters of the covariance function corresponding to unit characteristic length-scale and unit signal standard deviation were firstly initiated to be zeros and the likelihood parameter was initiated to be $\log(0.1)$, which denotes the standard deviation of the noise to be 0.1 mm. The parameters of the Gaussian process were then optimized by minimizing the negative log marginal likelihood. After the parameters were optimized, the mean surface and the covariance surface of the measured data were determined. In this study, the implementation of the Gaussian process modelling was based on the Gaussian processes for machine learning (GPML) MATLAB toolbox (Rasmussen and Nickisch, 2010).

3.2.2 Image registration for x-y alignment

After Gaussian process modelling, the mean surfaces of the original measurement datasets were modelled. The three-dimensional datasets were then projected onto the x-y plane as 2D images. Image registration was used to align the overlapped images. Generally, there are four types of transformation for image registration, i.e. translation, rigid, similarity and affine. In this study, the translational type was used since only x-y translation was considered. The technique used in the image registration process is intensity-based automatic image registration. The intensity-based automatic image registration is an iterative process. Firstly, the overlapped regions of two images were identified; one was set as the fixed image while the other was set as the moving image. Hence, a metric, an optimizer and the transformation type were specified. Since the measurement datasets were taken from the same instrument, the metric and optimizer were configured to be monomodal. For each iteration, a transformation matrix applied to the moving image was determined

and the metric was determined by comparison with the transformed moving image with a bilinear interpolation to the fixed image. The iteration stopped when the stop condition was detected, i.e. when it reached a point of diminishing returns or reached the maximum number of iterations.

3.2.3 z-axis alignment

In the previous process, the overlapped region was registered in the x-y direction. The datasets on the z axis were then aligned to minimize the distances of the overlapped surfaces. This is a least-squares problem and the objective function can be determined by:

$$F = \sum_{i=1}^{N} \left\| z_i' - z_i \right\|^2 \tag{3.4}$$

where z_i' and z_i are the corresponding points in the two surfaces, and z_i' denotes the translated data points of the alignment process along the z axis. Translation along the z axis can be determined by minimizing the objective function in Eq. (3.4).

3.2.4 Data fusion for the overlapped area

When all the (x, y, z) translation information was determined, the datasets could be stitched together to form an overall measurement result. For the overlapped region, the data were fused together with a data fusion algorithm. There are many kinds of data fusion methods such as simple or weighted means, weighted least-squares fusion and residual approximation-based fusion (Wang et al., 2015). In this study, the edge intensity data fusion method (Chen et al., 2008) was used to have a better transition in the overlapped region. For a dataset $R(m \times n)$, the edge intensity is defined by:

$$E_{R(i,j)} = \left| \frac{f(i,j) - \bar{m}}{m \times n - 1} \right| \tag{3.5}$$

where $\bar{m} = \sum_{i=1}^{n} \sum_{j=1}^{m} \frac{f(i,j)}{m \times n} \, (i = 1,...,n, \; j = 1,...,m)$

For two datasets $A(i,j)$ and $B(i,j)$, the weighting functions were determined by:

$$\begin{cases} W_{A(i,j)} = \dfrac{E_{AR(i,j)}}{E_{AR(i,j)} + E_{BR(i,j)}} \\ W_{B(i,j)} = \dfrac{E_{BR(i,j)}}{E_{AR(i,j)} + E_{BR(i,j)}} \end{cases} \tag{3.6}$$

Hence, the fused dataset F was determined by:

$$F(i,j) = W_{A(i,j)} \times A(i,j) + W_{B(i,j)} \times B(i,j) \tag{3.7}$$

3.3 Simulation verification

To verify the proposed stitching method, a simulation using MATLAB was conducted. As shown in Figure 3.2, a synthetic large sinusoidal surface was considered to be the targeted measuring surface. The design of the surface is determined by:

$$z = a\left[\sin(x) + \cos(y)\right] + GN(0, 0.1) \tag{3.8}$$

where $a = 0.002$ mm, $x, y \in [0, 100]$ mm and $GN(0, 0.1)$ is the added Gaussian noise with zero mean and 0.1 μm variance.

The peak-to-valley distance of the surface was 8 μm. The area of the whole surface was 100 mm ×100 mm which was divided into nine sub-regional measurements. The highlighted area in Figure 3.2 denotes the overlapped area between nearby measurement datasets.

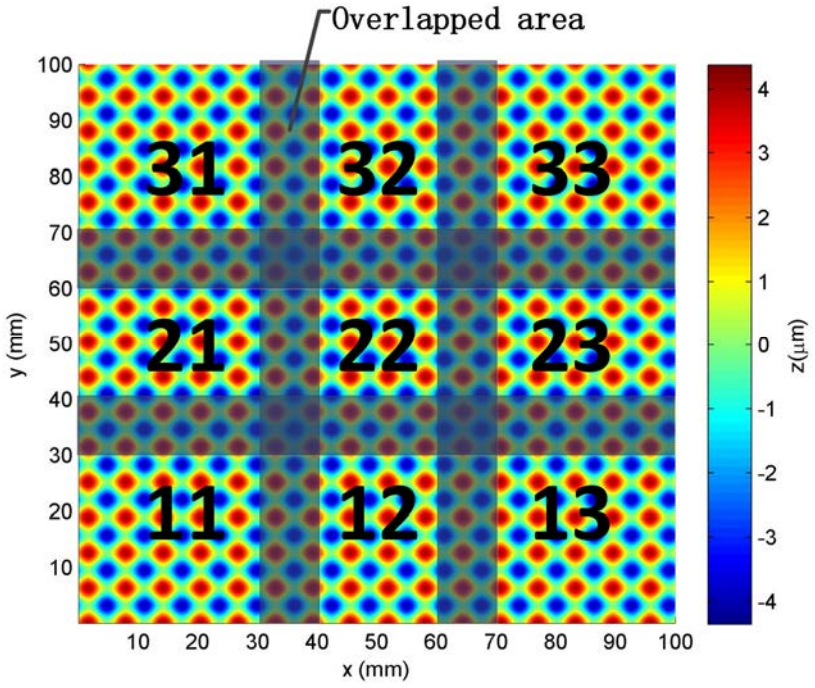

Figure 3.2 Simulated stitching surface

As shown in Figure 3.2, the nine measurements had the same size and are marked as 11~13, 21~23 and 31~33 respectively. The area of the individual measurement was 40 mm ×40 mm while the width of the overlapped area (highlighted in the figure) was 8 mm, which was 20% of the width of the dataset, as suggested elsewhere (Wyant and Schmit, 1998).

After the Gaussian process, the mean and variance of the original surface were determined and Figure 3.3 shows the mean and variance of surface 11. The result shows that the standard deviation of the majority of the modelled surface was about 0.1 μm, while the simulated noise level was 0.1 μm, which demonstrates the effectiveness of the Gaussian process.

The mean surfaces after Gaussian process modelling were then transformed into 2D grayscale images to perform image registration. The registration result of the overlapped regions of surface 11 and surface 12 are shown in Figure 3.4. The result shows that the two sub-regions are well registered.

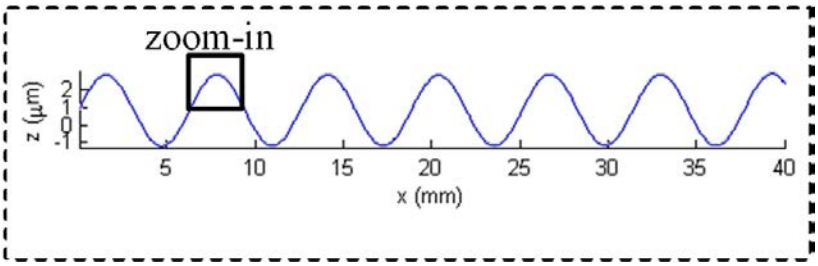

(b) 2D section profile illustrating mean and covariance

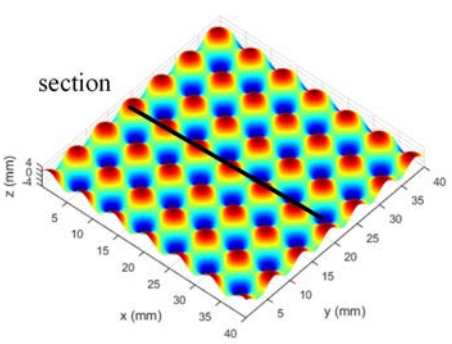

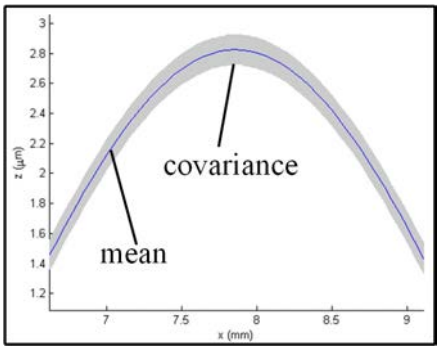

(a) Original surface *(c) Zoom-in view of mean and covariance*

Figure 3.3 Results after Gaussian process

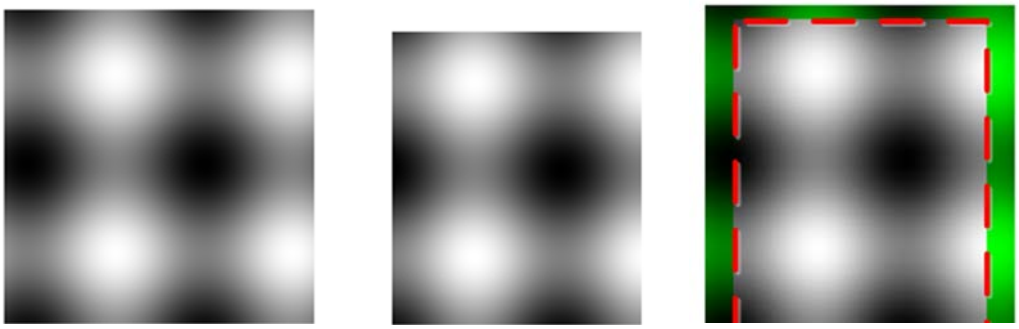

(a) Fixed image *(b) Moving image* *(c) Registered pair images*

Figure 3.4 Zoom-in view of one pair the registration results

After image registration, the (x,y) translation relationship of the nearby regions was determined. The next step was to register the datasets in the z direction. The process was to search for the minimum distance between the two mean surfaces by using the least-squares error method. For surface region 11 and surface region 12, the

aligned result is shown in Figure 3.5. The result shows that the two surfaces were well registered in the z direction.

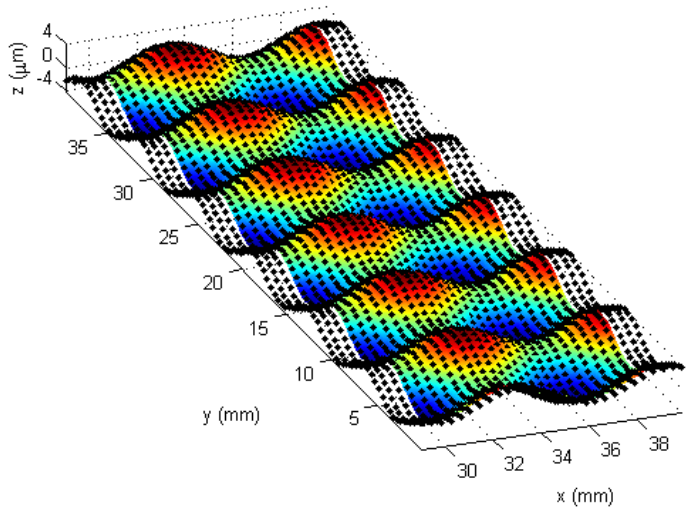

Figure 3.5 Z axis registration result. The colour-coded surface represents surface 11 and the black dots represents surface 12

After the (x, y, z) translation information was determined, the sub-regions could be stitched together. The data in the overlapped area were recalculated with the edge intensity method. Figure 3.6 shows the final stitching result which shows that

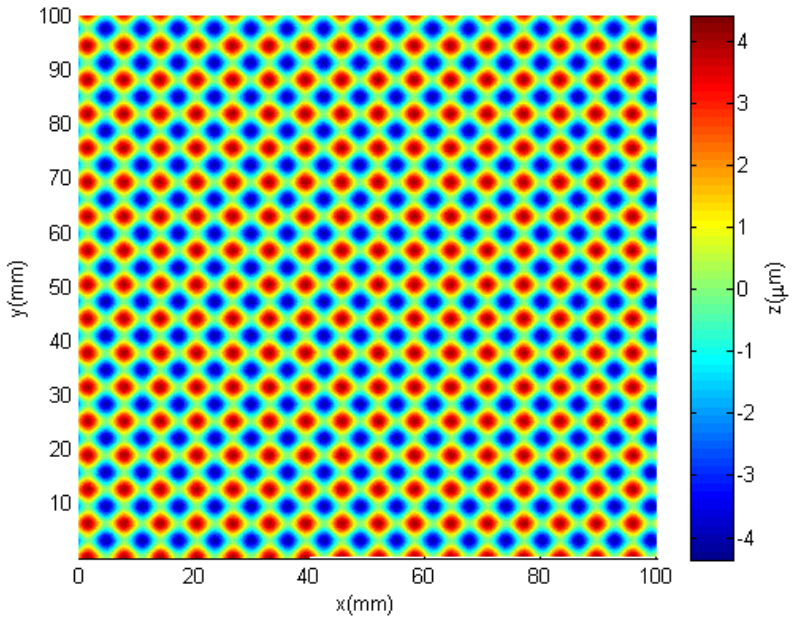

Figure 3.6 Stitching result

there were no obvious edges in the overlapped area. This infers that the datasets were well stitched. The final stitching result was also registered to the original design surface with an iterative closest point (ICP) method (Besl and McKay, 1992) and the error map was determined as shown in Figure 3.7. The root-mean-square (RMS) value of the error map is 0.108 μm. The error map shows that the error is evenly distributed and in most areas is close to zero. It is also interesting to note that the error in the central area is relatively small as compared to that in the surrounding areas. This is mainly caused by the accumulated errors in the image registration process since the surrounding datasets principally need more connections than those in the centre. The different patterns for the error map related to two nearby sub-surfaces are the results from the registration error for the proposed method. The result shows that the registration error is in the level of sub-micrometre and the error for each nearby registration is randomly distributed, which depends on the data in the overlapped area. This is demonstrated well in different datasets for the x direction, i.e. for different groups of datasets (11, 12, 13), (21, 22, 23) and (31, 32, 33), the errors are distributed (from left to right) in an increasing manner, first decreasing and then increasing manner, and decreasing manner, respectively.

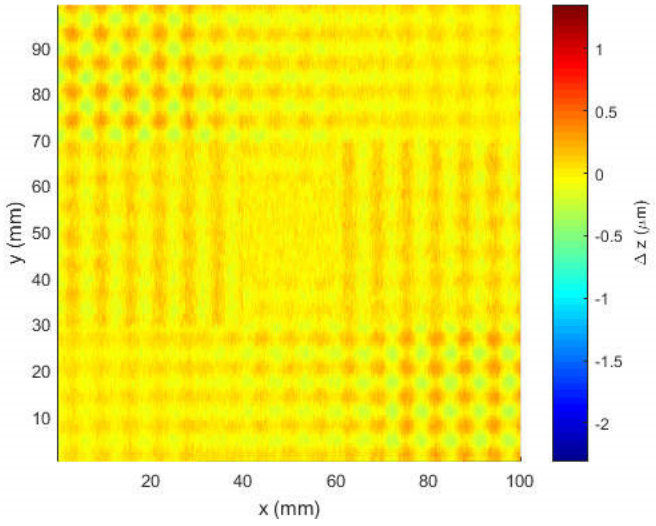

Figure 3.7 Error map comparing with the design surface

3.4 Experimental verification and discussion

3.4.1 Measurement of a diamond-turned sinusoidal surface

To demonstrate the practical usage of the proposed method, a stitching measurement experiment was conducted by measuring a diamond-turned sinusoidal surface by a commercial coherence scanning interferometer (CSI, with a 20× object lens and 1× and 0.55× zoom lens). The surface was measured in a manner similar to the simulation in a 3×3 matrix arrangement. The area of a single measurement was approximately 0.3 mm ×0.2 mm. A set of nearby sub-surfaces with an overlap marked region is shown in Figure 3.8 and all the original measurement data are shown in Figure 3.9.

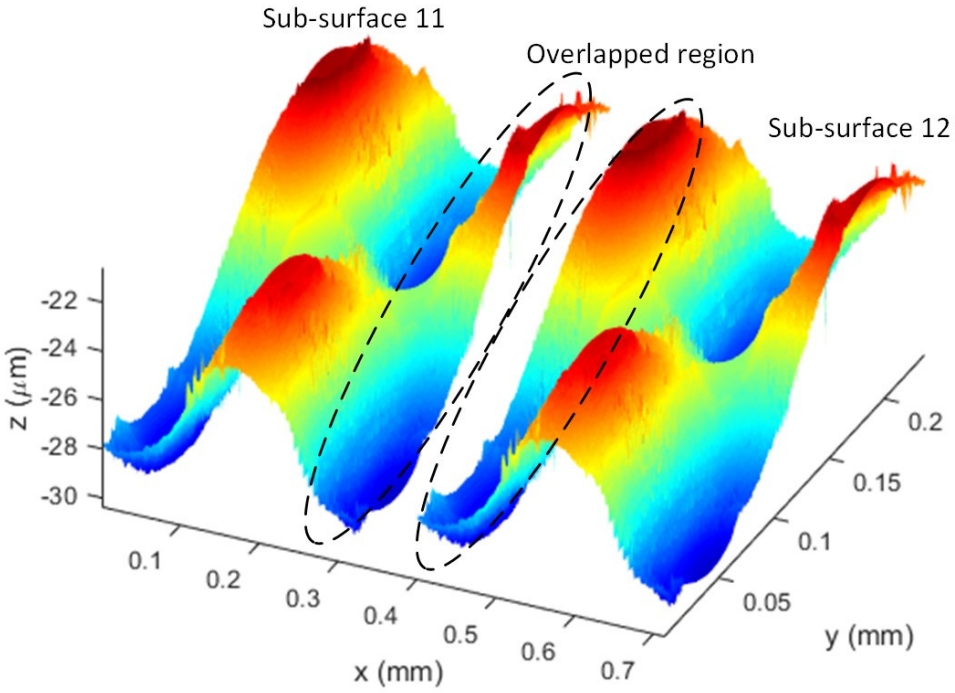

Figure 3.8 The 3D dataset for two nearby sub-surfaces, the overlap region is marked with dash line

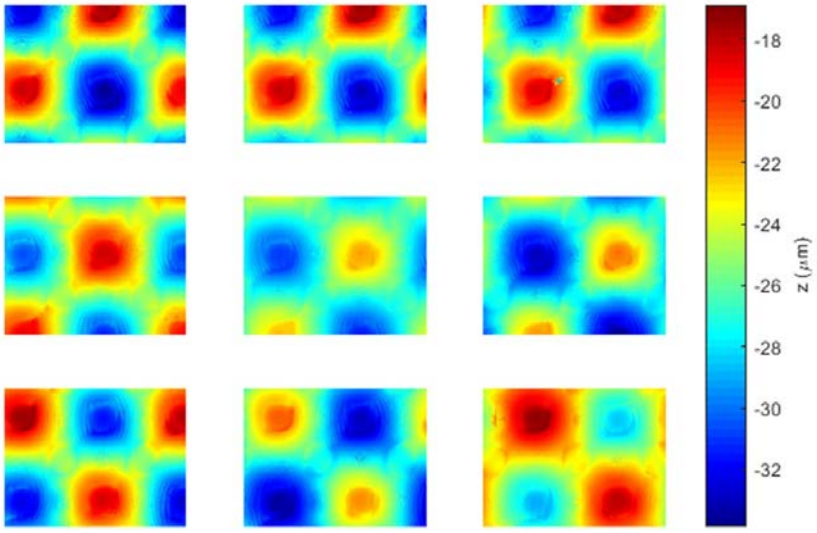

Figure 3.9 Original data (measurement size of each dataset is approximately (0.3×0.2) mm and the colour bar gives height information in micrometres)

After obtaining the individual measurement data, the data were modelled by a Gaussian process. The mean surfaces of the measurement data are shown in Figure 3.10. The result shows that the overall deviations of the mean surfaces are greatly

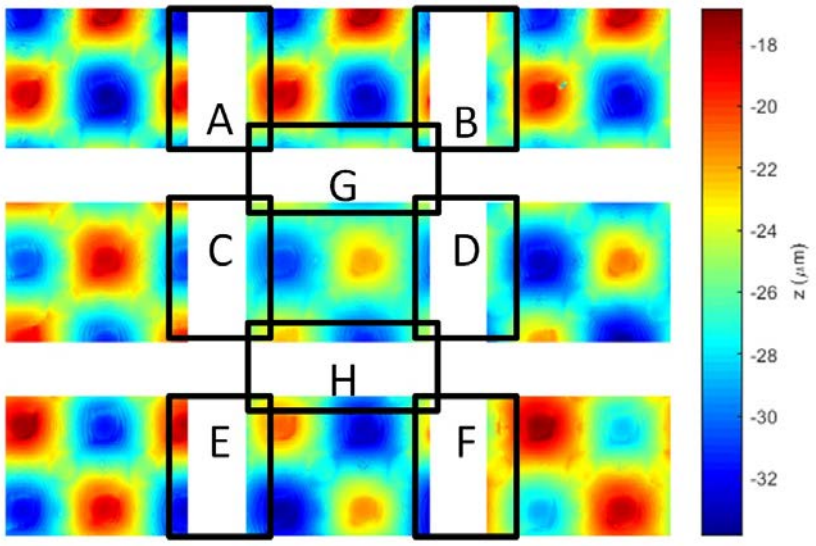

Figure 3.10 Mean surfaces of Gaussian process (measurement size of each dataset is approximately (0.3×0.2) mm and the colour bar gives height information in micrometres) and overlapped regions

reduced and the intensities of the subfigures have better uniformity. This result demonstrates the advantage of using a Gaussian process to model the measurement data, especially when the measurement noise is large or the measurement result is affected by obstacles such as dust and/or scratches. As reported by some researchers elsewhere (Huang et al., 2016), the registration error is about 25 μm for a noise level with standard deviation of 150 μm.

The mean surfaces were then converted to grayscale images and image registration was conducted among the eight overlapped regions which are highlighted in Figure 3.10 with notations of A to H. Figure 3.11 shows the registration results of the overlapped regions for region A. The results show that the sub-surfaces are registered well.

(a) Fixed image (b) Moving image (c) Registered pair images

Figure 3.11 One pair of the image registration result

After image registration for the x-y plane, the next step was to perform z axis alignment. After that, the coordinate transformation information for all the three axes was obtained and the registration process was finished. In this study, the z axis alignment was divided into two steps. The first step aimed to align the sub-surfaces in the horizontal direction and the other step was used to align the sub-surfaces in the vertical direction. The horizontal direction step aimed to register the sub-surface in the horizontal direction, i.e. regions A and B, regions C and D, and regions E and F as

shown in Figure 3.10. The vertical direction step aimed to register the sub-surface in the vertical direction, i.e. regions G and H. As a result, the relationships of all the sub-surfaces were determined.

3.4.2 Results and discussion

After registration, the overlapped data were fused together by using the edge intensity method. Figure 3.12 shows the final stitching result after data fusion while Figure 3.13 shows the stitching result provided by the CSI software. The details of the stitching result from the proposed method and that from the CSI software are also shown in Figure 3.12 (b, c) and Figure 3.13 (b, c). The stitching result shows that the sub-surfaces were well stitched together and the stitching result provided by the proposed method had better edge transition features than the stitching result provided by the CSI software. Figure 3.12 (b, c) shows a better transition area than Figure 3.13 (b, c) at the region near the edge of the original sub-surfaces. This is due to the

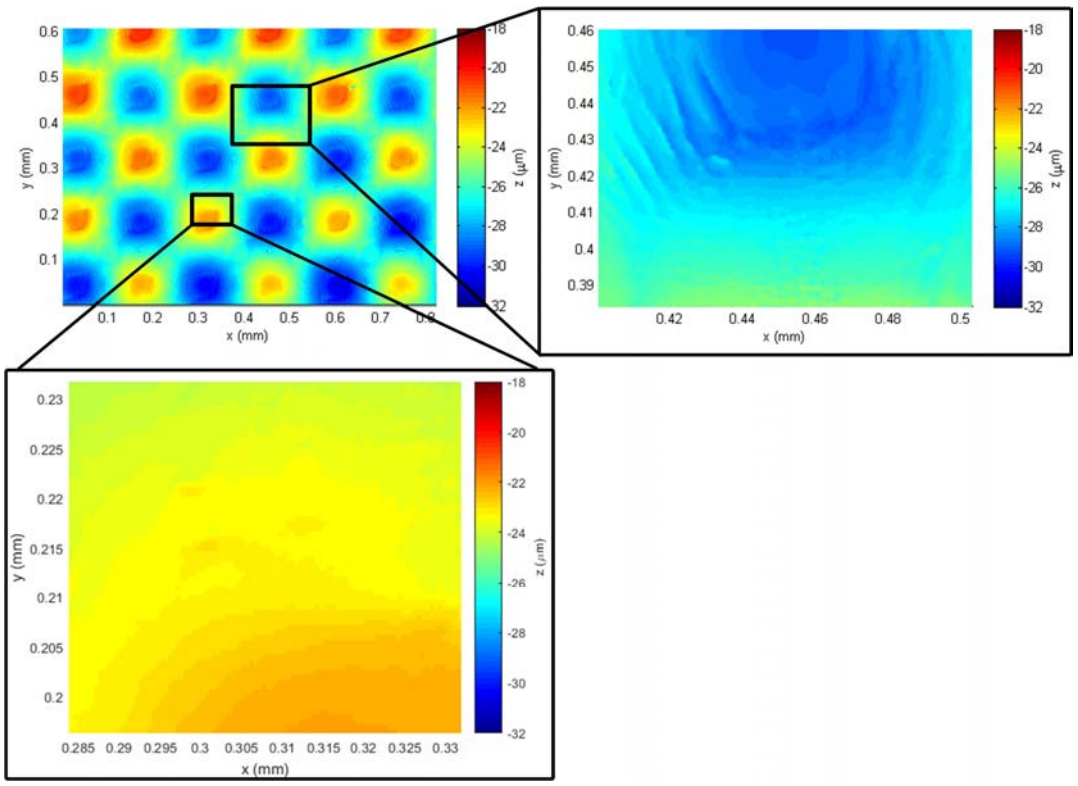

Figure 3.12 Stitching result of the proposed method

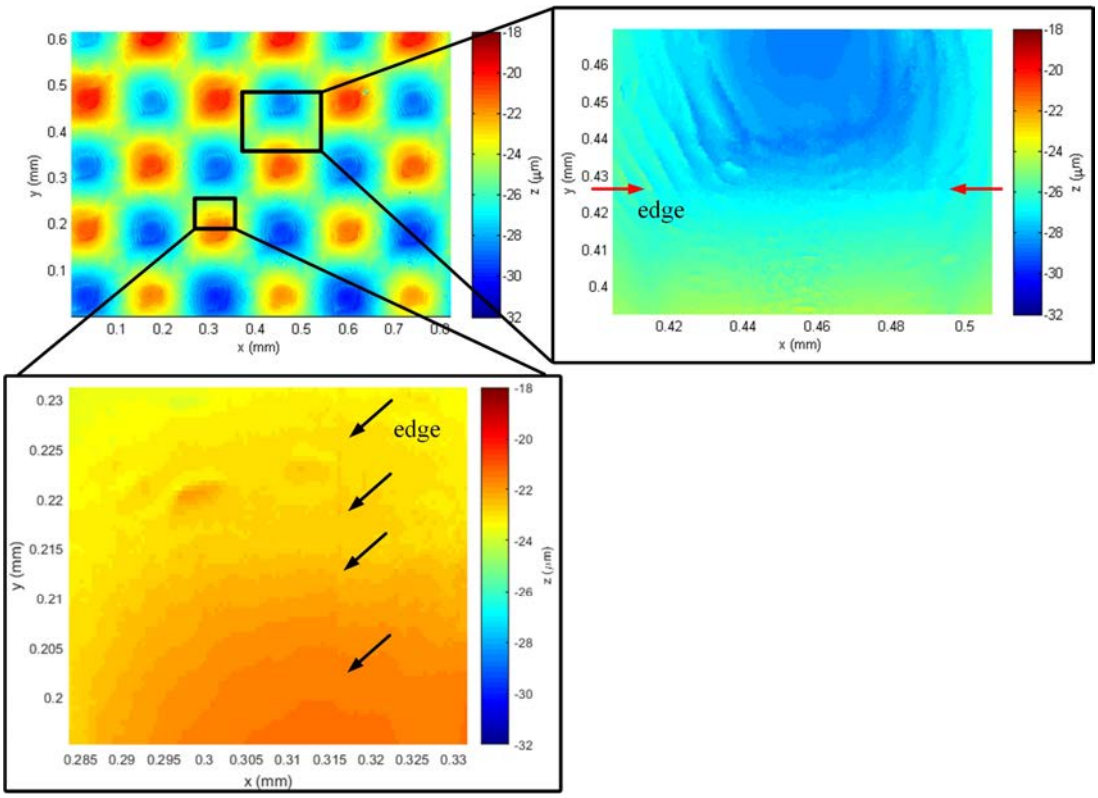

Figure 3.13 Stitching result of the CSI software

characteristics of the edge intensity data fusion method, which combines both the features in the overlapped surfaces to generate a fused dataset. This is particularly useful when the two overlapped sub-surfaces have significantly different measurement results due to measurement noise.

The final stitching result was also compared with that measured with a lower magnification setting (20×0.55) in a single shot measurement. To reduce the effect of the measurement noise, especially the different noise levels at different magnifications (Liu et al., 2015), the form error of the stitching method was evaluated. Both the results of the stitched measurements and the single shot measurement were bandwidth-matched through a Gaussian filter. The cut-off spatial wavelength of the Gaussian filter was 0.01 mm. Moreover, the edge area with half a cut-off length was removed since this area had a large edge effect, which significantly affected the evaluation of the

results. The two filtered results were then registered with the ICP method and the error map calculated as shown in Figure 3.14. The single shot measurement had a measurement area of 0.6 mm ×0.4 mm which covered the central part of the final stitching measurement result and contained all the edges in the stitching result. The root-mean-square (RMS) error with the proposed method was 0.31 µm. Similarly, the stitching result provided by CSI software was also registered to the single shot measurement result by using the same method and the error map was obtained as shown in Figure 3.15. The RMS error was 0.27 µm. The result shows that the errors were of the same order and both were evenly distributed.

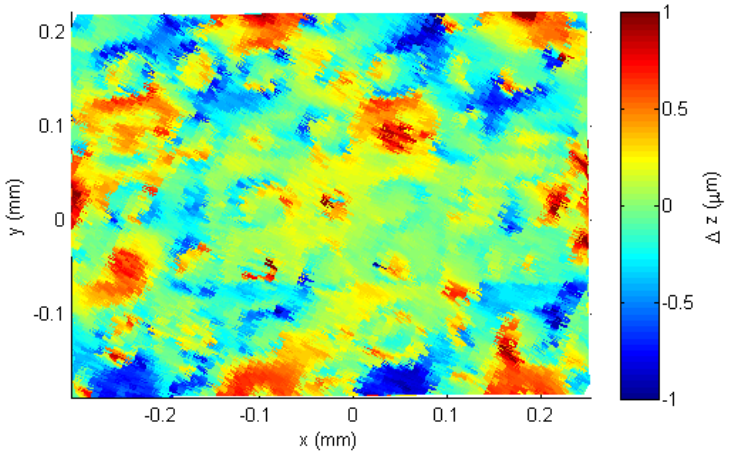

Figure 3.14 Proposed stitching error comparing with a single shot measurement

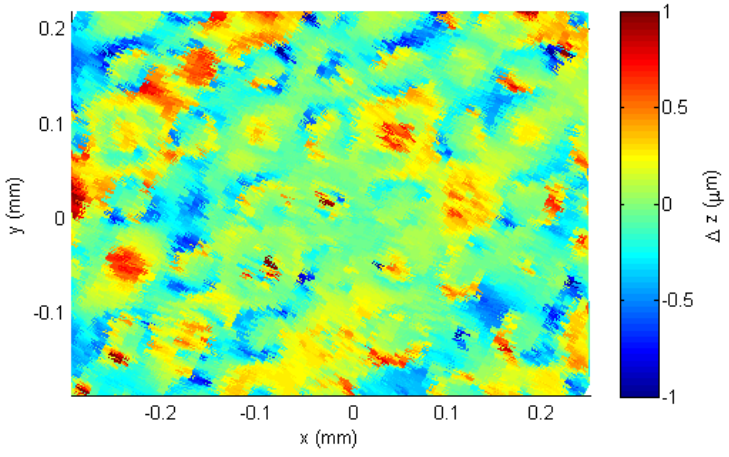

Figure 3.15 CSI stitching error comparing with a single shot measurement

The proposed stitching method makes use of a precision moving stage to simplify the stitching process from a 6 DOF problem to 3 DOF problem. For the stitching strategy as shown in the measurement experiment, the length of each sub-surface is about 0.3 mm, to achieve the sub-micrometre stitching accuracy. The angular motion error can be calculated to be less than $\arctan(\frac{0.1\ \mu m}{0.3\ mm}) = 0.33\ mrad$. This requirement can be achieved by many commercial linear stages such as those from Aerotech (2017), whose rotation error is as small as 0.050 mrad.

The proposed stitching method is a generic method which is suitable for measuring various kinds of surfaces with different patterns or different local curvatures. However, its measurement ability is affected by the measuring range of the sensor and the moving stage. For the experiments as demonstrated in this study, the measurement ability is limited by the hardware of the instrument: measurement range in the z direction of the CSI and the X-Y stage, which results in the fact that it can only measure surfaces which are relatively flat. With the help of additional rotational stages, the measurement for high-departure aspheric surfaces becomes possible with the modified proposed method. The corresponding translation motion should be modified to the rotation motion. For surfaces with relatively less features such as those with a longer spatial period, the registration accuracy may be largely affected, and pre-processing can be implemented to improve the registration accuracy by using the invariant features such as Gaussian curvature (Ren et al., 2012b). This will be considered in future work. On the other hand, for some workpieces without strong periodical patterns, the small local difference caused by surface roughness and discontinuity of materials can still be treated as features to ensure the registration accuracy (Liu et al., 2016a).

3.5 Summary

In this chapter, a Gaussian process and image registration-based stitching and data fusion method is presented for high dynamic range optical measurement of precision surfaces, which is based on a Gaussian process, image registration and data fusion techniques. For the overlapped areas, the data are fused with the edge intensity method. A simulation and actual measurement were conducted for verification of the method. For both simulation and actual measurements, nine (3×3) sub-surface measurements were stitched together to form a holistic measurement result. The stitching result exhibited improved edge transition features in the overlapped area, which is an advantage, especially for overlapped sub-surface measurements that have significantly different results. It is concluded that the proposed method is technically feasible and suitable for sub-aperture stitching for large area measurement with optical instruments.

Chapter 4 Gaussian process-based multi-sensor measurement of freeform surfaces

4.1 Introduction

Nowadays, modern optical components with freeform surfaces are widely used since they have the advantages of excellent optical performance and functionality (Fang et al., 2013b). Due to the high accuracy requirement and geometrical complexity of freeform surfaces, this poses a lot of challenges in their design and manufacture as well as their measurement since the measurement process needs to characterize the machined freeform surfaces so as to determine conformance with the design. The coordinate measuring machine (CMM) (Hocken and Pereira, 2016) is one of the most important geometrical measurement devices. Equipped with the most widely used touch trigger probe with high repeatability, it provides traceable and accurate measurement results over a relatively large measurement range, and is well accepted in the industry for coordinate measurement due to its flexibility and accuracy (Savio et al., 2007). For modern CMMs, after several decades of development since they were first invented, their measurement accuracy is ensured by sophisticated designed hardware and a carefully controlled environment together with specific software.

At present, there is a research and development trend towards multi-sensor CMMs since the measurement capability of these machines can be significantly enhanced by integrating multiple sensors (Weckenmann et al., 2009). This provides a unique functionality comparison with the single-sensor CMM machines. Currently, there are many commercialized multi-sensor CMMs available in the market. For instance, ZEISS O-INSPECT (Carl Zeiss Industrial Metrology, 2016) is equipped with a contact sensor, imaging sensor and white light distance sensor, which is able to

provide fast inspection by the image sensor and high-accuracy 3D measurement results by the contact sensor and white light distance sensor. Werth VideoCheck (Werth Messtechnik GmbH, 2016) is designed to be equipped with many kinds of sensors such as trigger probe, fibre probe (Schwenke et al., 2001) and video sensor, which provide measurement ability for small features with the help of the small-diameter fibre probe down to 20 μm, as well as quick checking with the fast trigger probe and image sensor. Hexagon Optiv Classic (Hexagon, 2016) provides a vision sensor and a touch trigger probe, while Nikon (Nikon Metrology NV, 2016) enhances the true 3D multi-sensor measurement by combining a vision sensor, laser auto-focus sensor, tactile sensor and rotary indexer.

On one hand, the measurement range, resolution and flexibility are largely enhanced by the complementary different characteristics of various sensors. On the other hand, in regard to most of the multi-sensor CMMs equipped with additional non-contact optical sensors which provide the ability to obtain the actual form and position of the workpiece, this functionality offers a solution to reduce the measurement error caused by the geometrical error such as form error and alignment error. Moreover, further improvement of the measurement accuracy can be accomplished by data fusion from different sensors.

Measurement with different kinds of sensors also provides the possibility to improve the overall measurement accuracy by data fusion techniques. Most of the multi-sensor CMMs enhance the measurement ability according to the sensor's characteristics. Although this provides high flexibility for measuring different features and samples by selecting different sensors installed on multi-sensor CMMs, there is still plenty of space for research and development when the integration of measured datasets from different sensors is taken into account. At the current stage of surface metrology, there are quite a number of studies focused on combining the datasets from

different sensors to generate holistic results with improved measurement accuracy. A cooperative fusion method was developed (Galetto et al., 2015) for a distributed multi-sensor large-volume metrology system which combined datasets from angular and distance measurements. However, it only worked for measurement using angular and distance sensors to determine the 3D positions of the measured points and could not be used for CMMs. A Gaussian process modelling method was used (Colosimo et al., 2014) to combine highly accurate low-density CMM data with low-accuracy high-density data from a laser scanner. The two datasets were linked together using a "linkage" model by introducing the scaling and shifting factors to correct the systematic error. The result showed that the measurement uncertainty of the fused data can be reduced as compared with the results from single measurement. This method was similar to the one proposed elsewhere (Qian and Wu, 2008), but it dealt with surface metrology problems instead of mechanical material design and modelling of food processors.

The Gaussian process is a machine learning process (Williams and Rasmussen, 2006) which is largely used in research areas such as image processing. Recently it has been used in surface metrology. The Gaussian process to form error assessment for CMMs was utilized (Xia et al., 2008). With the proposed Gaussian modelling method, the designed geometric form, systematic manufacturing errors and random manufacturing errors were decomposed. Simulation and actual measurement data demonstrated the improvement as compared to the traditional method. A Gaussian process-based modelling method and data fusion method was developed (Yin et al., 2016) for the measurement of complex surfaces. The result showed that the measurement uncertainty of the fused dataset was smaller than for the original datasets. However, the systematic error was not considered in the proposed method. The one-to-one linkage model to the one-to-many neighbourhood linkage model was extended

(Xia et al., 2011) to improve the misalignment problem. Simulation and actual measurement both exhibited significant improvement. In the multi-sensor CMM scenario, a generic method for data modelling and data fusion method is greatly needed to meet the development trend of the emerging market of multi-sensor metrology. Moreover, in the presence of measurement noise and form error, there is a need to study the accuracy of the data modelling method and how it is affected by these factors. The performance of the data modelling method should also be verified experimentally.

In order to address these issues, this chapter proposes a Gaussian process-based data modelling and maximum likelihood-based data fusion method for multi-sensor CMM measurement of freeform surfaces. The datasets from both sensors were first modelled by using the Gaussian process to obtain the mean surfaces and the covariance surfaces, which represent the underlying surfaces and the associated uncertainties. Hence, the mean and covariance surfaces were then fused together under the maximum likelihood principle. The method was verified through a series of simulations and real measurement conducted on a multi-sensor CMM, followed by detailed discussions including some failure situations to which much attention should be paid. The proposed Gaussian process and maximum likelihood-based method establishes a generalized, sensor-independent data fusion framework for multi-sensor CMMs, which provides an indispensable solution for integrating different sensor data for measuring high-precision freeform surfaces. The influence of the form error and measurement noise on the accuracy of the data modelling method is also discussed and was demonstrated in a series of experiments, while the performance of the Gaussian process modelling of the measurement uncertainty was also experimentally verified.

4.2 Gaussian process-based data modelling and maximum likelihood-based data fusion method

The schematic diagram of the proposed Gaussian process-based data modelling and maximum likelihood-based data fusion method is shown in Figure 4.1. It starts with the measurement of the workpiece with a laser sensor and a touch trigger probe. The measurement data of both the laser sensor and the touch trigger probe were modelled by using the Gaussian process method to obtain the estimated mean surface and associated measurement uncertainty. The next step is registration of two datasets into a common coordinate system. The measured data of the CMM is presented in point cloud format while the global coordinate information for different sensors was determined in advance in the calibration process, by using a standard calibration ball. However, it is reported (Shen and Menq, 2001) that there still exists small residual error due to the sensor's relative position at the micrometre level.

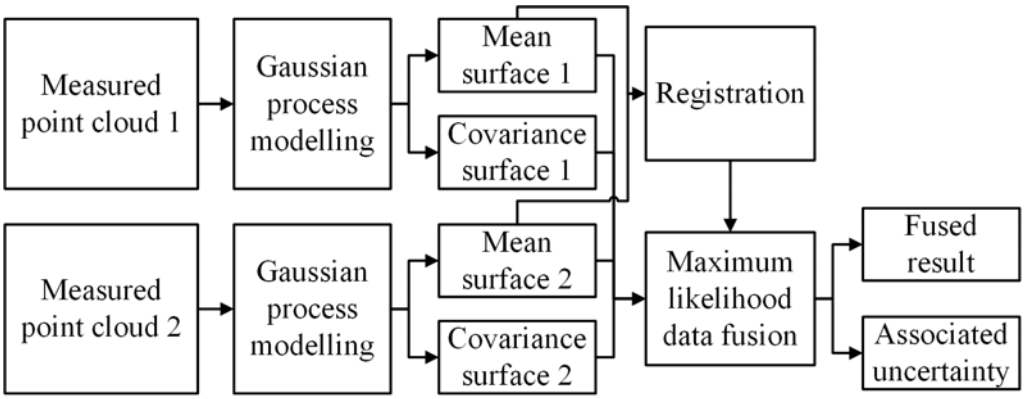

Figure 4.1 Framework of the Gaussian process and maximum likelihood-based data fusion method

To further improve the overall accuracy of the measurement process, the datasets were registered to a single coordinate system with the Iterative Closest Point (ICP) algorithm (Besl and McKay, 1992). This aimed to perform fine registration since the coordinate information of the two datasets was calibrated before the measurement

so coarse registration was undertaken. After registration, the datasets were aligned in a common coordinate system. Since the measurement datasets were modelled by using the Gaussian process, the mean surfaces and the covariance surfaces of the measurements were obtained. Hence, the mean surfaces and the covariance surface were fused together using the maximum likelihood data fusion algorithm. In the end, the best estimated underlying surface and its associated measurement uncertainty were determined. In this method, Gaussian process modelling is used to determine the underlying surface and its measurement uncertainty for each measurement from different sensors. With the measurement data and the uncertainty information, the maximum likelihood data fusion is used to determine the best estimated result in a statistical manner. The details of the proposed generalized data fusion method are explained in the following sections.

4.2.1 Gaussian process data modelling

In the present study, both the measured point clouds measured by laser sensor and touch trigger probe were modelled by the Gaussian process. A Gaussian process is a generalization of the Gaussian probability distribution (Williams and Rasmussen, 2006). There is always noise in the measurement process and the noise is supposed to follow the Gaussian distribution. In the CMM measurement process, the measurement result can be determined by Equation (4.1).

$$z = f(\mathrm{x}) + \varepsilon, \tag{4.1}$$

where z is the measurement result and $f(\mathrm{x})$ is the true value, respectively, x is the input vector which represents the measured location, and ε is the measurement error which is of Gaussian distribution with zero mean and variance σ_n^2; hence,

$$\varepsilon \sim N(0, \sigma_n^2), \tag{4.2}$$

It should be noted that the mean and variance for the measurement noise denote the systematic error and random error of the measurement. Similar to the assumption in Eq. (3.1) in Chapter 3, with a carefully calibrated measurement instrument, the systematic error is negligible thus it is set to zero.

Since the true value $f(\mathrm{x})$ is unknown and hereby the aim of using the Gaussian process is to estimate the $f(\mathrm{x})$ and the associated uncertainty, the Gaussian process can be defined by the mean function and covariance function:

$$f(\mathrm{x}) \sim GP(m(\mathrm{x}), k(\mathrm{x}, \mathrm{x}')), \tag{4.3}$$

where $m(\mathrm{x})$ is the mean function at location x and $k(\mathrm{x}, \mathrm{x}')$ is the covariance function evaluated at x and x', which can be determined by:

$$\begin{aligned} m(\mathrm{x}) &= E[f(\mathrm{x})], \\ k(\mathrm{x}, \mathrm{x}') &= E[(f(\mathrm{x}) - m(\mathrm{x}))(f(\mathrm{x}') - m(\mathrm{x}'))], \end{aligned} \tag{4.4}$$

Equation (4.3) shows that $f(\mathrm{x})$ is fully defined by the mean function and covariance function in Gaussian process modelling. Once the model is established, any prediction f_* at new location X_* can be given by the joint distribution of the measured values and the function values at the test locations:

$$\begin{bmatrix} z \\ \mathrm{f}_* \end{bmatrix} \sim N\left(0, \begin{bmatrix} K(X,X) + \sigma_n^2 I & K(X,X_*) \\ K(X_*,X) & K(X_*,X_*) \end{bmatrix}\right), \tag{4.5}$$

where I is the identity matrix, X is the matrix of the measured locations and X_* is the matrix of predictive locations; σ_n^2 is the noise variance.

Hence, the predictive equation for Gaussian process regression is:

$$\mathrm{f}_* | X, z, X_* \sim N\left(\bar{\mathrm{f}}_*, \mathrm{cov}(\mathrm{f}_*)\right), \tag{4.6}$$

where

$$\bar{\mathrm{f}}_* = E[\mathrm{f}_*|X, z, X_*] = K(X_*, X)[K(X, X) + \sigma_n^2 I]^{-1} z,$$
$$\mathrm{cov}(\mathrm{f}_*) = K(X_*, X_*) - K(X_*, X)[K(X, X) + \sigma_n^2 I]^{-1} K(X, X_*), \tag{4.7}$$

In the present study, Gaussian process modelling was undertaken by using the Gaussian processes for machine learning (GPML) toolbox (Rasmussen and Nickisch, 2010). The mean function was chosen to be zero mean since the underlying surface is supposed to be unknown. Choosing zero mean surface may affect the accuracy and efficiency of Gaussian process modelling; it may be considered to combine Gaussian process modelling with local topological consideration (Bukkapatnam and Cheng, 2010) in future study. The covariance function was chosen to be the most popular squared exponential function which can model smooth surface and is infinitely differentiable (Williams and Rasmussen, 2006), since the measured surface in this study was continuous freeform surface. The same covariance function used in the previous chapter which is determined by Eq. (3.3) is utilized in this study.

Since the Gaussian process is a machine learning process, the parameters of the model are first initiated and then optimized by minimizing the negative log marginal likelihood. This is implemented in an iterative process in the GPML toolbox.

4.2.2 Maximum likelihood data fusion

After Gaussian process modelling, the mean surface and the associated uncertainty at any positions can be estimated for each measurement. For a particular multi-sensor CMM measurement which considers measurement datasets from two different sensors, the mean surfaces and the associated measurement uncertainties can be denoted as m_1, m_2 and u_1, u_2, respectively. As the measurement noise is governed by Gaussian distribution, the probability of both of the two measurements obtaining result *m* can be determined by:

$$p(m|m_1,{u_1}^2)=\frac{1}{u_1\sqrt{2\pi}}e^{-\frac{(m-m_1)^2}{2{u_1}^2}},$$
$$p(m|m_2,{u_2}^2)=\frac{1}{u_2\sqrt{2\pi}}e^{-\frac{(m-m_2)^2}{2{u_2}^2}}, \tag{4.8}$$

For a particular measurement at a specified position, the likelihood of both sensors observing m is:

$$\begin{aligned}p(m|m_1,{u_1}^2,m_2,{u_2}^2)&=p(m|m_1,{u_1}^2)p(m|m_2,{u_2}^2)\\&=\frac{1}{2\pi u_1u_2}e^{-\left[\frac{(m-m_1)^2}{2{u_1}^2}+\frac{(m-m_2)^2}{2{u_2}^2}\right]},\end{aligned} \tag{4.9}$$

The natural logarithm of the above function is:

$$\ln\left(p(m|m_1,{u_1}^2,m_2,{u_2}^2)\right)=-\left[\frac{(m-m_1)^2}{2{u_1}^2}+\frac{(m-m_2)^2}{2{u_2}^2}\right]+C, \tag{4.10}$$

where $C=\ln(\frac{1}{2\pi u_1u_2})$.

According to the maximum likelihood principle, the best estimation for m can be determined when Equation (4.10) is maximized, which yields:

$$\hat{m}=\arg\max[\ln\left(p(m|m_1,{u_1}^2,m_2,{u_2}^2)\right)], \tag{4.11}$$

Hence,

$$\begin{aligned}\frac{\partial\ln\left(p(m|m_1,{u_1}^2,m_2,{u_2}^2)\right)}{\partial m}&=\frac{\partial(-\left[\frac{(m-m_1)^2}{2{u_1}^2}+\frac{(m-m_2)^2}{2{u_2}^2}\right]+C)}{\partial m}\\&=0,\end{aligned} \tag{4.12}$$

Thus,

$$\frac{2(\hat{m}-m_1)}{2{u_1}^2}+\frac{2(\hat{m}-m_2)}{2{u_2}^2}=0, \tag{4.13}$$

The best estimated value $\hat{m}$ can be determined by:

$$\hat{m} = \left(\frac{m_1}{u_1^2} + \frac{m_2}{u_2^2}\right) \Big/ \left(\frac{1}{u_1^2} + \frac{1}{u_2^2}\right) \tag{4.14}$$

Define weights

$$w_1 = \frac{1}{u_1^2} \text{ and } w_2 = \frac{1}{u_2^2} \tag{4.15}$$

Equation (4.14) can be rewritten as:

$$\hat{m} = \frac{w_1 m_1 + w_2 m_2}{w_1 + w_2} \tag{4.16}$$

Using the uncertainty propagation principle (JCGM, 2008a), the uncertainty for $\hat{m}$ can be determined as:

$$\begin{aligned} \hat{u} &= \sqrt{\left(\frac{w_1}{w_1 + w_2} u_1\right)^2 + \left(\frac{w_2}{w_1 + w_2} u_2\right)^2} \\ &= \sqrt{\left(\frac{\frac{1}{u_1}}{\frac{1}{u_1^2} + \frac{1}{u_2^2}}\right)^2 + \left(\frac{\frac{1}{u_2}}{\frac{1}{u_1^2} + \frac{1}{u_2^2}}\right)^2} = \frac{1}{\sqrt{\left(\frac{1}{u_1^2} + \frac{1}{u_2^2}\right)}} \end{aligned} \tag{4.17}$$

Using the weight denotation yields the uncertainty value $\hat{u}$:

$$\hat{u} = \frac{1}{\sqrt{w_1 + w_2}} \tag{4.18}$$

Equation (4.18) shows that the fused uncertainty has a smaller value than that from each of the original measurement data.

4.2.3 Data modelling and data fusion principle from the view of dimensional measurement science

From a statistical point of view, a measurement dataset which has a smaller measurement uncertainty has a larger weighting to the fused measurement value and

vice versa. It is intuitively understood that there is a bias towards measurement data which are more accurate. Equation (4.18) also shows that the fused uncertainty is smaller than any other uncertainty from the original measurement data. The fusion of two Gaussian distributions is illustrated in Figure 4.2. The horizontal axis denotes the measurement value at a specific position and the vertical axis denotes the probability of obtaining that measurement value. The two measurement datasets are of Gaussian distribution and denoted as Data 1 and Data 2 as shown in Figure 4.2. Regarding the random error, Data 2 is more accurate than Data 1 since Data 2 has a smaller standard deviation. The fused data have an even smaller standard deviation which illustrates that they have improved accuracy.

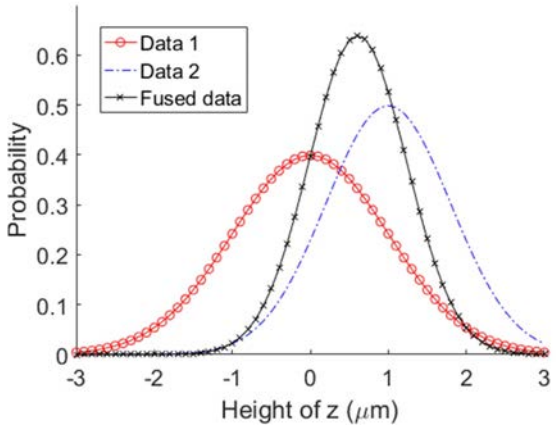

Figure 4.2 Fusion of two Gaussian distributions

Due to the nature of dimensional measurement, every measurement result has associated uncertainty and the true value is never known. Moreover, there are systematic error and random error contained in the measurement result. The systematic error denotes the bias from the estimated mean value to the true value while the random error complies with the Gaussian distribution of the measurement result which represents the measurement uncertainty. In the process of maximum likelihood-based multi-sensor data fusion, the fusion algorithm takes into account both the systematic error and random error and the fused result is calculated in a statistical manner. It is

easy to understand that the output uncertainty is reduced in the fusion result since the fusion process itself can be considered as a multiple (double) measurement process which can reduce the measurement uncertainty as compared to single measurement in the final result (Taylor, 1997). It is interesting to note that the weights for each dataset are determined by the associated uncertainties, i.e. the random errors. If a measurement has large systematic error but small random error while another measurement has small systematic error but large random error, the fused result will have a large bias to the measurement with small random error, which will introduce a large systematic error in the fused result.

This issue also exists in other fusion methods such as weighted least square fusion (Wang et al., 2015). This is particularly true for the state-of-the-art technology where the measurement instruments have high repeatability with very low measurement noise. However, the systematic error is sometimes large as compared to the random error, which means that the repeatability is high but the accuracy is not ensured (i.e. may deviate from the true value) (Liu et al., 2015). On the other hand, with the advanced technology such as the precision calibration method, the systematic error of CMMs is controlled well which can reduce the influence of this effect. The influence of the systematic error and random error on the fused result under different situations is shown in Figure 4.3.

With two different measurement datasets *D1* and *D2*, it is assumed that *D2* has smaller uncertainty than *D1*, the fused result *Df* has smaller uncertainty than both *D1* and *D2* and the mean of *Df* has a bias towards *D2*, which is shown in all the sub-figures in Figure 4.3. It is interesting to note that the true value (short as *Tv*) of the measurement is unknown and it can be considered under the following four situations: (a) $Tv < M1 < M2$, (b) $M1 < Tv < M2$ (bias to *M1*), (c) $Tv < M1 < M2$ (bias to *M2*) and (d) $M1 < M2 < Tv$, where *M1* and *M2* are the mean values of *D1* and *D2*.

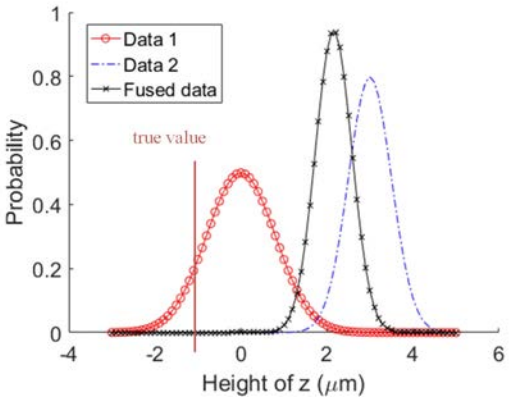

(a) Measurement with large systematic error but small random error, fused with measurement with small systematic error but large random error, $Tv < M1 < M2$

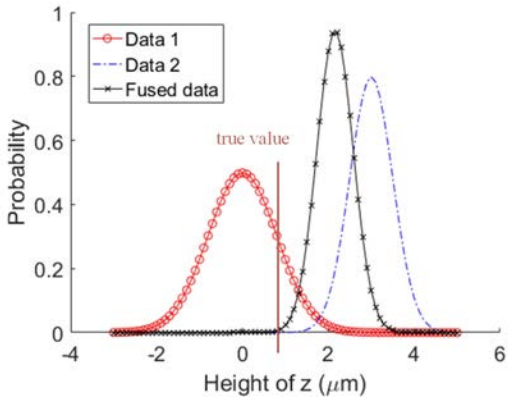

(b) Measurement with large systematic error but small random error, fused with measurement with small systematic error and large random error, $M1 < Tv < M2$

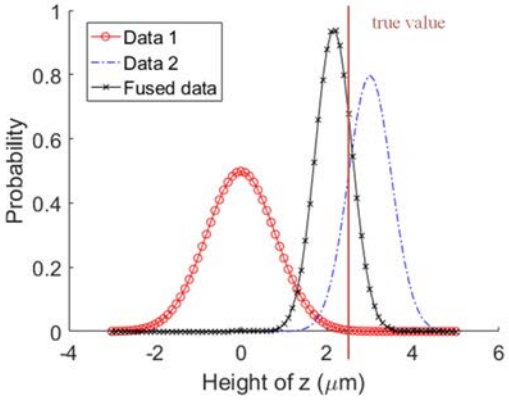

(c) Measurement with small systematic error and small random error, fused with measurement with large systematic error and large random error, $Tv < M1 < M2$

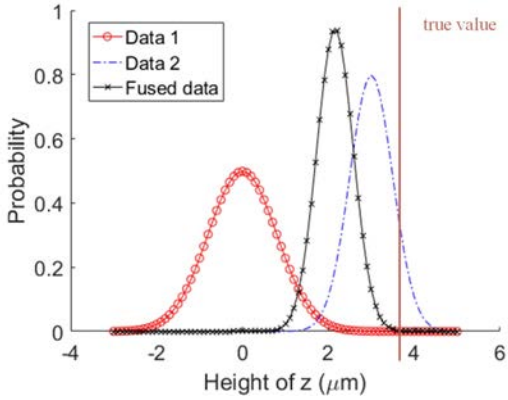

(d) Measurement with small systematic error and small random error, fused with measurement with large systematic error and large random error, $M1 < M2 < Tv$

Figure 4.3 Influence of systematic error, random error and the true value for the fused result

The case as shown in Figure 4.3(c) is the ideal case which has the optimal result that the fused result has the smallest bias to the true value. The case as shown in Figure 4.3(a) is the worst case in which the fused result has the largest bias to the true value.

In practice, the sensor with small measurement uncertainty usually possesses a small systematic error. This is particularly true when comparing the optical sensor with contact sensor which are widely used in multi-sensor CMMs, e.g. the laser sensor has large uncertainty and large systematic error while the touch trigger probe has small uncertainty and small systematic error. The case shown in Figure 4.3(d) is another case in which the fused result has a smaller uncertainty: it has a smaller bias than *D1* but larger than *D2*. This is the case that should be paid much attention in multi-sensor data fusion for dimensional measurement. In general, with a sophisticated designed multi-sensor CMM, the case shown in Figure 4.3(c) is the most desired case statistically, since the true value should be among the two mean values of the different measurements with bias to the sensor with a higher accuracy in a well-calibrated situation. In fact, this situation has the highest probability in the measurement process.

In this study, the mean value and associated uncertainty for the measurement datasets are not directly given by the measurement instrument but they are modelled by using the Gaussian process modelling method. Due to the existence of measurement uncertainty, the data points in the measurement result cannot represent the mean surface but are Gaussian distributed along the mean surface. The use of Gaussian process data modelling aims to model the raw data to obtain the mean surface and the associated uncertainty at every position of interest. The mean surface can be treated as the best estimated true value for the surface. With a sophisticated designed multi-sensor CMM and a well-established Gaussian process model, the mean surfaces from two different sensors should be consistent with each other with small systematic error. However, in some cases in which the accuracy requirement is stringent, the

measurement error from the hardware and the modelling error from the Gaussian process method may influence the final result, especially when one of the sensors has a large systematic error.

4.3 Experiments and discussions

To demonstrate the effectiveness and limitation of the proposed method, a series of simulated and real measurements with a sinusoidal surface and an f-theta lens surface was carried out. The performance of Gaussian process modelling was also demonstrated in a series of evaluation experiments. The real measurement experiments were conducted on a Werth VideoCheck UA multi-sensor CMM as shown in Figure 4.4 and the results are analyzed and discussed. The designed and machined sinusoidal and f-theta lens freeform surface are shown in Figure 4.5. Two sensors were used in

Figure 4.4 Werth VideoCheck UA multi-sensor CMM used for the experiments

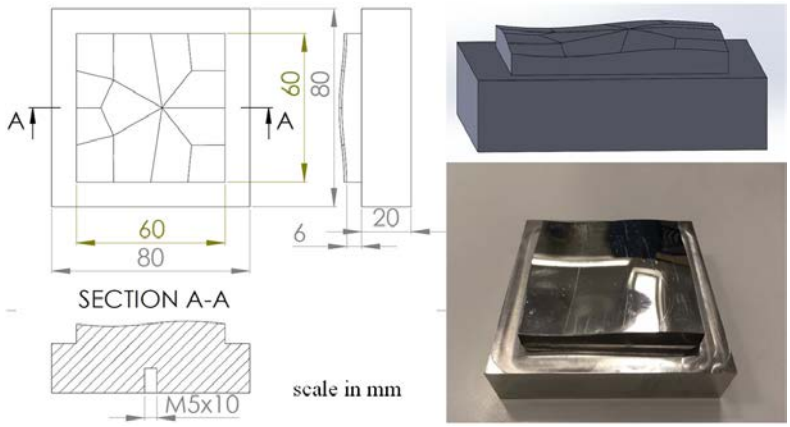

(a) Sinusoidal workpiece

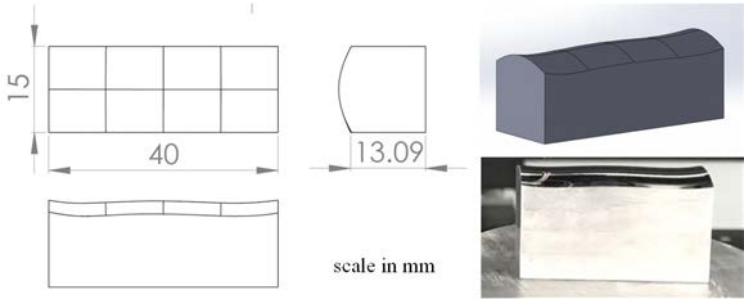

(b) F-theta lens workpiece

Figure 4.5 The designed and machined workpieces

the measurement experiment: the Werth opto-electronic non-contact laser distance sensor and the trigger probe (Renishaw TP200) with a 1.997-mm diameter tip. The probing error of the trigger probe is ±0.65 μm while the probing error of the laser sensor is ±1.0 μm. The Maximum Permissible Measuring Error (MPE) of the CMM is (0.75+L/300) μm. The experiment was conducted in a clean room and the environment temperature was kept at 20±1°C.

4.3.1 Simulated experiments

4.3.1.1 Sinusoidal surface

The first experiment simulated the measurement of a sinusoidal surface with two different sensors. For each sensor, the measurement had different uncertainty

values. Figure 4.6 shows the simulated measurement results and the measurement can be determined as:

$$z_{1,2} = a\left[\sin\left(\frac{\pi}{10}x\right) + \cos\left(\frac{\pi}{10}y\right)\right] + \varepsilon_{1,2}, \tag{4.19}$$

where $a = 1$ mm, $x \in [0,40]$ mm and $y \in [0,40]$ mm, $\varepsilon_1 = 0.03$ mm and $\varepsilon_2 = 0.02$ mm are the added normal distributed noises which represent different measurement uncertainties.

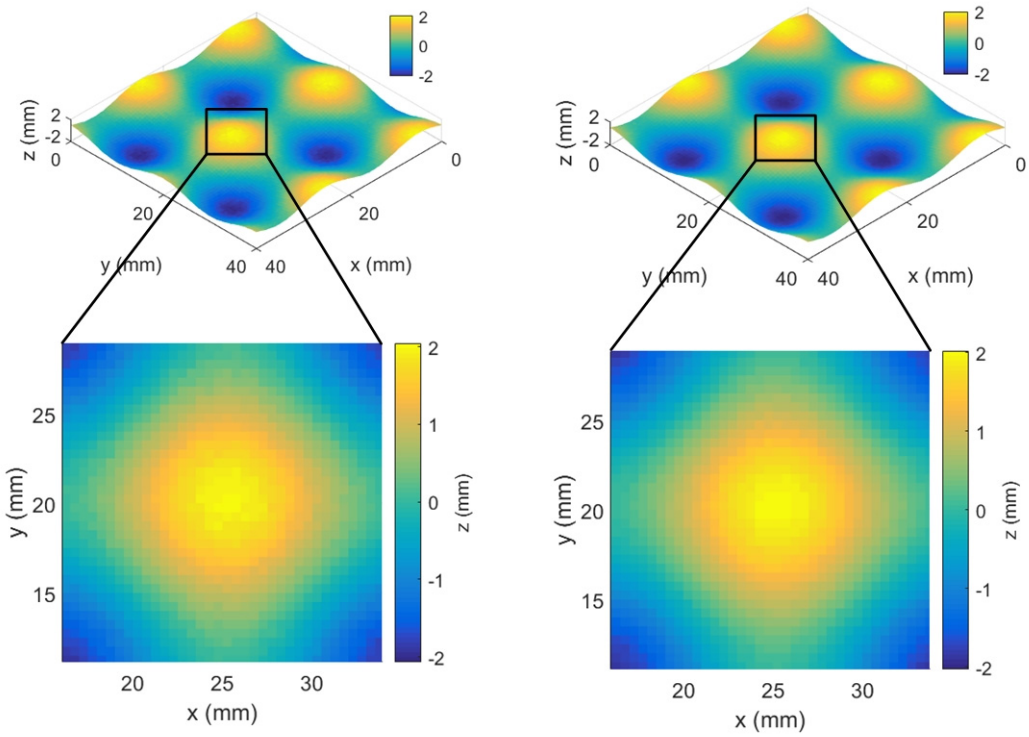

(a) With 30 μm measurement noise *(b) With 20 μm measurement noise*

Figure 4.6 Simulated measurement results of the designed sinusoidal surface

Modelling of the two measured datasets was undertaken by the Gaussian process method. In the Gaussian process modelling, the mean function was initially chosen to be zero mean function and the covariance function was Squared Exponential function, while the likelihood function was specified to be Gaussian. The parameters of the covariance function corresponding to unit characteristic length-scale and unit

signal standard deviation were firstly initiated to be zeros and the likelihood parameter was initiated to be $\log(0.1)$, which denotes the standard deviation of the noise to be 0.1 mm. The parameters of the Gaussian process were then optimized by minimizing the negative log marginal likelihood. The results of the Gaussian process modelling are shown in Figure 4.7. The covariance is shown in a profile view for better illustration. The root mean squared (RMS) values of the covariance surfaces were 29.8 μm and 19.8 μm, and the modelling errors were both 0.2 μm, which clearly demonstrate the effectiveness of modelling the noise for the two measurement datasets.

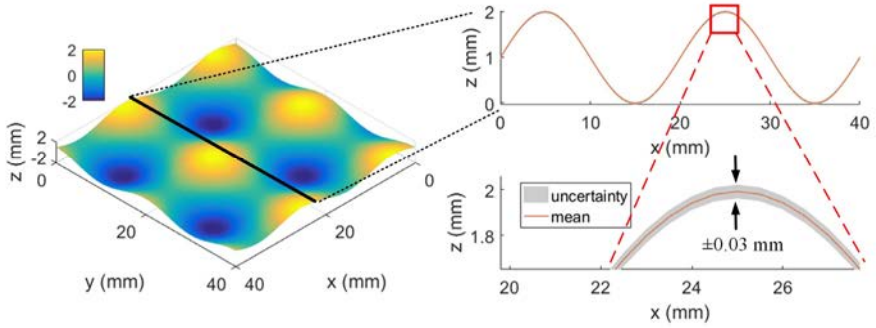

(a) With 30 μm measurement noise

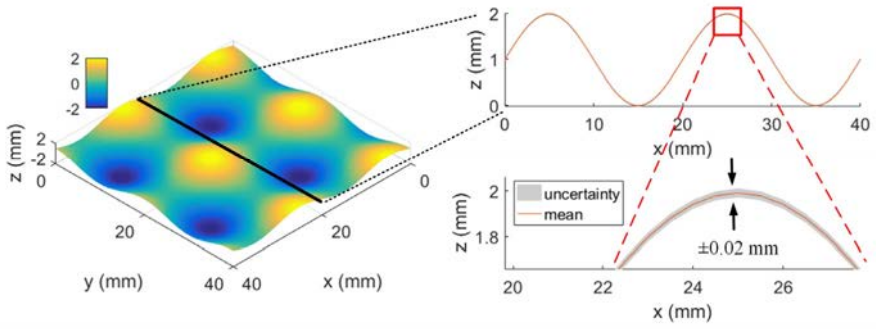

(b) With 20 μm measurement noise

Figure 4.7 Gaussian process modelling results of the two simulated measured datasets

The fused result with the maximum likelihood data fusion algorithm is shown in Figure 4.8. The result shows that the overall uncertainty value was reduced and the

RMS value of the covariance surface was 16.5 mm, smaller than both the original measurement data.

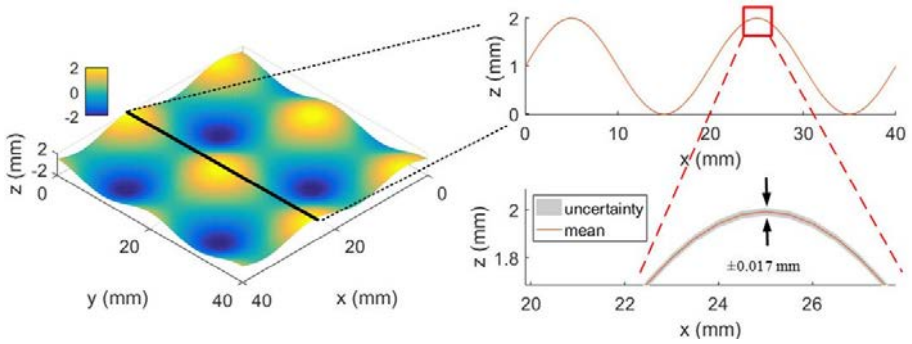

Figure 4.8 Fused result with the maximum likelihood data fusion method.

The deviations from the original measured surfaces and fused surface to the underlying surface were evaluated and the result is shown in Figure 4.9. It is interesting

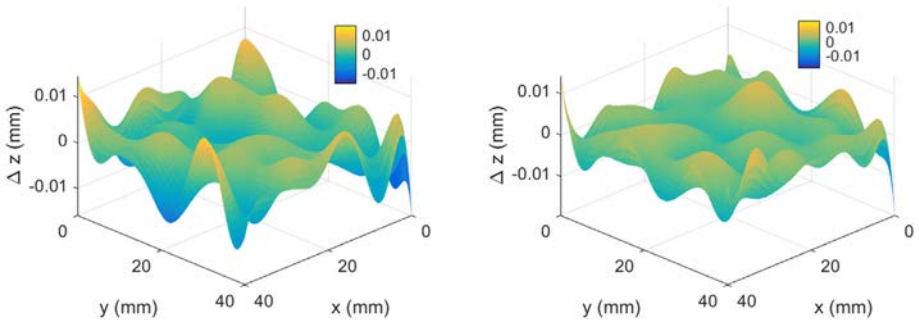

(a) For sensor 1 *(b) For sensor 2*

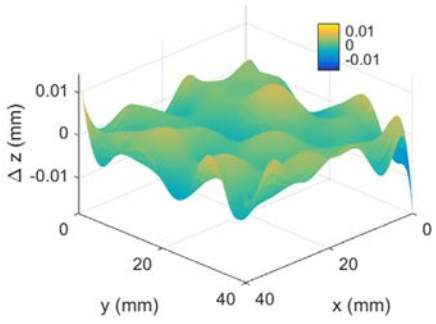

(c) For fused data

Figure 4.9 Deviations to underlying surface

to note that the edge area of the measurement results, especially the corner area, had a larger prediction error since there were insufficient measurement data in those areas. Table 4.1 shows the RMS value of the uncertainties and the deviations for the original measurement datasets and the fused dataset. The result clearly shows that both the uncertainty and the deviation from the reference surface had improvements as compared to the original measurement results.

Table 4.1 RMS value of associated uncertainties of original measurement datasets and fused dataset

	With sensor 1	With sensor 2	Fused data
RMS of uncertainty	29.8 μm	19.8 μm	16.5 μm
RMS of deviation	3.5 μm	2.4 μm	2.2 μm

4.3.1.2 F-theta lens surface

Another simulation experiment was conducted on an f-theta lens freeform surface to evaluate the proposed method. Compared with the sinusoidal surface, the f-theta lens surface is relatively smoother without periodical features. The measurement of the f-theta lens surface is determined by:

$$z_{1,2} = ax^2 + bx^4 + cy^2 + \varepsilon_{1,2}, \tag{4.20}$$

where $a = -1/250$, $b = 1/92000$ and $c = -1/25$ are the design parameters of the surface and $\varepsilon_1 = 40$ μm and $\varepsilon_2 = 30$ μm are the added normal distributed noises which represent the different measurement errors. Figure 4.10 shows the simulated measurement surfaces.

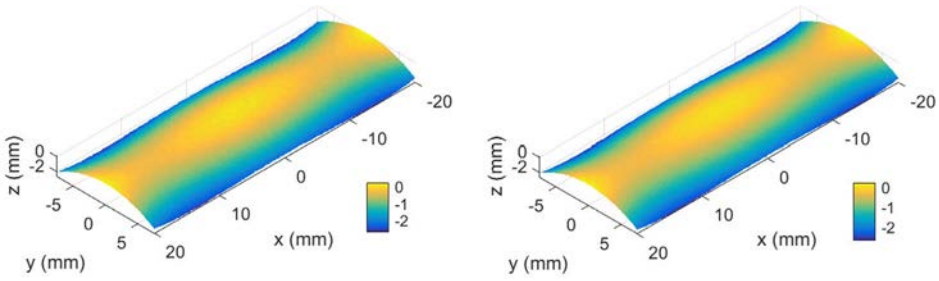

(a) With 40 µm measurement noise *(b) With 30 µm measurement noise*

Figure 4.10 Simulated measurement results of the designed f-theta lens surface

Figure 4.11 shows the results of Gaussian process modelling with the mean surface and the covariance surface determined. The RMS values of the covariance

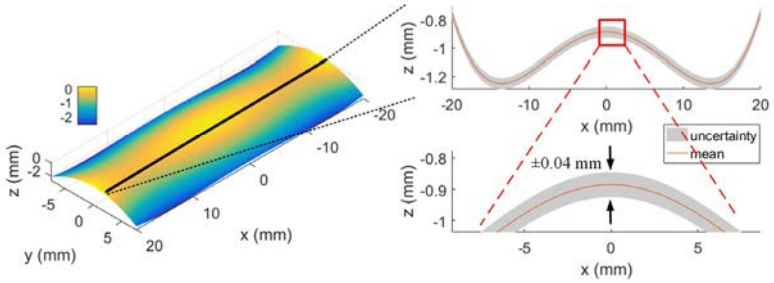

(a) With 40 µm measurement noise

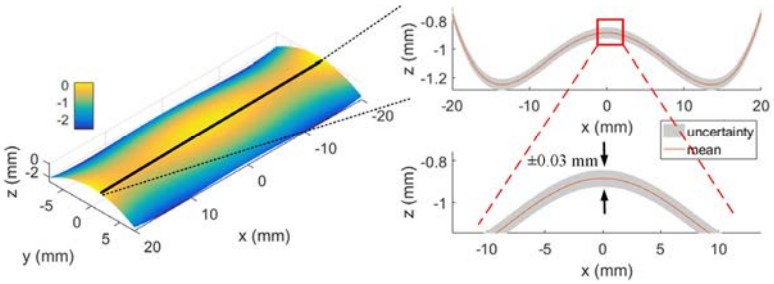

(b) With 30 µm measurement noise

Figure 4.11 Gaussian process modelling results of the two simulated measured datasets

surface were 38.6 µm and 31.0 µm and the modelling errors were 1.4 µm and 1.0 µm, respectively. The results show that the measurement uncertainty was estimated well

using the Gaussian process. Figure 4.12 shows the result after maximum likelihood data fusion. The RMS value of covariance surface was 24.2 μm which is smaller than the ones from the original covariance surface, and this is expected from the use of the data fusion principle.

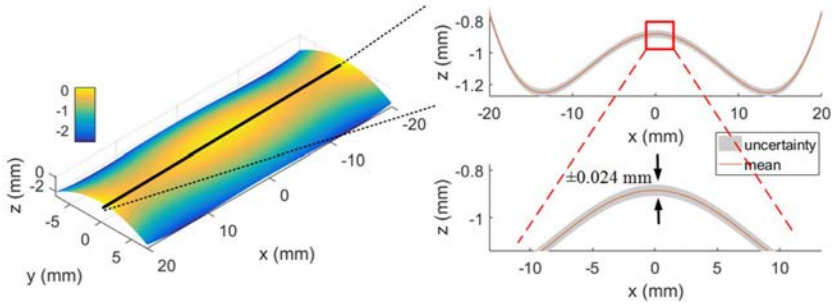

Figure 4.12 Fused result with the maximum likelihood data fusion method

The deviations from the original surfaces and the surface after data fusion to the underlying surface are shown in Figure 4.13. The RMS value of the uncertainties

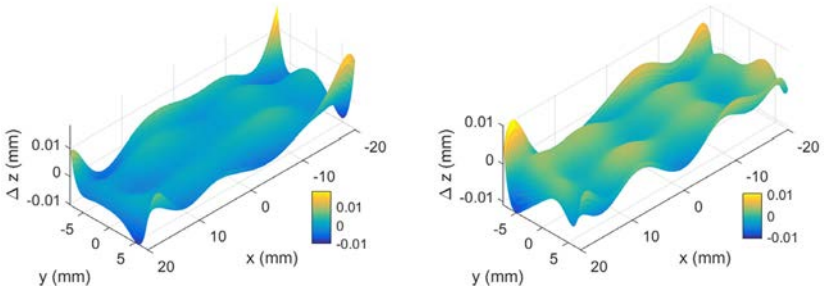

(a) For sensor 1 *(b) For sensor 2*

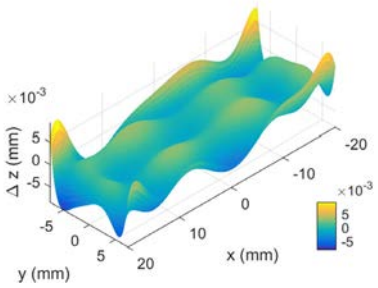

(c) For fused data

Figure 4.13 Deviation from the underlying surface

and deviations are shown in Table 4.2. Both the uncertainties and the deviations of the fusion result showed improvement as compared with the original datasets. Similar to the one for the sinusoidal surface, the error in the edge and corner area was larger since the data in those areas were insufficient.

Table 4.2 RMS value of associated uncertainties of original measurement datasets and fused dataset

	With sensor 1	With sensor 2	Fused data
RMS of uncertainty	38.6 μm	31.0 μm	24.2 μm
RMS of deviation	2.3 μm	2.1 μm	1.8 μm

4.3.2 Model error analysis for Gaussian process modelling

In the previous simulation experiments, the measurement noises were modelled well by the Gaussian process modelling method. However, in real-life situations, machined surfaces are not perfect and may contain defects and form error due to machining error which may affect the modelling accuracy of the Gaussian process. A series of simulation experiments was conducted to verify the effectiveness and limitations of Gaussian process modelling by adding the form error to the simulated surface. That is to say, the simulated surface had a base form, form error and measurement noises as shown in Figure 4.14. The base form was a sinusoidal surface with lateral pitch of 50 mm and the peak-to-valley (PV) value was 4 mm with the surface denoted by S_b. The machining error denoted by S_e was simulated to be a sinusoidal deviation from the base form with a higher spatial frequency together with a pitch of 5 mm and smaller peak-to-valley height (PV) value of 0.1 mm, and the PV value was varied in a series of experiments in order to validate the model. The

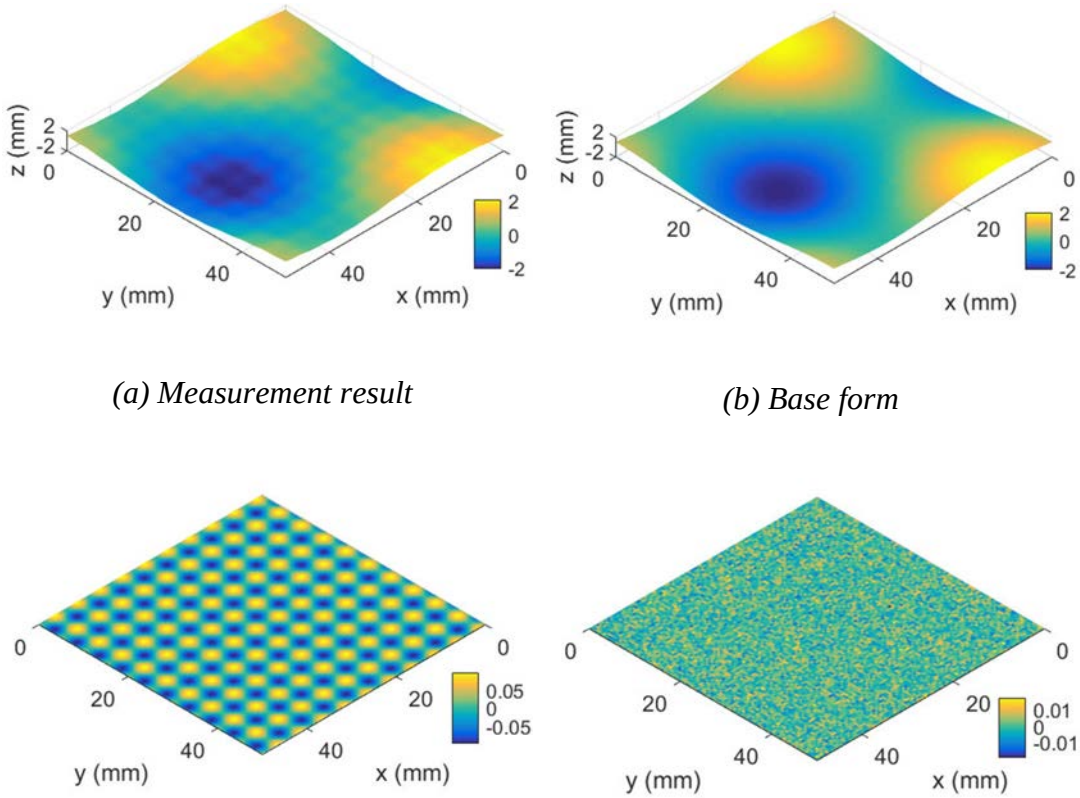

(a) Measurement result

(b) Base form

(c) Machining error

(d) Measurement noise

Figure 4.14 Simulated measurement result and components with different spatial frequencies

combination of the base form and the form error determined the actual form (S_c) of the surface as shown in Equation (4.21):

$$S_c = S_b + S_e, \tag{4.21}$$

For the measurement noise N, it was simulated to be Gaussian distributed noise with zero mean and 0.005 mm standard deviation, the expanded deviation was of 0.015 mm (k=3), and this amplitude was also varied to test the performance of the model. The simulated measurement result of the surface is denoted by S_m:

$$S_m = S_b + S_e + N, \tag{4.22}$$

The experiment was conducted as follows. The amplitude of the base form was fixed as ±2 mm and the standard deviation of the measurement noise was fixed as 0.005 mm. The expanded deviation of the measurement noise level (k=3) was 0.015 mm. The amplitudes of the form errors in the experiments were simulated as ±0.005 mm, ±0.01 mm, ±0.02 mm, ±0.03 mm, ±0.04 mm and ±0.05 mm. The simulated measurement result of the surface S_m was then modelled by using the Gaussian process modelling method and the mean surface S_{mean} and the variance surface S_{cor} were calculated. The objective function O_E of the performance of the Gaussian process model was determined by the RMS of the deviation from the mean surface S_{mean} to S_c:

$$O_E = RMS(S_{mean} - S_c), \tag{4.23}$$

The result of the experiment is shown in Figure 4.15(a). The result shows that when the form error was smaller than the measurement noise, the error of the model was large, while when the form error was larger than the measurement noise, the error of the model was small. This result demonstrates that when the form error is smaller than or similar to the measurement noise, the model has the limitation of being unable

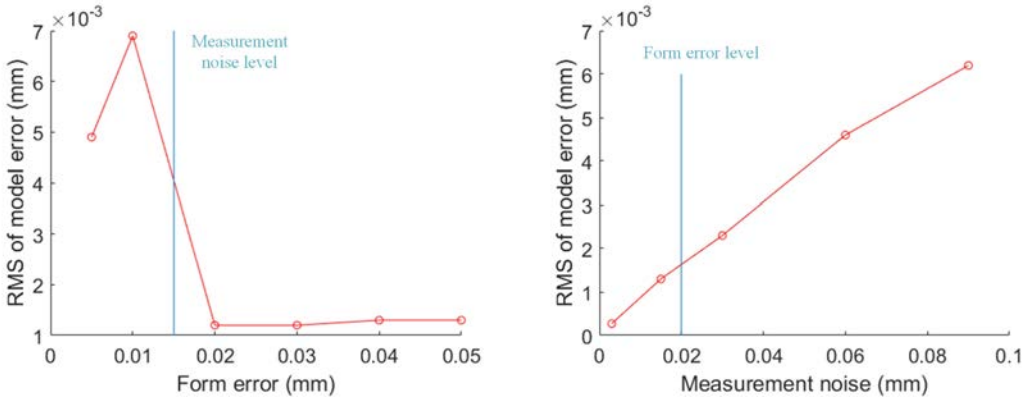

(a) Fixed measurement noise *(b) Fixed form error*

Figure 4.15 The relationship of model error, form error and measurement noise

to distinguish the form error and measurement noise which leads to a large modelling error that treats both the form error and the measurement noise as the measurement noise. This leads to an overestimate of the overall uncertainty of the measurement.

Another experiment was conducted to fix the base form and the form error, and change the amplitude of the measurement noise. The amplitude of the base form was also fixed as ±2 mm as in the previous experiment while the form error was fixed as ±0.02 mm. The standard deviation of the measurement noise was simulated as 0.001 mm, 0.005 mm, 0.01 mm, 0.02 mm and 0.03 mm. The method of evaluation of the performance of the model was similar to that in previous experiments and the result is shown in Figure 4.15(b). The expanded deviation values of the measurement noise are used in the results. The result shows that the model error increases when the measurement noise increases in a linear relationship. When the measurement noise is larger than the form error, the modelled error may also be affected by the form error but this is not clearly shown in the result since it may be covered by the effect of the large measurement noise.

In general, the experiment results show that the accuracy of the model of Gaussian process modelling is not only affected by the measurement noise but also by the form error of the measured surface, especially when the amplitude of the form error is smaller than that of the measurement noise. It is interesting to note that the model error affected by the measurement noise is in the confident region of the uncertainty modelled by the Gaussian process which is acceptable in the result, and the model error being affected by the form error is not the case since it may cause the mean surface to have a bias to the true value which is outside the confident region of the modelling. This is one of the limitations of Gaussian process data modelling and affects the accuracy of the proposed method.

4.3.3 Evaluation of the performance of measurement uncertainty modelling using the Gaussian process

To evaluate the performance of the Gaussian process model for modelling the measurement uncertainty for a multi-sensor CMM, a repeated measurement experiment by using the touch trigger probe was conducted and compared with the specification of the sensor and the result of using Gaussian process modelling. A workpiece was designed as shown in Figure 4.16 and eight points (marked A-H) were measured 50 times with a purposely-designed DMIS programming language (Werth Messtechnik GmbH, 2011). The eight points were chosen to be on the flat surface and curved surface with different tilting angles. The results show good agreement with similar distribution and Figure 4.17 shows one of the measurement results in a histogram and fitted Gaussian distribution. The standard deviation of the fitted Gaussian distribution is about 0.7 μm which is at the same level of the specification of the touch trigger probe (i.e. 0.65 μm).

The freeform surface as shown in Figure 4.5(a) was measured by using the touch trigger probe with a dense measurement (i.e. 0.5 mm pitch). The measured data

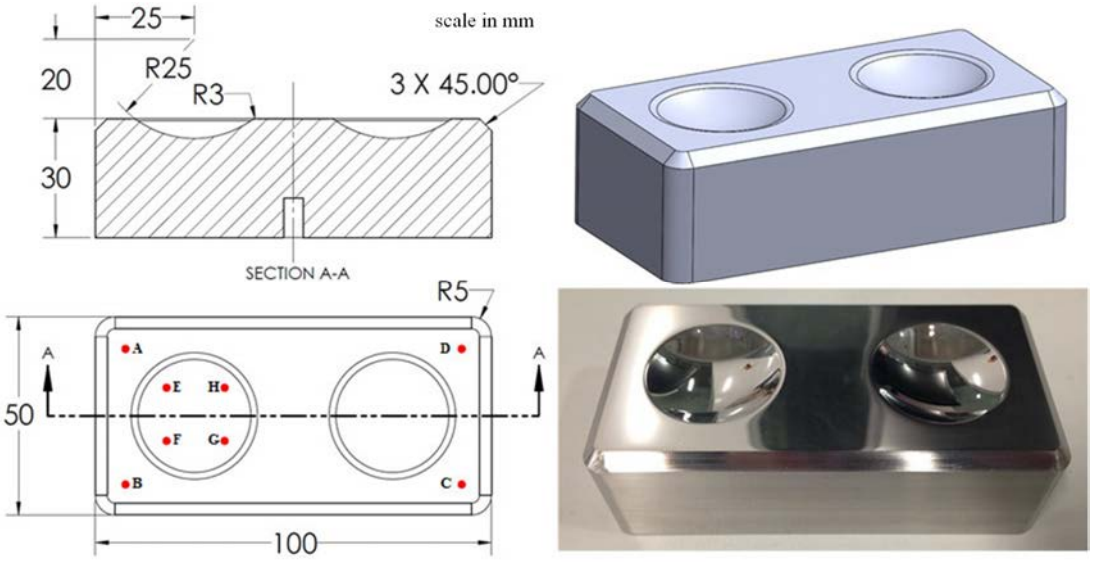

Figure 4.16 The designed and machined workpiece and the repeated measurement

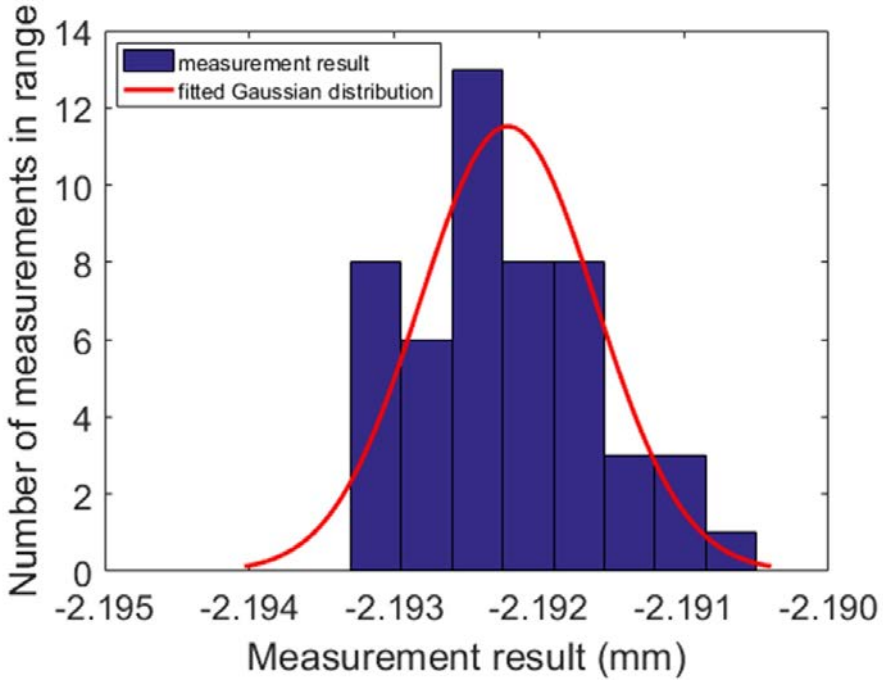

Figure 4.17 Evaluation result for the measurement uncertainty for the trigger probe using the repeated measurement method

were modelled by Gaussian process modelling while the mean surface and the associated uncertainty are shown in Figure 4.18. The RMS of the uncertainty is 0.74 μm which is slightly larger than the specification of the probe and the experimental standard deviation value. The result demonstrates the effectiveness of the Gaussian

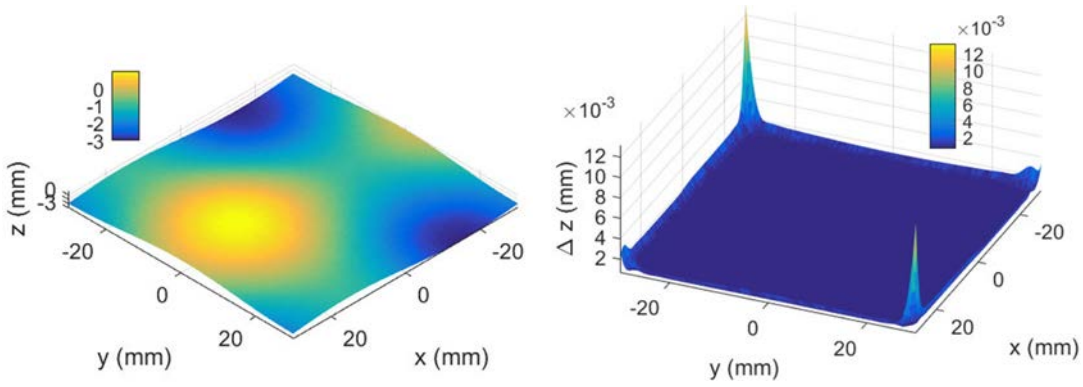

(a) Mean surface *(b) Associated uncertainty*

Figure 4.18 Mean surface and associated uncertainty after Gaussian process modelling

process method to model the measurement uncertainty. It should be noted that the uncertainties in the edge and corner areas are largely due to the lack of data points in those areas and the measurement uncertainties are different with different measurement density, with less measurement points or larger sampling pitch, so it is clear that the measurement uncertainty is larger due to a reduction of measurement data.

4.3.4 Measurement experiment using a multi-sensor CMM

The two workpieces with sinusoidal and f-theta lens surface surfaces as shown in Figure 4.5 were measured with the Werth multi-sensor CMM with a laser sensor and touch trigger probe to demonstrate the effectiveness of the proposed data modelling and data fusion method. Generally, the laser sensor has the strength of its non-contact measurement nature but has larger measurement uncertainty while the touch trigger probe has higher measurement accuracy with smaller uncertainty. The measurement with the laser sensor was designed to be dense and the measurement with the touch trigger probe was designed to have less sampling points.

4.3.4.1 Measurement of a sinusoidal surface

The experiment was designed as follows. First, the sinusodial surface was measured by the touch trigger probe with a density of 0.5 mm and the measurement result was treated as the reference data since it had high density and high accuracy. The surface was then measured by the laser sensor with a density of 1 mm pitch and this measurement result was determined as the first dataset. The measured data were then modelled by the Gaussian process and the results are shown in Figure 4.19. Figure 4.19(a) is the raw data from the laser sensor, Figure 4.19(b) and Figure 4.19(c) are the mean surface and the associated uncertainty of the Gaussian process while Figure 4.19(d) shows the deviation from the mean surface to the reference surface. The RMS of the uncertainty is 18.3 μm and the RMS of the deviation is 38.3 μm. The large

measurement uncertainty may be caused by the unstable measurement of the optical sensor. It is interesting to note that the prediction grid for the Gaussian process has 1-mm pitch in the area where $x \in [-30, 30]$ mm and $y \in [-30, 30]$ mm.

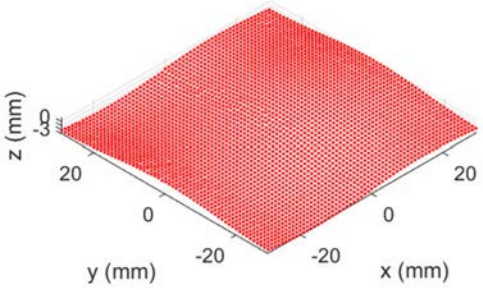

(a) Raw data of measurement with the laser sensor

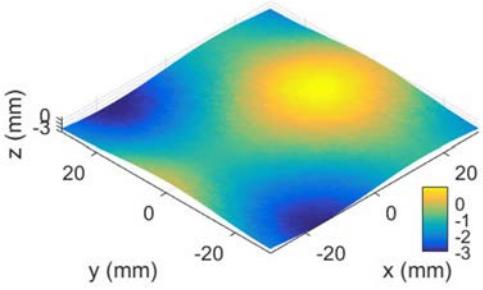

(b) Mean surface

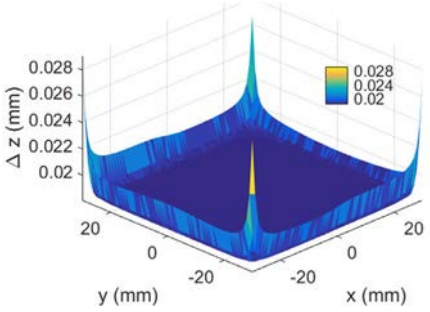

(c) Associated uncertainty

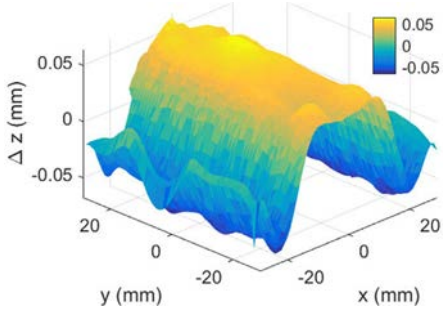

(d) Deviation of the mean surface to the reference data

Figure 4.19 Measurement data of laser sensor and Gaussian process result

A subset of 50 randomly sampled measurement points from the dense measurement data of the touch trigger probe was selected as the second dataset. The raw data and the result after the Gaussian process for the second dataset are shown in Figure 4.20. Figure 4.20(a) shows the raw measurement data while Figure 4.20(b) shows the mean surface and Figure 4.20(c) shows the associated uncertainty. Figure 4.20(d) shows the deviation from the mean surface to the reference surface. It is noted that the grid of the prediction for the Gaussian process is the same as that for the laser

sensor. The RMS of the measurement uncertainty is 15.7 μm and the RMS of the deviation map is 13.2 μm. The large measurement uncertainty is due to the small number of sampling points.

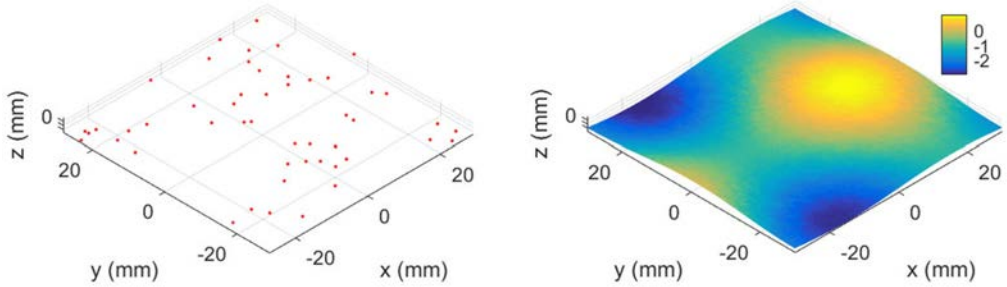

(a) Raw data of the touch trigger probe *(b) Mean surface*

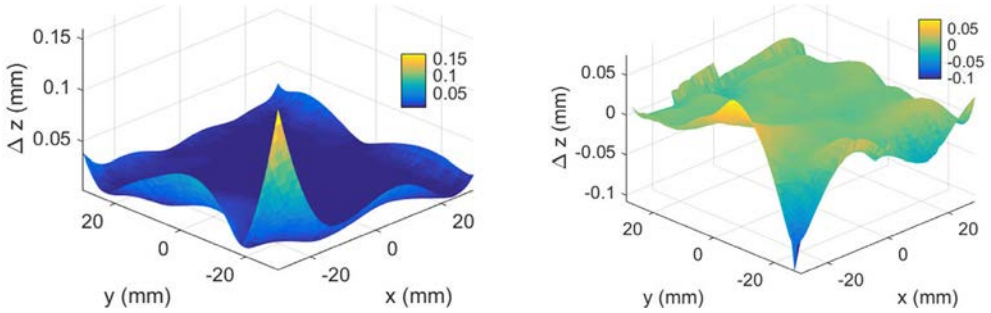

(c) Associated uncertainty *(d) Deviation to the reference data*

Figure 4.20 Measurement data of touch trigger probe and Gaussian process result

The fused result of the dataset from the laser sensor and trigger probe is shown in Figure 4.21. Figure 4.21(a) is the fused mean surface, while Figure 4.21(b) is the associated uncertainty and Figure 4.21(c) is the deviation from the fused mean surface to the reference data. The RMS of the uncertainty is 8.0 μm and the RMS of the deviation map is 8.4 μm, both showing improvements compared to the original measurement datasets.

Five different datasets for the touch trigger probe from different sampling positions were obtained and underwent the above procedure and the results are shown in Figure 4.22. The measurement data of the laser sensor were the same. Figure 4.22(a)

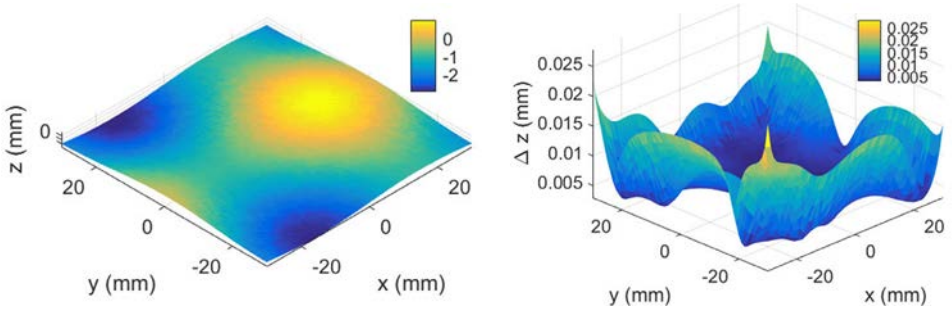

(a) Mean surface *(b) Associated uncertainty*

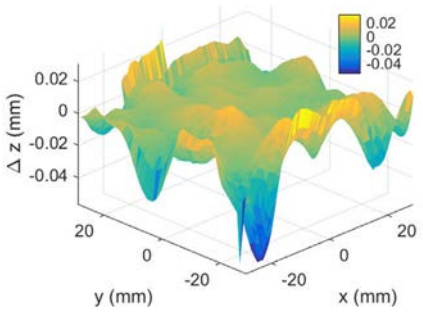

(c) Deviation from reference data

Figure 4.21 Mean surface, associated uncertainty and deviation from the reference data after data fusion

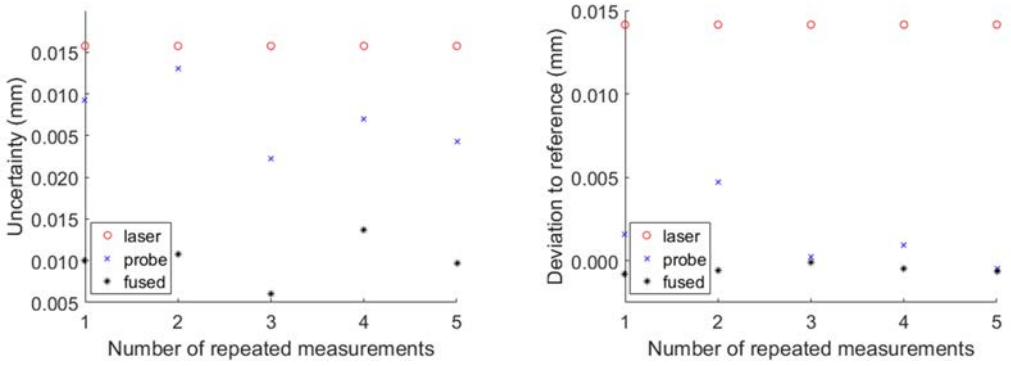

(a) Uncertainty *(b) Deviation from the reference surface*

Figure 4.22 Repeated measurement results

shows the results of the RMS of the measurement uncertainties and Figure 4.22(b) shows the result of the RMS of the deviations. Both results show a consistent

improvement of the measurement uncertainty and deviation from the reference data for the repeated measurement. The result demonstrates the effectiveness of the proposed data modelling and data fusion method. The high repeatability of the improvement of the data fusion may result from the well-established sensor configuration and high performance of data modelling which fit the situation shown in Figure 4.3(c).

4.3.4.2 Measurement of a f-theta lens surface

The f-theta lens freeform surface was measured in the present study. Instead of showing the improvement of the final result, this experimental result shows that when one measurement has a large systematic error, the performance of the final result is affected. Similar to the previous experiment, the surface was measured by a touch trigger probe with a dense measurement of 0.5-mm pitch and the result was determined as the reference data. In this experiment, there existed a large systematic error in the measurement of the laser sensor which may have been caused by the outliers in the measurement result, as shown in Figure 4.23. It is interesting to note that the outliers were removed in the data processing with a statistical analysis method (Rusu and Cousins, 2011). However, there was still residual error in the dataset which may have affected the final result. The outliers may be caused by the characteristics of the measured surface such as reflection and dust which may greatly influence the optical sensor.

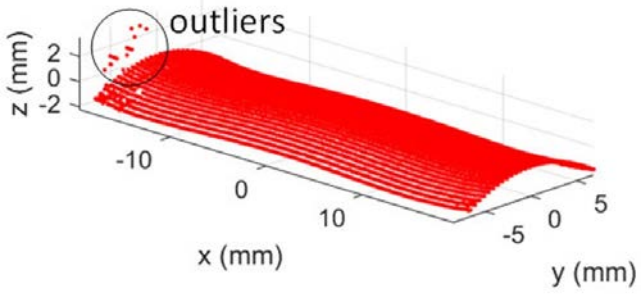

Figure 4.23 Measurement result with outliers of the laser sensor

After the outliers were removed, raw data were processed by Gaussian process modelling and the mean surface was obtained together with the associated uncertainty. The deviation of the mean surface to the reference surface was also determined as shown in Figure 4.24. The RMS of the uncertainty was 18.9 µm and the RMS of the deviation map is 24.9 µm. The result shows a larger uncertainty and even larger deviation than the previous measurement experiment which may introduce a larger systematic error for this measurement.

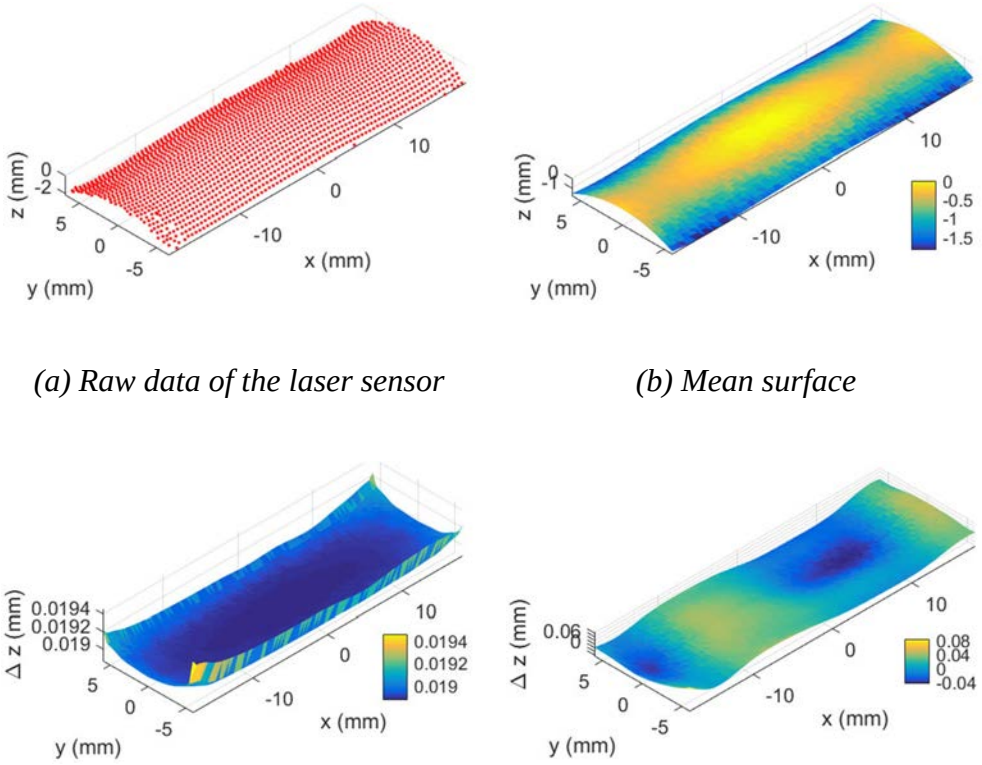

(a) Raw data of the laser sensor *(b) Mean surface*

(c) Associated uncertainty *(d) Deviation to the reference data*

Figure 4.24 Measurement data of laser sensor and Gaussian process result

A subset of 50 points of the measurement data from the touch trigger probe were used as the second dataset for the measurement. The data were modelled using the Gaussian process and the mean surface and the associated uncertainty were determined. The deviation from the mean surface to the reference surface was also

determined as shown in Figure 4.25. The RMS of the uncertainty was 5.7 μm while the RMS of the deviation map is 2.9 μm.

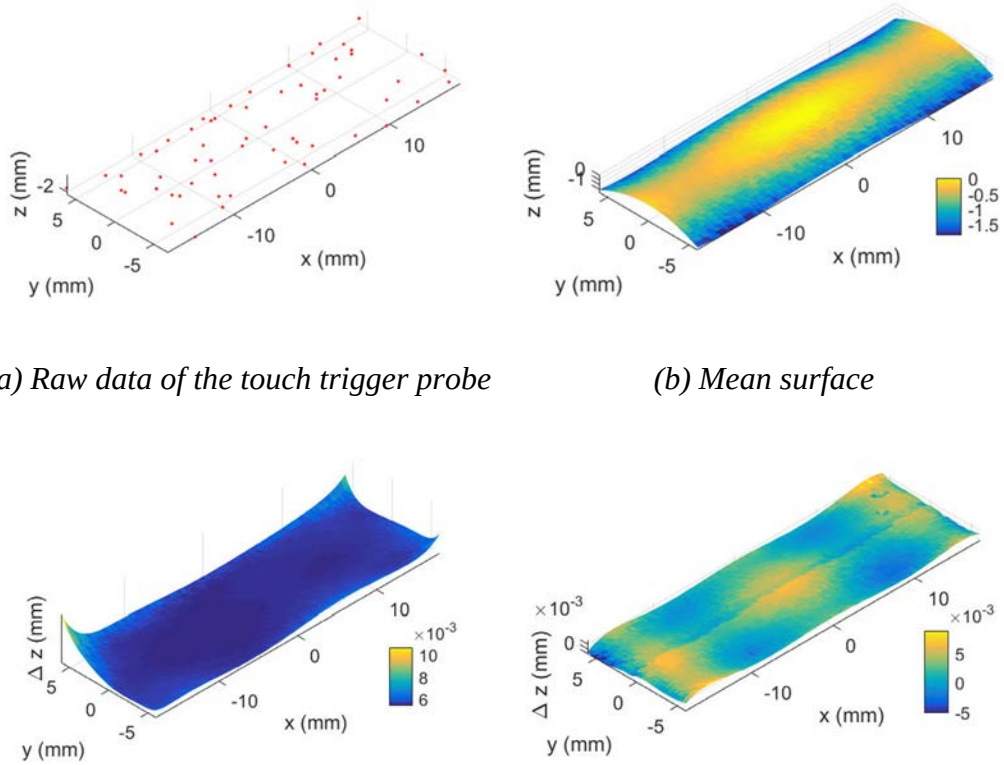

(a) Raw data of the touch trigger probe *(b) Mean surface*

(c) Associated uncertainty *(d) Deviation to the reference data*

Figure 4.25 Measurement data of touch trigger probe and Gaussian process result

The fused results of the two datasets are shown in Figure 4.26. The RMS of fused uncertainty was 5.2 μm while the RMS of the deviation map is 4.8 μm. It is found that the fused uncertainty was improved, which was smaller than the original two datasets. However, the deviation was larger than the one only considering the touch trigger probe. Another five measurement results were obtained at different sampling locations and the results are shown in Figure 4.27. All the results show that the uncertainty was improved while the deviations were worse. This is due to the fact that the measurement data from the laser sensor had large bias from the true value which affected the final fused result. These results of the experiment demonstrate that

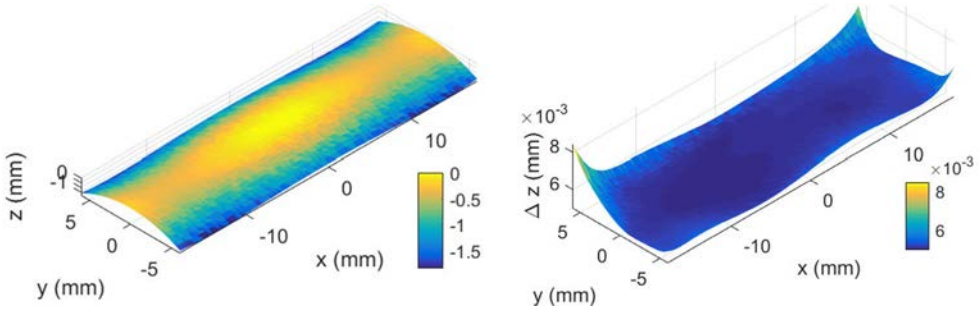

(a) Mean surface *(b) Associated uncertainty*

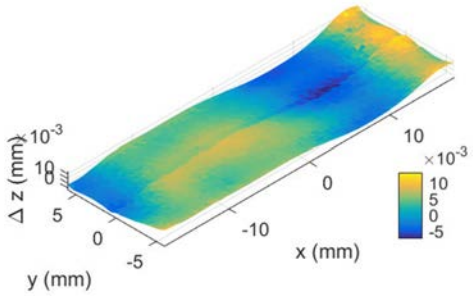

(c) Deviation from reference data

Figure 4.26 Mean surface, associated uncertainty and deviation from reference data after data fusion

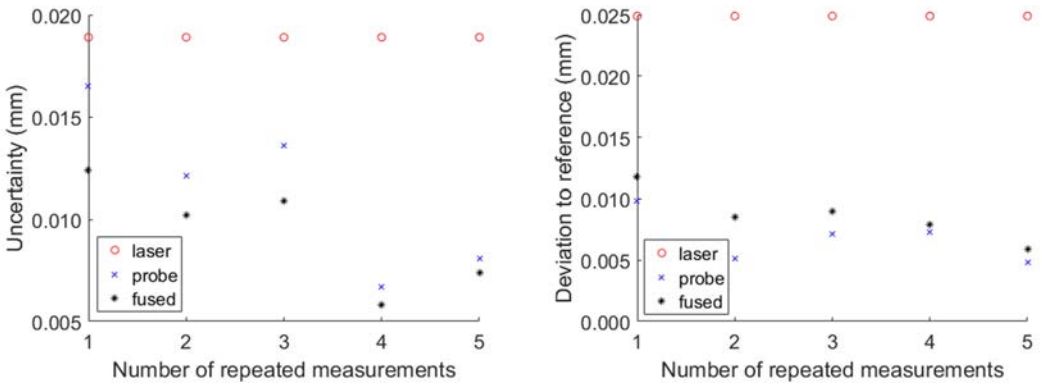

(a) Uncertainty *(b) Deviation from the reference surface*

Figure 4.27 Repeated measurement result

the case was similar to the situation as discussed in Figure 4.3(d), where the true value was larger than the mean values of both original measurements. This is the limitation

of the data fusion method that when one of the sensors has large systematic error, the fused result is poorer than when only considering the data from another sensor. Future work will be focused on the quantitative analysis of the influence of the systematic error on the fusion result. Practically, more attention should be paid to correcting the systematic error, especially that which is caused by the optical sensors such as the laser sensor. For this issue when considering the systematic error, another approach is generating adaptive weighting by a Bayesian framework (Wang et al., 2014). In this situation, the fault-inducing systematic error may be detected and the weighting for those points can be adjusted accordingly.

4.4 Summary

Coordinate measuring machines (CMMs) equipped with multiple sensors are becoming popular in the high-end precision metrology market since their measurement ability can be enhanced by combining the datasets measured from different sensors. The development of a data modelling method for datasets measured by different sensors and an appropriate data fusion method are the key issues for measurement with multi-sensor CMMs so as to further enhance their measurement performance. This chapter presents a data modelling and data fusion method for multi-sensor CMMs which is based on Gaussian process modelling and the Bayesian inference-based maximum likelihood principle. The raw data from different sensors were firstly modelled by the Gaussian process so as to obtain the mean surface and covariance surface which represent the underlying surface and the measurement uncertainty, as well as the prediction for the data at unsampled positions. The mean surface and covariance surface were then fused together by the maximum likelihood principle so as to obtain the best estimated surface and the associated uncertainty. Simulation and real experiments showed that both the measurement uncertainty and prediction error

at unsampled positions underwent improvement over single-sensor measurement. Special attention should be paid to the important aspect of avoiding or reducing the systematic error from each sensor so that the performance of the fusion algorithm can be enhanced. The proposed method is a generic data modelling and data fusion method which can be implemented in various kinds of multi-sensor CMMs with different sensors. The limitation of the proposed method is that the performance is affected by the systemic error. Further work will be suggested to focus on the identification of systematic error and setting different weights according to the accuracy of the datasets regarding the systematic error and random error.

Chapter 5 Development of multi-sensor in-situ metrology systems

5.1 Introduction

The Industry 4.0 standard has proposed a new initiative for in-situ and/or in-process production measurement in manufacturing environments. With the demand for ever higher-performance products, emphasis has been placed on the functional use of three-dimensional (3D) surfaces in order to produce high-value-added products (Jiang and Whitehouse, 2012). The trend towards product miniaturization further constitutes a driving force for the use of 3D surfaces in many fields, such as advanced optics (Fang et al., 2013a) and biomedical applications (Bechert et al., 2000), to improve the performance and provide versatile functionalities of the surfaces. This poses new research challenges for high dynamic range measurement for 3D surfaces that can cover a larger scale with credible accuracy (Leach et al., 2013) and production measurement in manufacturing environments which demand high-speed and robust in-situ and/or in-process surface measurement (Shore and Morantz, 2012, Jiang, 2011, Ju et al., 2014, Zhu et al., 2015). This is particularly true when the workpiece is large and repositioning error is unacceptable.

One of the reasons is that with a large and heavy workpiece, it is difficult, sometimes impossible, to measure the workpiece with an off-line method. Another reason is that it is difficult to compensate for the machining error if the workpiece is taken off for offline-line measurement and remounted on the machine tool after measurement. Moreover, most of the off-line measurement machines rely on one

single sensor with a limited field of view which cannot provide a measurement result with a high dynamic range, which has a large measurement area and high resolution.

To address these challenges, a turnkey solution is to develop a separate metrology loop which does not rely on the structural loop of the machine tool. One of the examples is the Large Optics Diamond Turning Machine (LODTM) (Hale, 1999). This method is similar to most of the modern metrology systems which move the sensor head with the moving linear or rotational stages. To enhance the measurement ability, different types of sensors can be chosen to be mounted on the moving axes. For instance, Lamb et al. (Lamb et al., 1999) developed an automation system for industrial 3D laser digitizing which integrated the Hymarc Hyscan 45C laser scanner with a CMM machine which had a working volume of (2.0×1.3×1.0) m. The Hyscan 45C was built-in with a high-power laser and a panning mirror making it capable of measuring steep walls and deep core out areas which are difficult to measure. Equipped with the products having advanced sensor technologies such as Gocator 3100 series which act as an area structured light sensor, the 3D surface data can be obtained in a single shot measurement with fast measurement speed and high accuracy (LMI Technologies, 2016).

However, integrating these sensors with a separate metrology frame is a complicated and expensive solution. Considering that the machine tools nowadays have precision advanced motion control, the motion accuracy is high and the motion error is within an acceptable accuracy range. Moreover, without machining force, the deformation and vibration situation is better compared with that in the machining process (Hocken and Pereira, 2016). Installing a measurement system on the machine tool is one of the promising methods to implement in-situ measurement. With the large

moving range of the motion axis of the machine tools, high dynamic range measurement can be achieved.

Nowadays, there are commercial machine tools which provide in-situ metrology capability. The MIKRON HPM 600U/800U CNC machines provide an optional infrared touch probe which can be mounted on the machine replacing the tools to perform on-machine measurement (GF AgieCharmilles, 2015). Zeeko developed an on-machine stitching interferometer (OMSI) for mounting on a Zeeko IRP polishing machine to perform in-situ measurement (Zeeko, 2010). However, they have to be implemented by the machine tool manufacturers since it is necessary to access the coordinate information from the CNC controller.

Since most of the motion control interfaces of the machine tools are not open to users and researchers, it is difficult to obtain the coordinate information of the motion axis and further develop it on the machine tool for in-situ measurement. This issue also exists in the methods which integrate additional sensors into the metrology systems with motion stages. Without the coordinate information of the axes, it is difficult to combine the sensor data to obtain a holistic measurement result. Without directly accessing the coordinate information of the machines, the position of the sensor has to be estimated. Position estimation is widely used in robots. An optical fibre gyroscope (Komoriya and Oyama, 1994) was used to estimate the position of a mobile robot. However, the position estimation error was large. A drift-free position estimation method (Latt et al., 2011) was developed using inertial sensors for periodic or quasi-periodic motion. The method combined a linear filtering stage with adaptive filtering stage to remove drift and attenuation. The root mean square (RMS) error of the proposed method was about 3 μm while the maximum error was 8.9 μm.

However, the prior knowledge of the motion was needed in this method. In order to address this issue, this chapter presents a method to estimate the position of the motion axis with an additional motion sensor when the motion is controlled with a designed trajectory. With the help of a 2D laser scanner and an additional motion sensor, a multi-sensor in-situ metrology system was built and mounted on the machine tool demonstrating the high dynamic range measurement of a 3D surface. Together with the information provided by the designed trajectory, the position estimation accuracy was significantly enhanced as compared with the methods solely based on the motion sensor. The methodology and experimental setup details are described and the measurement result and its associated uncertainty are also analyzed. The successful establishment of this method provides an innovative way for in-situ high dynamic range measurement for 3D surfaces.

The proposed multi-sensor in-situ metrology system utilizes multiple sensors, i.e. the motion sensor and the laser sensor, to complete the surface measurement task. Since the measurand are different physical quantities, i.e. acceleration/angular acceleration and dimension, the metrology system is an inhomogeneous multi-sensor system. The data fusion principle developed in Chapter 4 deals with homogeneous physical quantities, i.e. both are dimensions, from different sensors. In the latter part of this chapter, a new type of homogeneous multi-sensor in-situ metrology system is built including a laser point sensor and a laser line sensor. With the Gaussian process-based data modelling method and the maximum likelihood data fusion method developed in the previous chapter, the data obtained from these two sensors are fused together and the accuracy of the fused data is improved comparing with the original data. The homogeneous multi-sensor in-situ metrology system not only further demonstrates the effectiveness of the proposed data modelling and data fusion method

in the previous chapter but also implements the data fusion method in an in-situ environment, which is a pioneer research work to fill the gap of in-situ measurement and multi-sensor data fusion for dimensional measurement.

5.2 Inhomogeneous multi-sensor in-situ metrology system

5.2.1 System configuration

Figure 5.1 shows a schematic diagram of the multi-sensor in-situ metrology (MIM) system. Without the need to build an independent metrology frame, instead, the system is built and attached to the motion axis of the machine tool as a sensor module incorporated into a specially designed fixture. The sensor module contains two types of sensors: a 2D laser scanner as a geometrical measurement sensor and a motion sensor. The sensor module is mounted on the machine tool and scans along the surface of the workpiece with a purposely-designed tool path. During the scanning of the surfaces, the data from the laser scanner and the motion sensor are simultaneously acquired by a computer system. After data processing, the coordinate

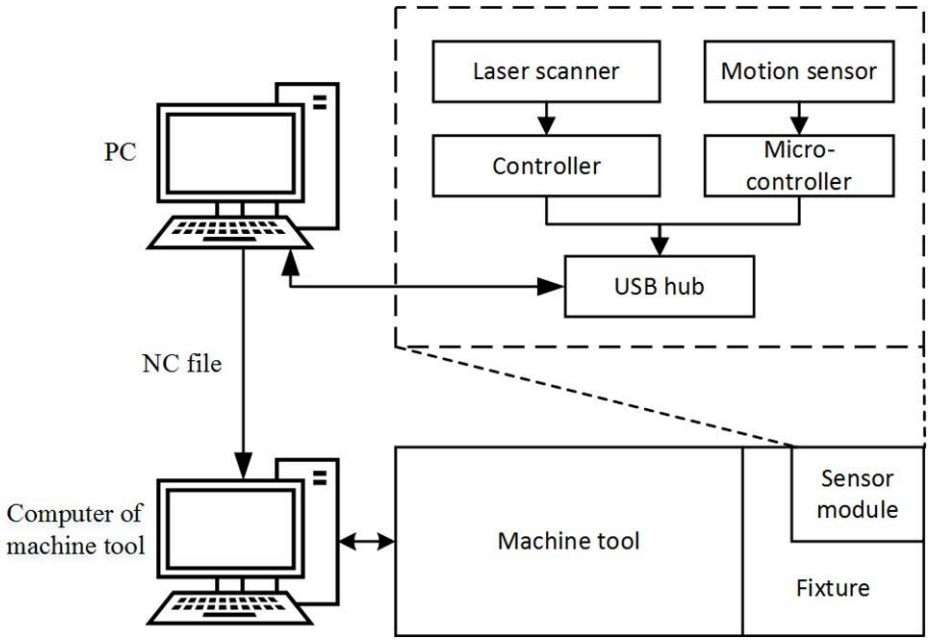

Figure 5.1 Diagram of the multi-sensor in-situ metrology system

information of the sensor module is determined by integrating the designed tool path and the motion sensor data. The whole surface can be reconstructed by the coordinate information provided by the sensor module and the laser scanner. The MIM system is mechanically attached to the machine tool. However, it is relatively independent of the machine tool since it has no direct electrical connection to the control system of the machine tool. The independent feature of the MIM system extends its application to a large field in industry. This is a very useful attribute of the MIM system.

A prototype of the MIM system was designed for a 7-axis multi-axis ultra-precision polishing machine IRP200 from Zeeko, Ltd. which is equipped with three linear axes (X, Y, Z), three rotational axes (A, B, C) and a spindle axis (H). The configuration of the motion axes is shown in Figure 5.2. With the purposely-designed and made precision fixture, the sensor module is mounted on the B axis without

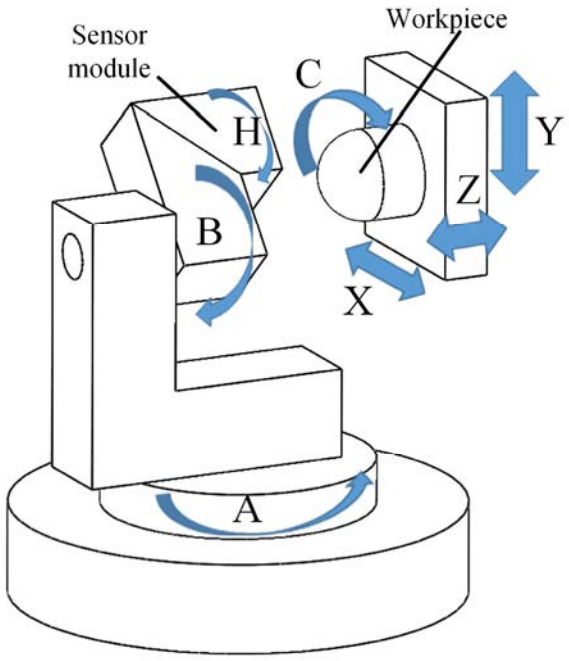

Figure 5.2 Motion axes setup of the MIM system mounted on the multi-axis ultra-precision polishing machine. The sensor module is mounted on the B axis covering H axis while the workpiece is mounted on the C axis.

removing the polishing head while the workpiece is mounted on the C axis. With this setup, the sensor module can be moved along the A and B axes and the workpiece can be moved along the X, Y, Z and C axes. This setup realizes a large scanning volume for the sensor module which enables the system to undertake large range measurement.

Figure 5.3 shows the scanning strategy of the MIM system. The scanning strategy consists of the rotational motion of the B axis and the linear motions of the X axis, Y axis, and Z axis. The A axis has a fixed angle to ensure that the laser scanner is perpendicular to the X-Y plane. The laser scanner is rotated around the B axis and a scanning slice can be generated, as shown in the highlighted zone in Figure 5.3. The workpiece is moved along the X axis, Y axis and Z axis, combined with the scanning of the B axis. As a result, the whole surface of the workpiece can be scanned. The total scanning area is large as this is determined by the moving range of the motion axis of the machine tool. The resolution of the scanning is high together with the help of the high sampling rate of the laser scanner and the motion sensor as well as a fine feed rate.

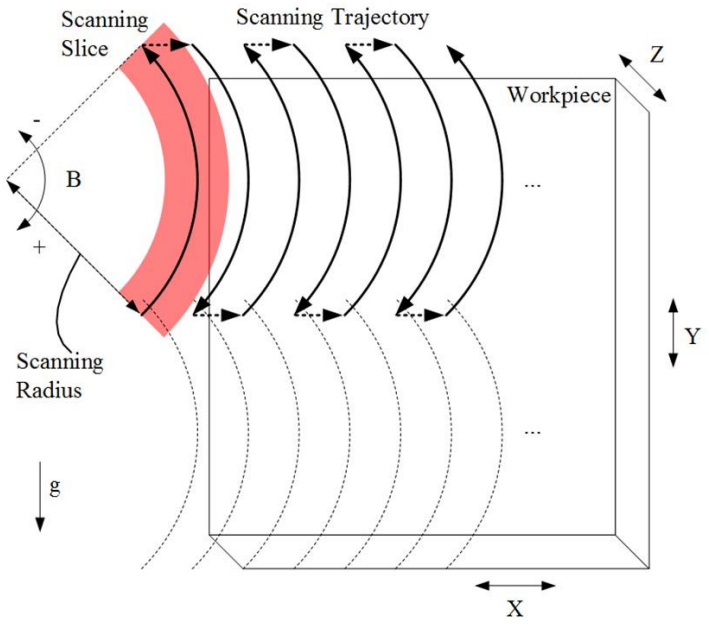

Figure 5.3 Scanning strategy of the metrology system

On the other hand, the measurement range is limited by the moving range of the motion axes while the measurement resolution is limited by the laser scanner and the sampling rate. This is different from that of single CCD camera measurement systems in which the measurement range and resolution need to be compromised. In other words, the MIM system can achieve a large measurement range with high resolution. This is the principle of the high dynamic range measurement of the MIM system.

The motion sensor consists of a 3-axis acceleration sensor and a 3-axis gyroscope. While scanning by the proposed method, the gyroscope data along the Z direction and the acceleration data in the Y (also g) direction are used to assist the determination of the position for each dataset, together with the designed trajectory. Since the data from the laser scanner and the motion sensor are obtained simultaneously, with the designed scanning angle for the B axis, the coordinate information for each line of the laser scanner can be determined accordingly. The coordinate of the sensor module is determined by the time signal combining with the space signal from the design trajectory. With coordinate transformation for the scanning lines, the whole surface can be reconstructed as a point cloud format incorporating both a large area and a high resolution. To avoid the missing of data and to provide the stitching ability for future work, the scanning slices are designed to overlap.

5.2.2 Experimental setup and procedures

The experiment was conducted on an IRP200 7-axis polishing machine from Zeeko Co. Ltd., UK. The flowchart of the process to conduct the in-situ measurement is shown in Figure 5.4. The experimental setup is shown in Figure 5.5.

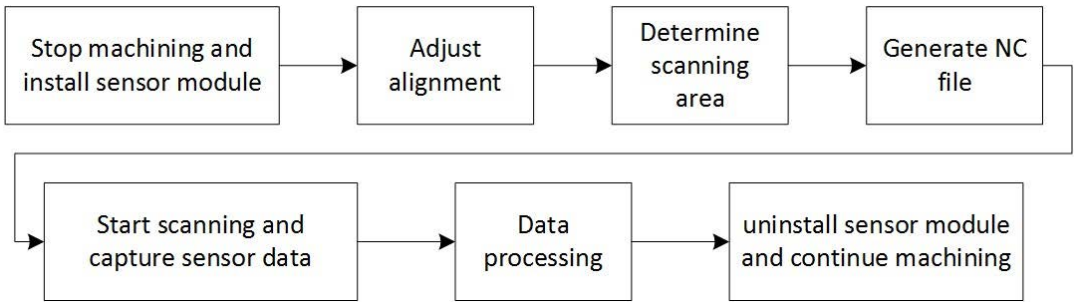

Figure 5.4 Flowchart of the process to conduct in-situ measurement

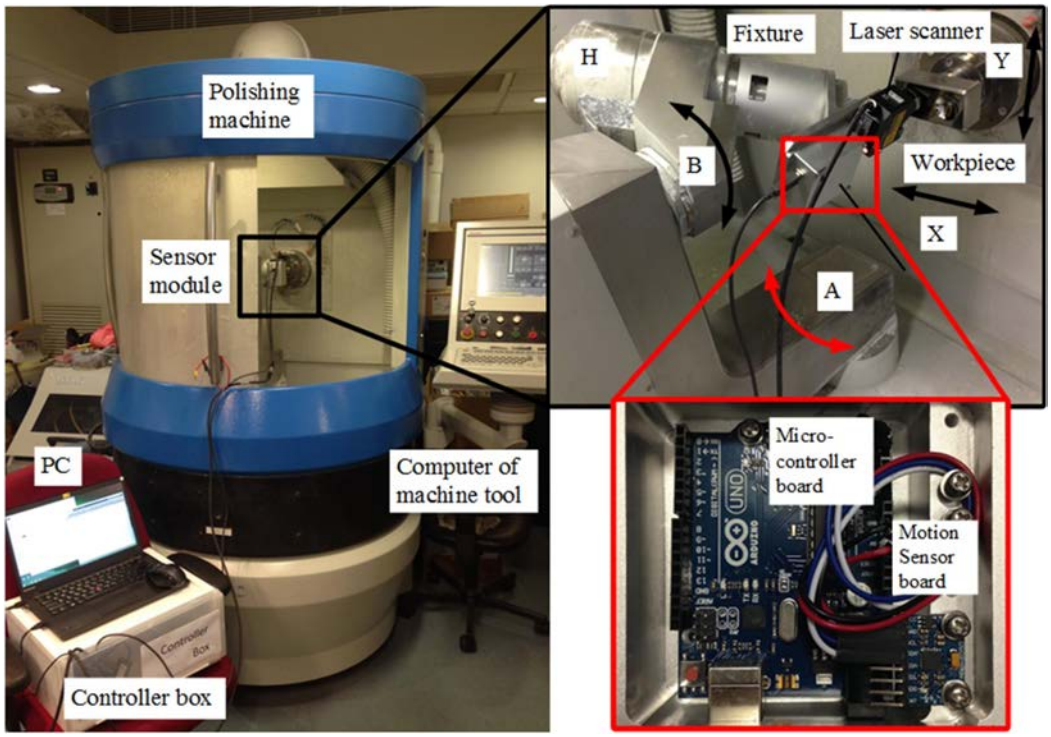

Figure 5.5 Experimental setup of the metrology system on the multi-axis machine tool

The sensor module consists of a Keyence LJ-G015 2D laser sensor, a MPU-6050 motion sensor (6-axis Motion Tracking device) and an Arduino UNO with Atmel ATmega16 micro-controller. The sensors and the associated controller and control board are shown in Figure 5.6.

(a) KJ-G015 2D laser sensor

(b) LJ-G5001 controller for the laser sensor

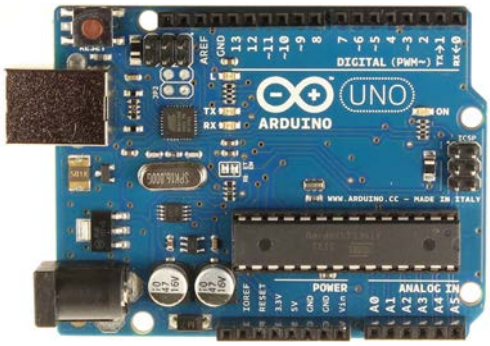

(c) Arduino Uno board

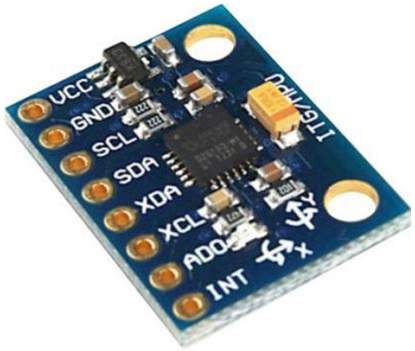

(d) Motion sensor board

Figure 5.6 Sensors and controllers in the experiment

The sensor module is mounted on the B axis via a purposely-designed fixture and the workpiece is mounted on the C axis of the polishing machine. As shown in Figure 5.7 and Figure 5.8, the fixture is designed as two separate parts. The first part

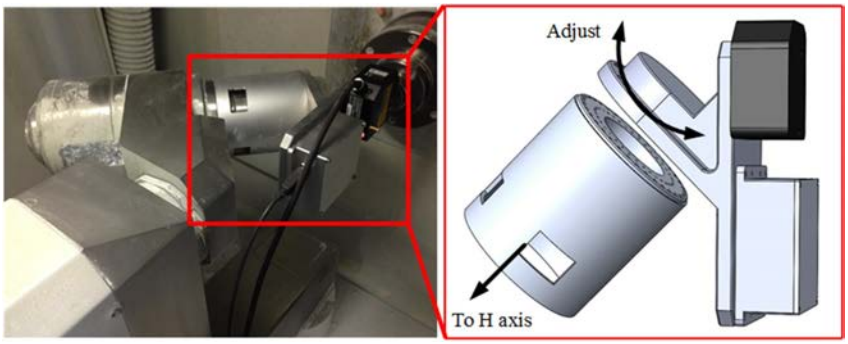

Figure 5.7 Sensor module and fixture

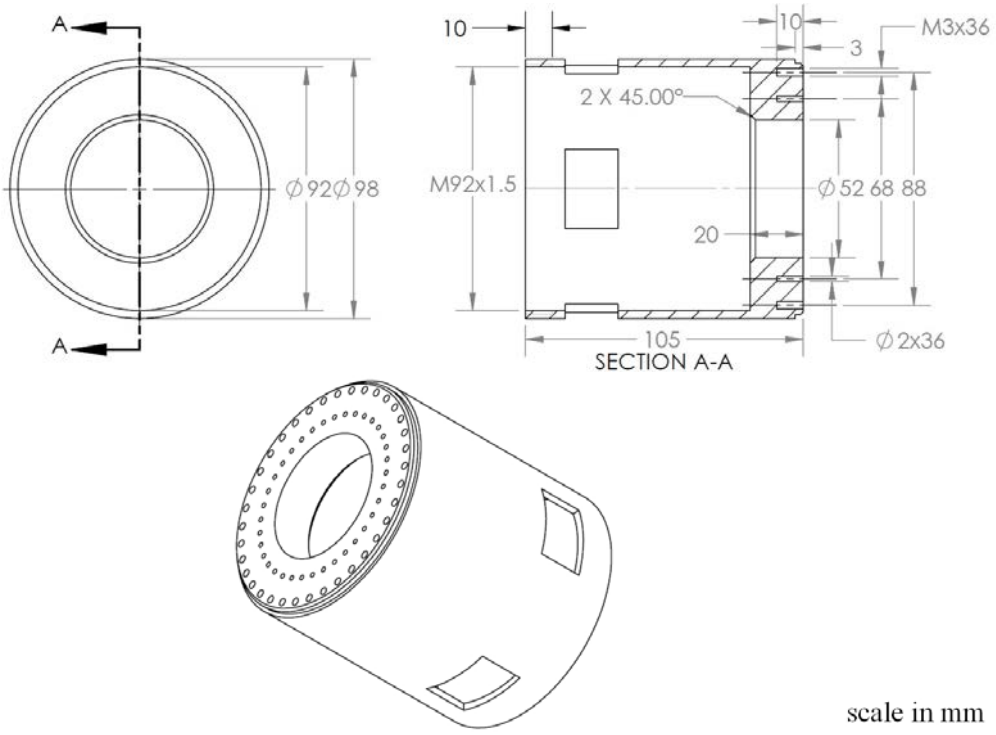

(a) The base connector

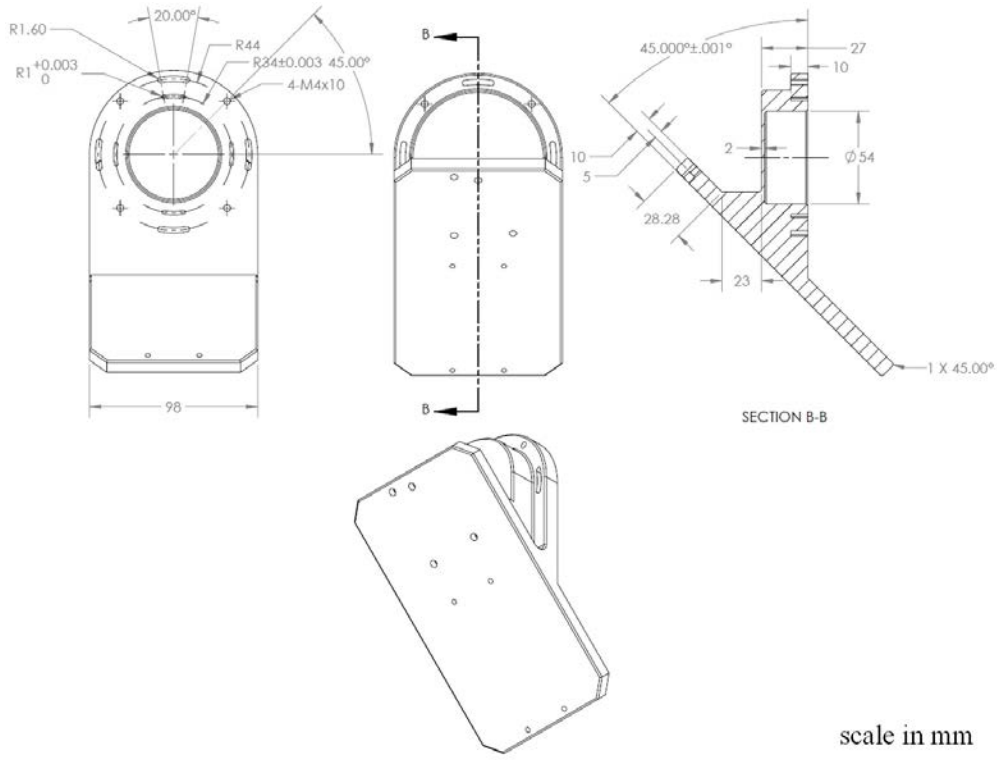

(b) The adjust plane

Figure 5.8 Design of the fixture: (a) the base connector, and (b) the adjust plane

is attached to the H axis while the second part is detachable and adjustable around the H axis for adjusting alignment purposes. The laser sensor measures a 2D profile with 7 mm length, 10 μm pitch and 4.6mm Z axis measurement range. The laser sensor is connected to a Keyence LJ-G5000 laser controller and the motion sensor is connected to the micro-controller. Both the laser controller and the micro-controller are connected to a laptop computer via a USB hub. The laptop computer communicates with the laser controller via a VB.Net library and controls the micro-controller via a USB-serial protocol purposely developed by the author. The baud rate is set to 230400 bps. The specifications of the motion sensor and the 2D laser sensor are shown in Table 5.1 and the specifications of the polishing machine are shown in Table 5.2.

Table 5.1 Specifications of the motion sensor and the 2D laser sensor

Motion sensor (InvenSense MPU-6050)	
Gyroscope full-scale range	±250°/sec
Accelerometer full-scale range	±2g
Analog-to-digital converters word length	16 bits
2D laser sensor (Keyence LJ-G015)	
Z-axis measuring range	±2.3 mm
X-axis measuring range (reference distance)	7.0 mm
Z-axis repeatability	0.2 μm
X-axis repeatability	2.5 μm

Table 5.2 Specifications of the IRP200 ultra-precision polishing machine

X axis travel range	±145 mm
Y axis travel range	±125 mm
Z axis travel range	+5 mm, -125 mm
A axis travel range	+115°, -50°
B axis travel range	±180°
C axis travel range	Continuous bi directional

The embedded software for the micro-controller is written in C programming language and the software on the laptop is written in VB.Net programming language, integrated with the application program interface (API) of the laser controller. The data from the laser sensor and motion sensor are obtained simultaneously and recorded as a data file for data processing. The recorded time for every dataset is also retained with millisecond accuracy. The data processing is implemented by Matlab programming language.

The micro-controller is designed to run a tight loop to check the command sent from the host computer. For the current design, there is only one command to process, which is the data receiving command. The communication of the micro-controller and the host PC is via the USB-to-serial port and the baud rate is set to 230400 bps, which is as high as possible to increase the data transition speed. Three axes of acceleration

data and gyro data are captured and sent for analysis. The flow chart of the firmware of the micro-controller is shown in Figure 5.9.

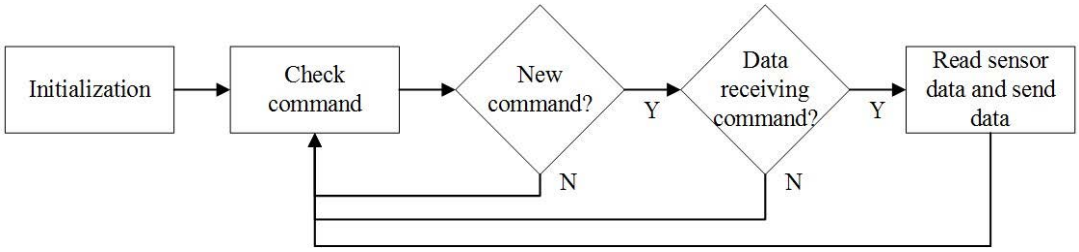

Figure 5.9 Flow chart of the firmware of the micro-controller

The VB.net program communicates with both the micro-controller and the laser sensor. The main loop of the program is written in a timer loop which is triggered every 10 milliseconds. The flow chart of the VB.net program is shown in Figure 5.10. In every timer loop, the memory of the local variables is first allocated and then checks the start measurement command. The start measurement command is controlled in the

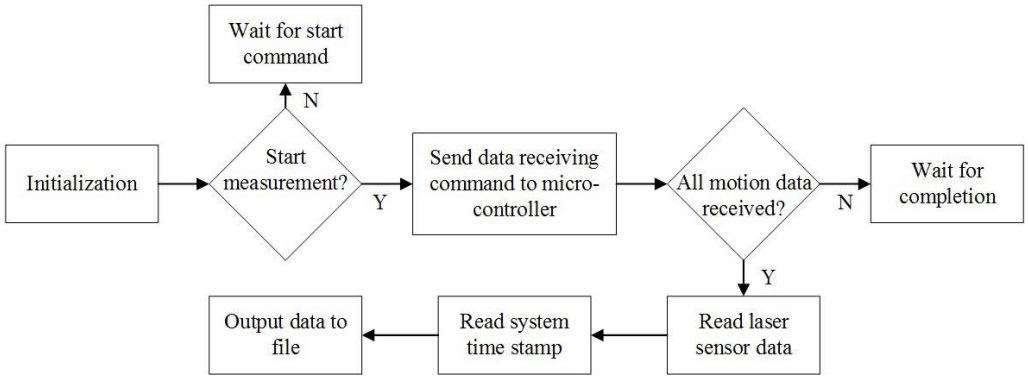

Figure 5.10 Flow chart of the timer loop of the VB.net program

UI (user interface) of the program and the UI is shown in Figure 5.11. Once the measurement command is started, the VB.net program sends a data receiving command to the micro-controller and waits for all the motion data to be received from the micro-controller. After all the motion data are received, the data from the laser sensor are retrieved and the system time is logged in millisecond resolution to

determine the actual time for the measurement data. In the end, the data are appended to a text file for further analysis. The data format of the output text file is shown in Table 5.3.

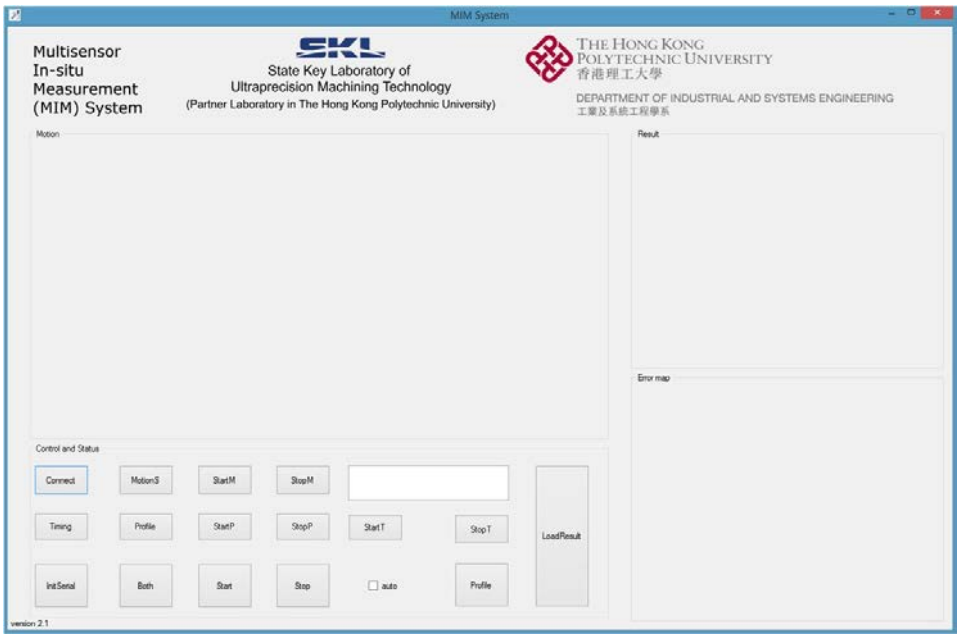

Figure 5.11 User interface of the VB.net program

Table 5.3 Data format for the output files of the MIM system

Items	Data counts	Format
Laser scanner data	800	float
Motion data	12 (2 for each component)	unsigned char
System time	3	minute/second/millisecond

A workpiece used in previous chapter was adopted for the evaluation of the developed multi-sensor in-situ metrology system. Figure 4.16 shows the drawing of the workpiece which was designed based on the concept of the Modular Freeform

Gauges (MFG) for ease of calibration (Savio et al., 2002). The dimension of the surface of the workpiece is 100 mm × 50 mm and the height is 5 mm. The process to conduct in-situ measurement for the designed MIM system starts with the installation of the sensor module and the fixture on the machine. The next step is alignment adjustment so as to minimize the installation error of the sensor module. The scanning parameters are then determined and the NC tool path file is generated. Hence, data acquisition and data processing are finally undertaken.

5.2.2.1 Alignment adjustment for the sensor module

Although the laser scanner is installed on a well-designed fixture and carefully aligned, there are still imperfections and the installation error is shown in Figure 5.12 which includes three errors: roll, pitch and yaw errors.

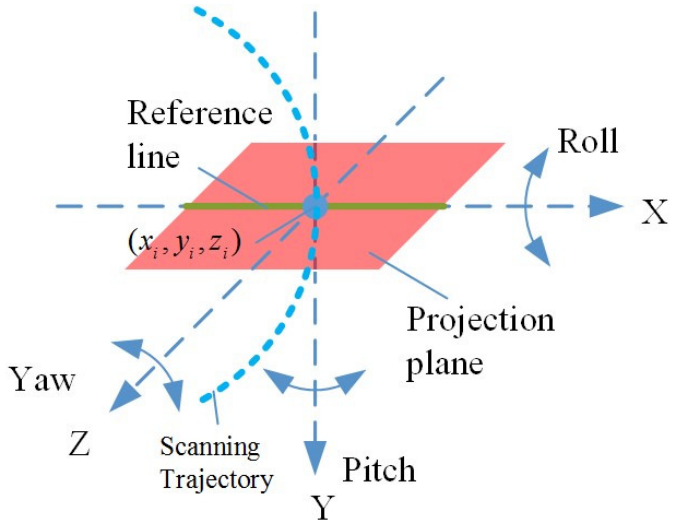

Figure 5.12 Alignment error of the laser scanner

With the designed fixture installed on the polishing machine, there are two major alignments to be adjusted. One is the perpendicularity of the laser scanner to the X-Y plane, which is determined by the angle of the A axis. The other alignment is the parallelism of the laser scanner to the X-Z plane which is determined by the angle of adjustment as shown in Figure 5.7.

To fine-tune the perpendicularity of the laser scanner to the X-Y plane, an optical flat surface was mounted on the C axis and the profile of the flat surface was measured while adjusting the angle of the A axis as shown in Figure 5.13. A best-fit line was generated to the measurement data by the least square method and the best position was determined by minimizing the tilting angle of the line.

Figure 5.13 Procedure to adjust the perpendicularity of the laser scanner to the X-Y plane using a flat surface

To adjust the parallelism of the laser scanner to the X-Z plane, a standard sphere was mounted on the C axis and the profile was measured while fine-tuning the angle of the fixture, as shown in Figure 5.14. A circle was fitted for the measured data and the radius of the circle was calculated. The best position was determined by maximizing the radius through adjusting the fixture.

Figure 5.14 Procedure to adjust the parallelism of the laser scanner to the X-Z plane using a standard sphere

After the alignment adjustment, the scanning radius of the slice was determined and is expressed by Equation (5.1).

$$R_s = |X_s| - (\frac{1}{2}L - C_x) \tag{5.1}$$

where X_s is the X coordinate of the standard sphere, L is the measurement length of the 2D laser scanner, and C_x is the X coordinate of the centre of the fitted circle.

5.2.2.2 Determination of the scanning parameters

For every measurement, the scanning parameters should be optimized to be able to cover the whole measured surface by having the right balance between scanning speed and data resolution. For the workpiece as shown in Figure 4.16 the scanning parameters are shown in Table 5.4. It is interesting to note that the scanning with the B axis and the X axis was good enough for this workpiece since the scanning range can cover the whole workpiece. After the scanning parameters were determined, the tool path was generated by the G-code as the NC file for the polishing machine.

Table 5.4 Scanning parameters

B axis range	25° ~ -25°
X axis pitch	5 mm
Feed rate	20 mm/min
Scanning Radius	73.475 mm

5.2.2.3 Data acquisition

The NC file for the scanning trajectory (see Figure 5.3) was implemented on the polishing machine and data acquisition was undertaken. The data acquisition process was controlled by the software on the laptop computer as a timer loop (15 ms). For every cycle, a command is issued by the laptop computer to the micro-controller to obtain the motion sensor data and the function is then called to receive the data from the laser scanner through the application program interface (API). The data of the laser scanner, the data of the motion sensor, and the captured time signal (in milliseconds) were stored in a text file for data processing. The time signal was recorded to solve the jitter issue in the data acquisition process.

5.2.2.4 Data processing

The data processing was done by the data processing module which is written in Matlab programming language. The first data to be analyzed were the motion data. The raw data of the acceleration data in the X, Y, Z directions and the gyroscope data in X, Y, Z directions are shown in Figure 5.15. Since the B axis was rotating around the Z axis, the most significant motion data were the acceleration data of the Y axis and gyroscope data of the Z axis. The raw data were first normalized with zero mean

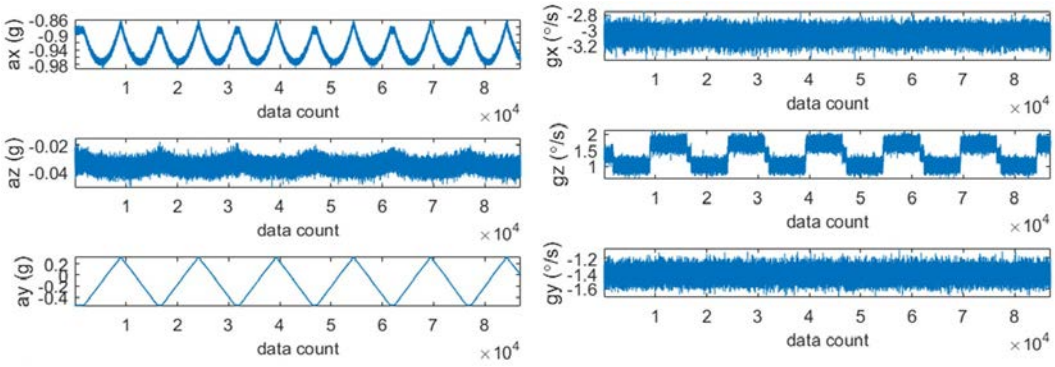

Figure 5.15 Raw data of the acceleration and gyroscope data in the X, Y, Z directions

and filtered for further processing. To avoid a phase shift in filtering which significantly affects the accuracy, a forward-backward filtering algorithm (Gustafsson, 1996) was used to filter the raw data. The normalized raw data and the filtered data of the acceleration and gyroscope are shown in Figure 5.16.

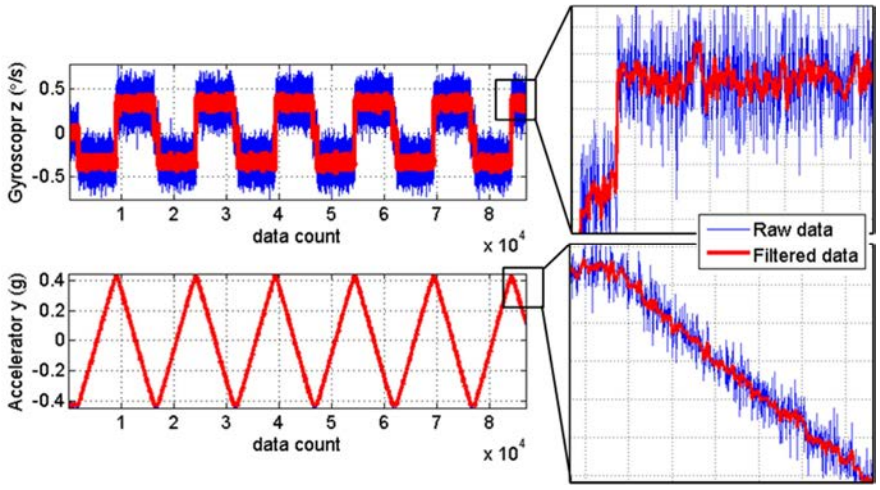

Figure 5.16 Raw data and filtered data

Since the motion was slow, the effect of the acceleration and deceleration was insignificant. In this study, the scanning slices were determined by setting two thresholds in the filtered gyroscope data for the anti-clockwise scanning and clockwise scanning, respectively. It is interesting to note that there was jitter in the data capturing process, which means that the capturing time was not evenly distributed. The jitter issue is illustrated in Figure 5.17. The result shows that the actual time between two datasets was not evenly distributed. The jitter issue is caused by the operating system of the host computer due to the fact that the Windows system is not a real-time system so that the timer is affected. In order to reduce the influence of the jitter effect, a solution was introduced as described below. Nevertheless, a real-time system will be introduced to improve the MIM system in future work.

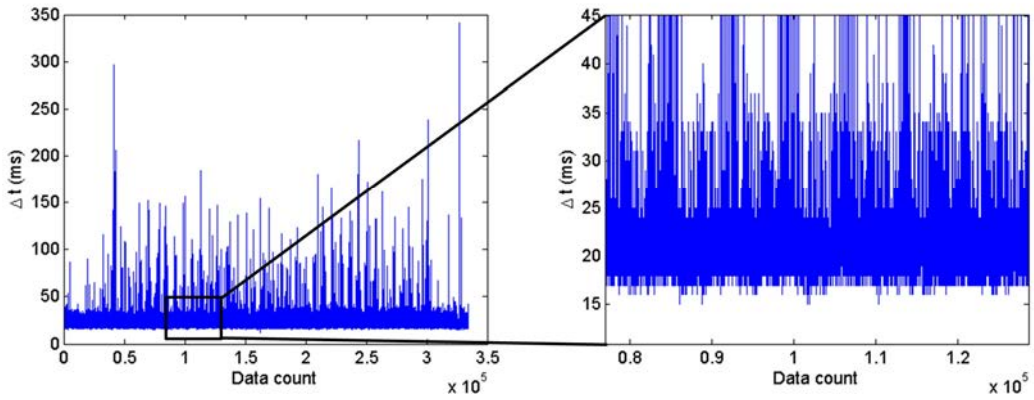

Figure 5.17 Jitter issue for the MIM system

To address this issue, the datasets within one slice and their associated scanning angle were calculated according to the actual capturing time, which is determined by Equation (5.2):

$$a_i = a_0 + \frac{t_i - t_0}{t_T} a_r \tag{5.2}$$

where a_0 is the start angle, t_0 is the start time, t_i is the capturing time for the ith dataset, t_T is the total time, and a_r is the angle of the scanning range.

After the angles for every dataset were identified, the coordinate information associated with the data from the laser scanner could be determined by the transformation matrices and the transformed scanned data can be determined by Equation (5.3):

$$S_t = M_{R_z} M_{T_x} S_m \tag{5.3}$$

where S_m is a matrix containing the original measurement data with X and Z coordinate data from the 2D laser scanner and the Y coordinate is set to zeros, M_{T_x} is the transformation matrix to translate the data according to the scanning radius, and M_{R_z} is

the transformation matrix to rotate the data according to the determined scanning angle. Thus, S_m, M_{T_x}, and M_{R_z} are determined by:

$$S_m = \begin{bmatrix} M_x \\ M_y \\ M_z \\ I \end{bmatrix} \tag{5.4}$$

where M_x, M_y, M_z are the vectors containing the measurement data from the laser scanner in X, Y and Z coordinates, respectively. I is the identity matrix with the same size of M_x, M_y and M_z.

$$M_{T_x} = \begin{bmatrix} 1 & 0 & 0 & x_T \\ 0 & 1 & 0 & y_T \\ 0 & 0 & 1 & z_T \\ 0 & 0 & 0 & 1 \end{bmatrix} \tag{5.5}$$

where x_T, y_T and z_T are the translational values in the X, Y and Z directions and they are determined by the actual setup of the fixture and the laser scanner. In this study, $x_T = 73.475$ mm, $y_T = 0$ mm and $z_T = 0$ mm.

$$M_{R_z} = \begin{bmatrix} \cos(a_i) & -\sin(a_i) & 0 & 0 \\ \sin(a_i) & \cos(a_i) & 0 & 0 \\ 0 & 0 & 1 & 0 \\ 0 & 0 & 0 & 1 \end{bmatrix} \tag{5.6}$$

where a_i is the associated scanning angle for the processing slice.

Since the scanning slices are shifting from left to right, the x coordinate of the scanned data is shifted according to the actual shifting distance which is determined by:

$$S_a = S_t M_S \tag{5.7}$$

where

$$M_S = \begin{bmatrix} 1 & 0 & 0 & x_S \\ 0 & 1 & 0 & y_S \\ 0 & 0 & 1 & z_S \\ 0 & 0 & 0 & 1 \end{bmatrix} \tag{5.8}$$

where $x_S = (n_S - 1) \times 5$, $y_S = 0$ and $z_S = 0$, n_S determines the order of the slice number.

5.2.3 Results and discussion

The measurement data were acquired in a point cloud format and the number of points for the designed workpiece was about 75 million, which indicates that there were about 15,000 points per mm^2. With a higher sampling rate, the resolution can be increased. The scanning time was about 60 minutes for a surface of 100 mm × 50 mm and the processing time was about 3 minutes. With the use of a faster microprocessor to increase the sampling rate, the feed rate can be increased and the scanning time can be shortened. To visualize the result, the measurement data were down-sampled and the result is shown in Figure 5.18. Figure 5.19 shows that the result has the resolution

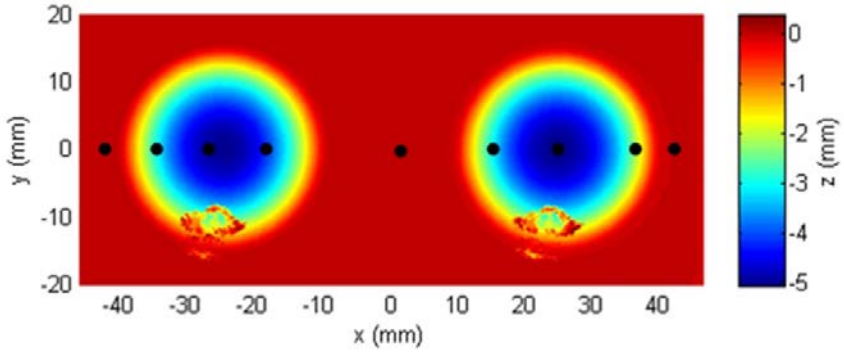

Figure 5.18 Scanned 3D surface

of about 10 µm. It is interesting to note that there was some measurement noise near the lower part of the spherical area, caused by the reflection of the laser light. The reflection area can be determined by the geometry of the surface and the angle of the laser beam. To address this issue, rotating the A axis or C axis for some specific area may be implemented in future work.

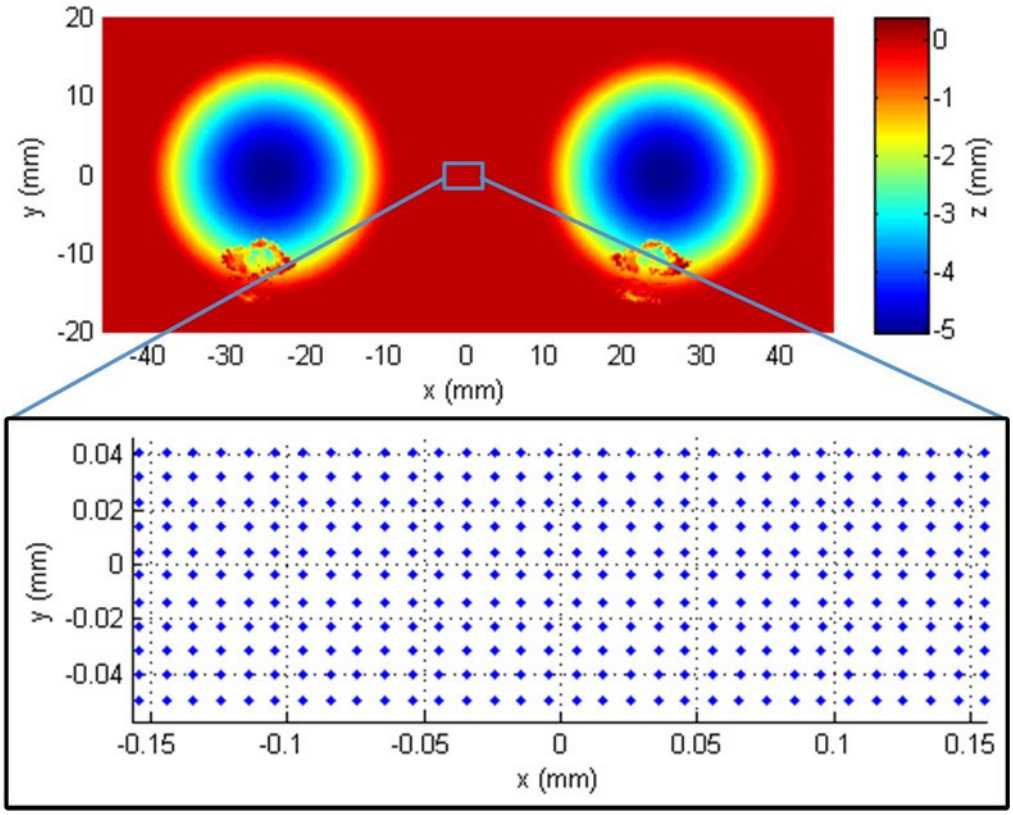

Figure 5.19 High-resolution measurement of the dataset for about 10-µm pitch

The measurement result was compared with the result measured by a Werth Coordinate Measuring Machine (CMM) (Video Check UA 400) with a touch probe TP200 (Renishaw UK). Since the measurement accuracy of the CMM is high with Maximum Permissible Measuring Error (MPE) of (0.75+L/300) µm at a temperature range of 20°C±2K and humidity of 50±5%, the probing error is as low as ±0.65 µm for the trigger probe, the measurement result of the CMM was used as a reference. The measurement result of the proposed system was registered to that of the CMM by using

an iterative closest point (ICP) method (Besl and McKay, 1992). The registration result is shown in Figure 5.20. The result shows that the two datasets were registered well.

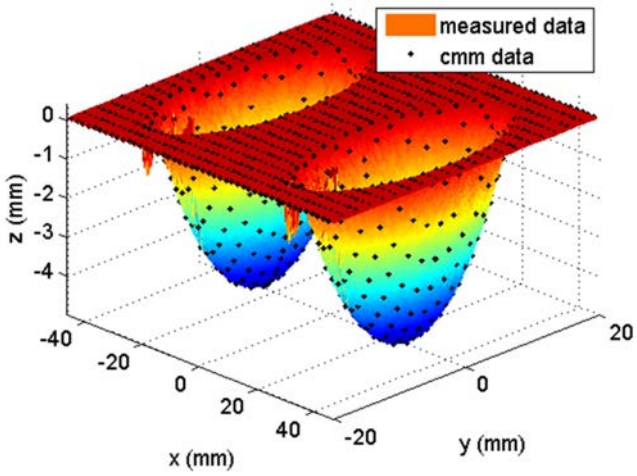

Figure 5.20 Registration result for the MIM measurement data and the CMM measurement data

One of the error maps of the measurement result is shown in Figure 5.21. The measurement result of the MIM system was evaluated at nine selected representative positions along the centre line of the surface as shown in Figure 5.18. The sample positions cover the flat and the tilted surfaces. Five repeated measurements were

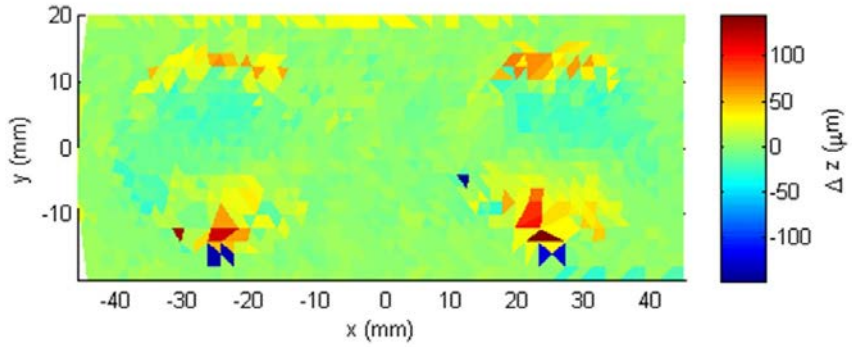

Figure 5.21 Error map of the measurement result compared with the CMM measurement data

conducted. As shown in Figure 5.22, the results were compared with the measured data by the CMM after registration. The error bar depicts the standard deviation of the repeated measurements. The result shows that measurement data at the flat surface had a higher accuracy than that at the tilted surface, i.e. 5 μm as compared to 10 μm from the reference CMM data, while the repeatability at every selected position was about ±4 μm. The uncertainty of the measurement may be due to the imperfection of the fixture, alignment error of the laser sensor, the motion error, and vibration of the machine tool. The measurement range divided by the measurement uncertainty is about 500:1 and this is believed to be able to be enhanced to 1000:1 by designing and fabricating a higher accurate fixture, the use of a higher-speed micro-controller and the incorporation of a data stitching method in future work. Moreover, a higher accurate laser scanner can be used to enhance the accuracy of the MIM system.

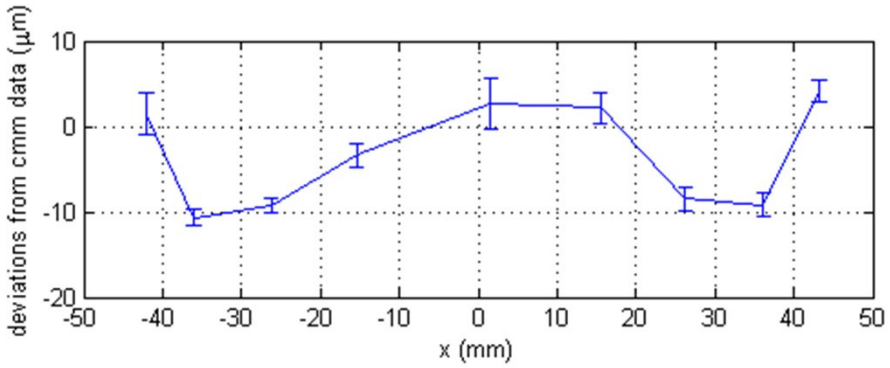

Figure 5.22 Performance evaluation of the measurement result

5.3 Homogeneous multi-sensor in-situ metrology system

The inhomogeneous multi-sensor in-situ metrology system consists of a motion sensor and a 2D laser sensor which can perform as an independent metrology system attached to a machine tool system. This is an advantage to the current machine tool systems since this method can be adapted to any kind of machine tool system or motion system as its independent characteristic. A homogeneous multi-sensor in-situ

metrology system was designed based on the inhomogeneous multi-sensor in-situ metrology system described in the previous section, which added an additional sensor system to measure the freeform surface with higher accuracy but less density. The aim of adding the additional sensor system is to improve the overall measurement accuracy with Gaussian process-based data modelling and maximum likelihood-based data fusion method as described in Chapter 4.

5.3.1 System configuration

The system diagram of the proposed homogeneous multi-sensor in-situ metrology system is shown in Figure 5.23. The multi-sensor module consists of two independent sensor systems, which are the line sensor measurement system and the point sensor measurement system, respectively. The line sensor system is based on the inhomogeneous multi-sensor in-situ metrology system described in the previous section while the point sensor is built on an accurate laser displacement sensor, which measures the surface according to the coordinate of the machine tool in the manner of an optical CMM. As a result, the detail of the newly proposed homogeneous multi-sensor in-situ measurement system is shown in Figure 5.24.

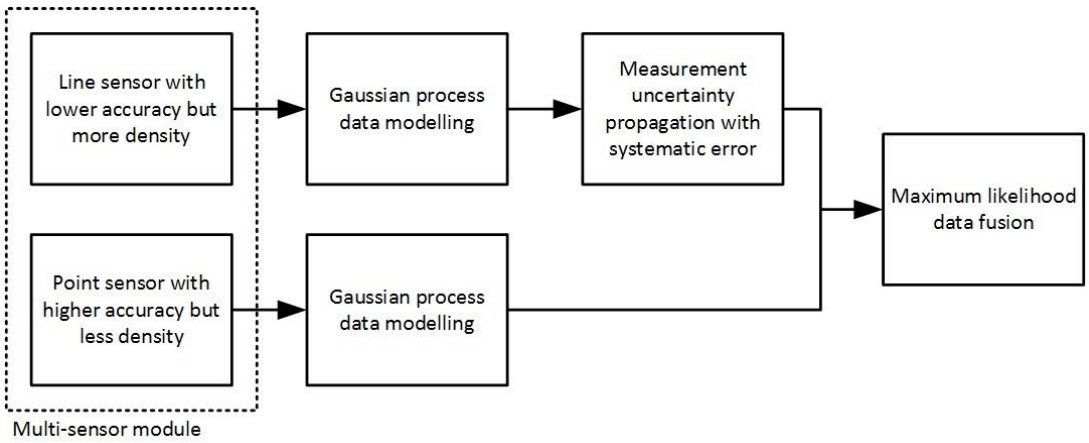

Figure 5.23 System diagram of the proposed homogeneous multi-sensor in-situ metrology system

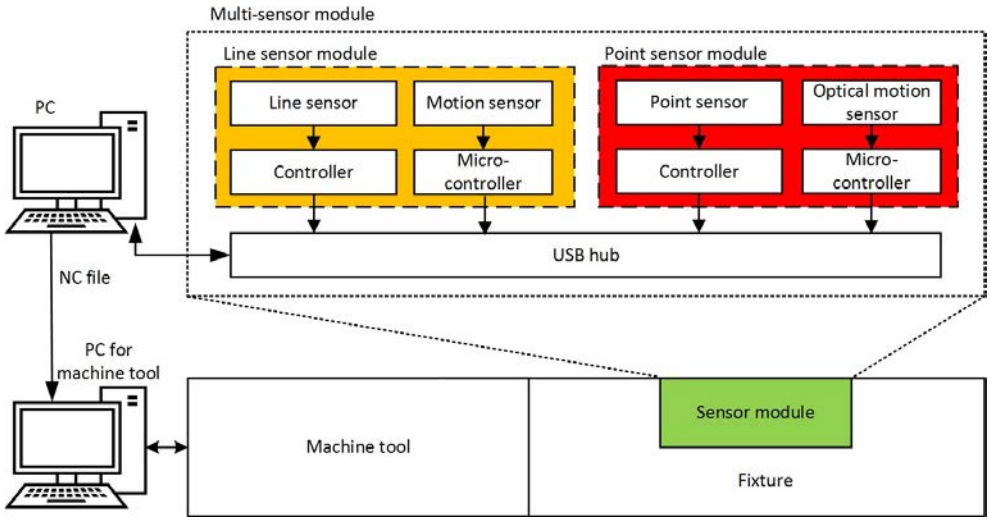

Figure 5.24 System design of the homogeneous multi-sensor in-situ metrology system

The line sensor and its controller are LJ-G015 and LJ-G5001 from Keyence with 0.2 μm measurement repeatability; the motion sensor is MPU-6050 from InvenSense with 16 bits ADC resolution; the point sensor and its controller are LK-H022 and LK-G5001 from Keyence with 0.02 μm measurement repeatability; the optical motion sensor is MCS-12085 from RMR Systems which has 400 cpi resolution; both micro-controllers are Arduino UNO. All the sensors and the micro-controller communicate with the PC via USB. The specifications of the laser line sensor and the laser point sensor are list in *Table 5.5*.

The hardware design of the multi-sensor module and the assembled system is shown in Figure 5.25. The multi-sensor module is designed to be mounted on an ultra-

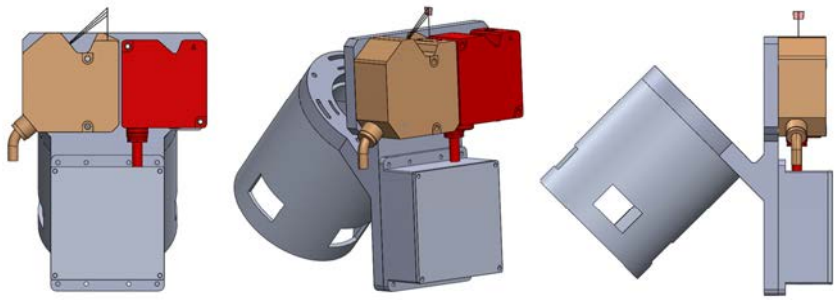

Figure 5.25 Hardware design of the sensor module

Table 5.5 Specifications of the laser line sensor and the laser point sensor

Laser line sensor (Keyence LJ-G015)	
Z-axis measuring range	±2.3 mm
X-axis measuring range (reference distance)	7.0 mm
Z-axis repeatability	0.2 μm
X-axis repeatability	2.5 μm
Laser point sensor (Keyence LK-H022)	
Z-axis measuring range	±3.0 mm
Z-axis repeatability	0.02 μm

precision polishing machine (IRP-200). The assembled system and the installation are shown in Figure 5.26. For the line sensor measurement system, the scanning setup is based on the one for the inhomogeneous multi-sensor in-situ metrology system as shown in Figure 5.27(a). For the point sensor measurement system, the displacement sensor is designed to be perpendicular to the X-Y plane of the coordinate of the machine tool. The measurement path is designed to be a raster scanning path as shown in Figure 5.27(b), which is in a point sampling configuration. The measurement path is generated by a purposely-designed MATLAB program which takes into account the scanning area, scanning pitch as input parameters and outputs the NC file which is readable for the IRP-200 polishing machine. To conduct the measurement experiment

automatically, an additional optical motion sensor was implemented to detect the X-Y motion of the machine tool and the implementation is shown in Figure 5.28.

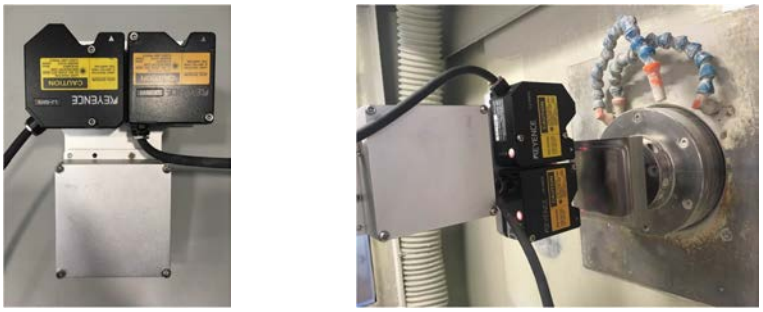

(a) Assembled sensor module (b) Installation in the machine tool

Figure 5.26 Photos of the sensor module

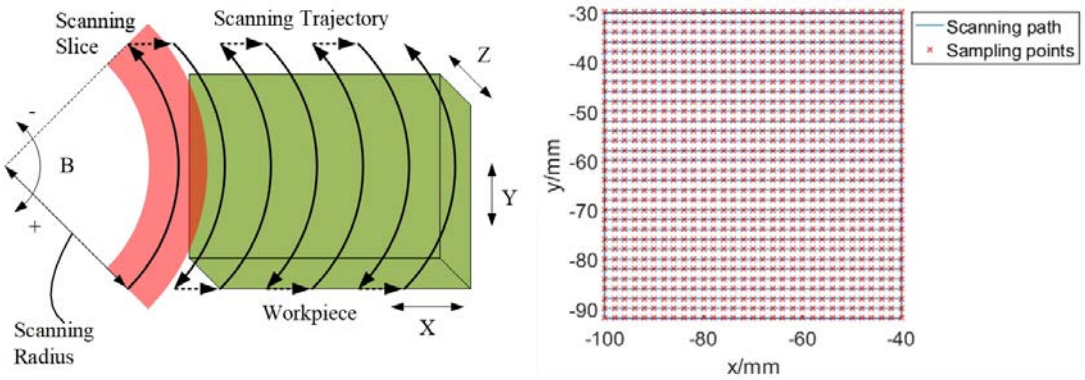

(a) Line sensor *(b) Point sensor*

Figure 5.27 Scanning measurement path for different sensors

Figure 5.28 Optical motion sensor to detect the motion of the machine tool

5.3.2 Measurement experiment

To evaluate the effectiveness of the proposed homogeneous multi-sensor in-situ measurement method and the developed multi-sensor metrology system, experiments were designed and conducted in the IRP-200 ultra-precision polishing machine. A progressive lens surface was used as the target surface which can be defined by the Zernike polynomials as shown in Equation (5.9) and the drawing of the progressive lens surface is shown in Figure 5.29.

$$\begin{aligned} z = {} & 0.462 \times \sqrt{3} \times (2x^2 + 2y^2 - 1) - 0.015 \times 2\sqrt{2}(3x^2y - y^3) \\ & - 0.046 \times 2\sqrt{2}(3x^2y + 3y^3 - 2y) \\ & + 0.007 \times 2\sqrt{2}(3x^3 + 3xy^2 - 2x) \\ & + 0.007 \times 2\sqrt{2}(x^3 - 3xy^2) \\ & + 0.0064 \\ & \times 2\sqrt{3}(10x^4y + 20x^2y^3 - 12x^2y + 10y^5 - 12y^3 \\ & + 3y). \end{aligned} \tag{5.9}$$

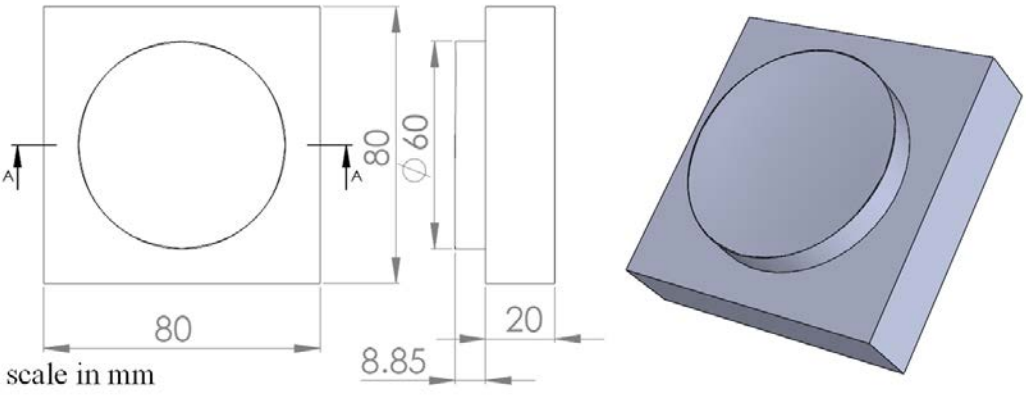

Figure 5.29 Design of the progressive lens freeform surface

The measurement process includes two steps. The first step is the measurement with the line sensor and the second step is measurement with the point sensor. The measurement setups with the line sensor and the point sensor are shown in Figure 5.30.

For the measurement setup using the line sensor, the measurement parameters are shown in Table 5.6. Figure 5.31 shows the measurement result of the line sensor and the high measurement resolution is shown in Figure 5.31(b) which has about 10-μm lateral resolution.

(a) Line sensor *(b) Point sensor*

Figure 5.30 Experiment setups with different sensors

Table 5.6 Scanning parameters for the sinusoidal surface

B axis range	25° ~ -25°
X axis pitch	5 mm
X axis range	-100 ~ -40 mm
Feed rate	20 mm/min
Scanning Radius	72.861 mm

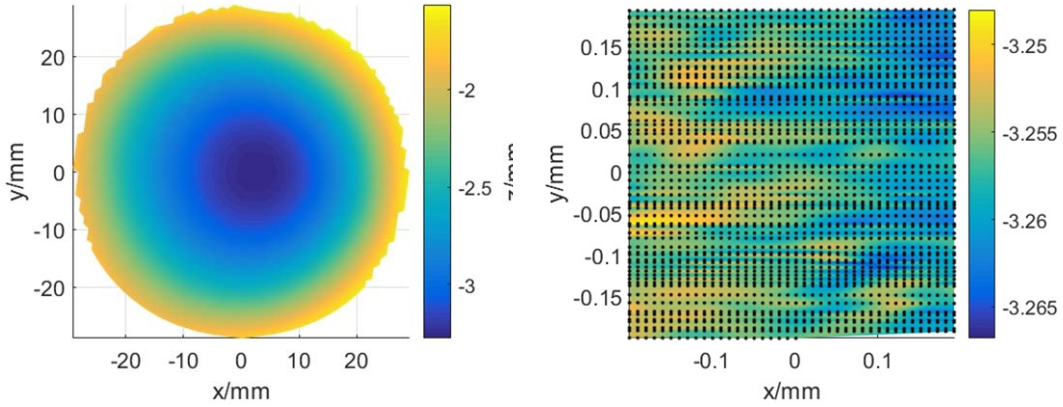

(a) Measurement result *(b) Result showing the high resolution*

Figure 5.31 Measurement result with the line sensor

The scanning parameters with the point sensor are shown in Table 5.7. The measurement result is shown in Figure 5.32. Compared with the measurement result obtained using the line sensor, the lateral resolution of the measurement result obtained by using the point sensor was much lower, i.e. 2 mm to 10 μm. From this point of view, the high dynamic range measurement of the inhomogeneous multi-sensor in-situ metrology system is an advantage since it has a relatively high lateral resolution.

Table 5.7 Scanning parameters with the point sensor

X axis range	-40 ~ -100 mm
Y axis range	-30 ~ -90 mm
Pitch	2 mm

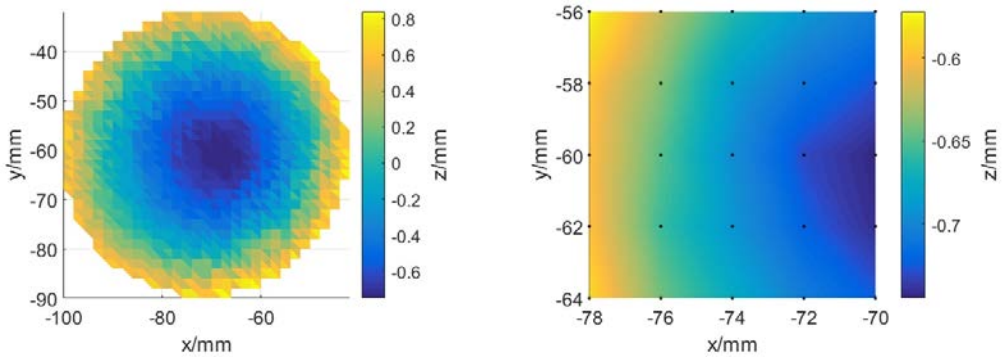

(a) Measurement result *(b) Result showing the low resolution*

Figure 5.32 Measurement result with the point sensor

5.3.2.1 Gaussian process data modelling for the measurement data

(1) Data modelling for the measurement data from the line sensor

The mean surface and the measurement uncertainty of the measurement data from the line sensor are shown in Figure 5.33. The RMS value of the associated uncertainty with the whole surface was 7 μm.

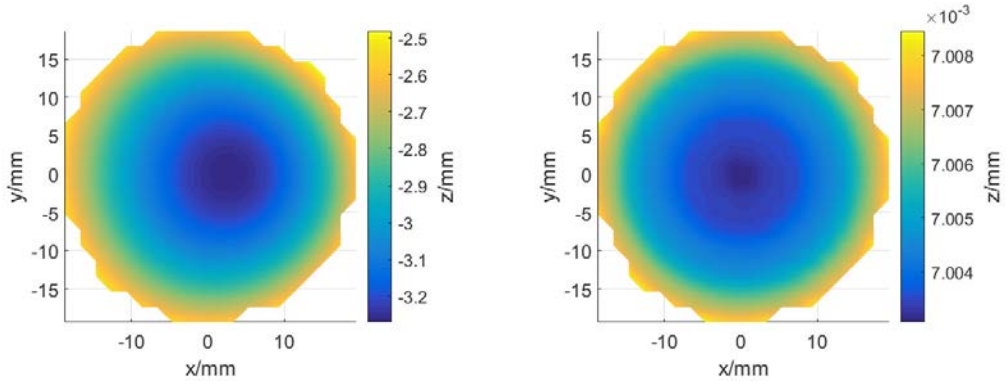

(a) Mean surface *(b) Associated uncertainty*

Figure 5.33 Result of Gaussian process for the measurement result from line sensor

(2) Data modelling for the measurement data from the point sensor

The mean surface and the associated uncertainty for the measurement data obtained from the point sensor is shown in Figure 5.34. The RMS value of the uncertainty was 5.6 μm.

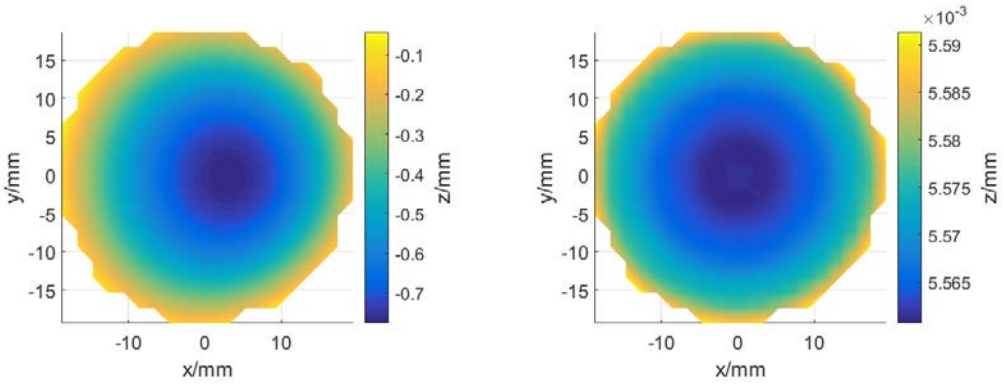

(a) Mean surface *(b) Associated uncertainty*

Figure 5.34 Gaussian process result for the point sensor

5.3.2.2 Maximum likelihood data fusion

The mean surface and the associated uncertainty for the line sensor and the point sensor were fused together by the maximum likelihood data fusion method and the result is shown in Figure 5.35. The RMS value of the uncertainty after data fusion was 4.4 μm.

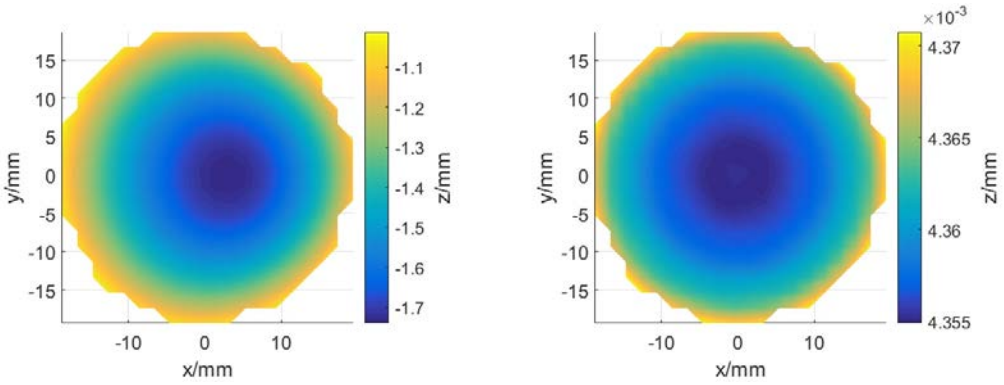

(a) Mean surface *(b) Associated uncertainty*

Figure 5.35 Result of fused data

5.3.2.3 Discussion

To evaluate the effectiveness of the proposed method, the measurement data were compared to the data measured by an accurate CMM as shown in Figure 5.36. As a result, the measurement result obtained from the CMM was used as the reference data.

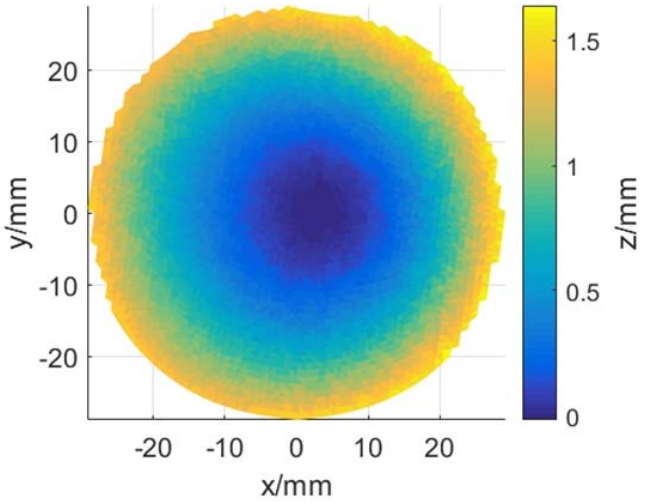

Figure 5.36 Measurement result by a CMM

The error map denoted by the deviation of the measurement data obtained from the line sensor and the point sensor to the reference data are shown in Figure 5.37. The RMS value of the error map are 5.9 µm and 8.2 µm, respectively. The deviation of the fused data to the reference data is shown in Figure 5.38. The RMS value of the error map is 4.2 µm, which has an improvement over both the original measurement data from the line sensor and point sensor. The result shows the effectiveness of the proposed data modelling and data fusion in the in-situ measurement environment. The result is summarized in Table 5.8 and Table 5.9.

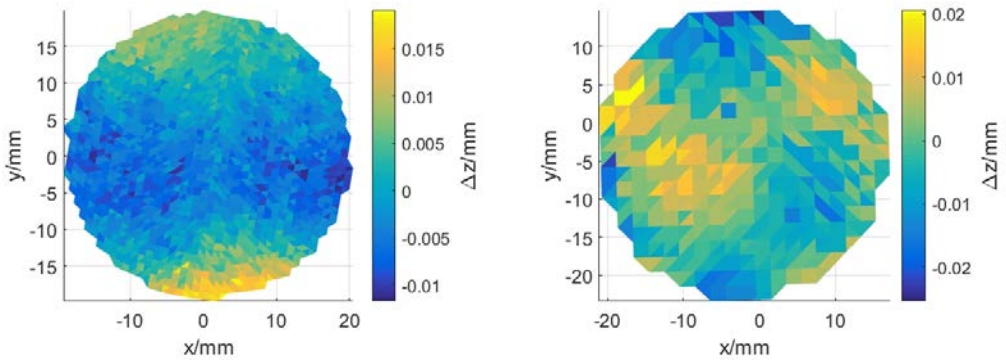

(a) For line sensor *(b) For point sensor*

Figure 5.37 Deviation of the measurement data to the reference data

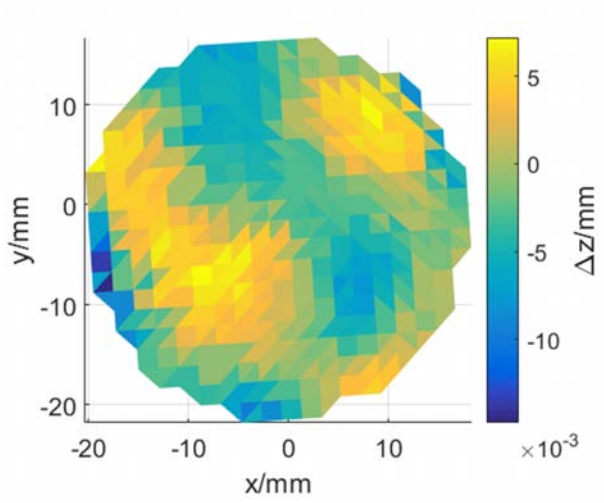

Figure 5.38 Deviation of the fused surface to the reference data

Table 5.8 RMS value of the estimated measurement uncertainty before and after data fusion

Line sensor	7 μm
Point sensor	5.6 μm
Fused data	4.4 μm

Table 5.9 RMS value of the form deviation to the reference surface before and after data fusion

Line sensor	5.9 μm
Point sensor	8.2 μm
Fused data	4.2 μm

Repeat measurement experiments were conducted and the RMS value of the measurement uncertainty and the RMS value of the form deviation to the reference surface before and after data fusion are shown in Table 5.10 and Table 5.11. In both repeat measurements, the measurement uncertainty and the form deviation to the reference surface were improved after data fusion, and the result demonstrates the effectiveness of the proposed data modelling and data fusion method in the scenario of self-developed multi-sensor in-situ metrology system.

Table 5.10 Repeat measurement results for the RMS value of the estimated measurement uncertainty

	Repeat measurement #1	Repeat measurement #2
Line sensor	6 μm	6.2 μm
Point sensor	5 μm	4.6 μm
Fused data	3.9 μm	3.7 μm

Table 5.11 Repeat measurement results for the RMS value of deviation to the reference surface

	Repeat measurement #1	Repeat measurement #2
Line sensor	5.6 μm	5.8 μm
Point sensor	7.4 μm	7.6 μm
Fused data	4.2 μm	4.5 μm

5.4 Summary

In this chapter, an autonomous multi-sensor in-situ measurement system has been reported which attempts to enable the precision machine tools to perform high dynamic range measurement of three-dimensional (3D) surfaces. This system makes use of a motion sensor to assist the estimation of the position for a 2D laser scanner while it is scanning with a purposely-designed trajectory. Without interfacing with the motion controller of the machine tool, this system possesses very high feasibility and it can be easily integrated into different machine tools. The result shows that the method is not only suitable for in-situ measurement but also provides high dynamic range measurement results with large measurement area and high resolution. The measurement uncertainty of the system is in the order of 10 micrometres, which depends on the alignment of the sensor and the fixture.

Furthermore, a homogenous multi-sensor which contains two types of optical sensor including a line sensor and a point sensor was built for in-situ measurement of freeform surface in a precision machine tool. The Gaussian process data modelling and maximum likelihood data fusion method presented in Chapter 4 was implemented

in the developed system. The experiment results show that the fused data had improvement over both the original data from different sensors, regarding the measurement uncertainty and error presented by the form deviation from the reference surface.

Chapter 6 Overall conclusions and suggestions for future work

6.1 Overall conclusions

The fast-developing technologies in various industries such as biomedical and advanced optics and their widespread applications have generated abundant research and development pertaining to the design, manufacturing and measurement of objects with freeform surfaces. Unlike the traditional parts with simple shapes such as planes and spheres, freeform surface is inherently complex and this poses a lot challenges for the manufacturing and measurement processes. This is particularly true when the requirements for freeform surfaces are developing in line with the trends of the overall size of workpieces becoming larger, the feature size of the microstructures becoming smaller, the surface form becoming more accurate and the surface roughness becoming smoother, etc. The requirement for measurement is even more stringent since the accuracy of measurement is always required to be one order higher than for machining. It is extremely difficult to meet all these requirements in a specific measurement instrument based on a single sensor or single measurement principle.

As a result, researchers are building numerous kinds of new measurement instruments which are based on the multi-sensor principle since their measurement ability can be significantly improved by utilizing the different characteristics of different kinds of sensors. There are more and more commercially available multi-sensor instruments such as multi-sensor CMMs in the advanced market and more and more literature available in the research field. Nonetheless, the research and development of multi-sensor techniques for dimensional measurement is still

relatively new and there still exists research gaps and plenty of room for further study, especially in the field of freeform surface measurement. Recapping the research objectives stated in Chapter 1, the conclusions of the research work done in this thesis can be list as below:

(i) To develop a stitching method for high dynamic range measurement of precision freeform surfaces for multiple measurement of single-sensor instruments. There is always large stitching error when the number of sub-surfaces is large for high dynamic range measurement using the stitching method. This is due to the fact that the rotational stitching error such as yaw, pitch, and roll is accumulating and this error is difficult to compensate for. Another issue is that there is always an obvious edge observed in the overlapped area of the fused result which is caused by the lack of a suitable data fusion method to combine the data from different datasets. This phenomenon is widely seen even in commercial surface measurement instruments. To address this issue, a Gaussian process and image registration-based stitching method and edge intensity data fusion method have been developed for high dynamic range measurement of precision surfaces. The data from the original datasets are first modelled by the Gaussian process data modelling method to obtain the underlying surface, which can reduce the effect caused by the measurement noise and improve the registration accuracy. The datasets are then registered together in a X-Y-Z translation manner with an image registration and *z* axis minimum least square error alignment method. Finally, the data in the overlapped region are fused together by an edge intensity method which balances the weighting for each data from different nearby datasets. With the proposed stitching method, the rotational stitching error can be significantly reduced and the transition effect in the overlapped area can be largely

improved. Furthermore, the proposed method is a generic method which can be implemented in a wide range of surface instruments.

(ii) To develop a Gaussian process data modelling and maximum likelihood data fusion method to model the measurement data and fuse them together to further increase the measurement accuracy. The performance of the measurement including the accuracy of the measurement result can be improved by fusion of the datasets measured from different kinds of sensors in multi-sensor measurement scenarios. This is realized by proposing a generic Gaussian process-based data modelling method and a maximum likelihood-base data fusion method. The datasets measured from two sensors are first modelled using the Gaussian process-based data modelling method to obtain the mean surface and the covariance surface which represent the associated measurement uncertainty. The proposed Gaussian process-based method is powerful to model the measurement dataset to estimate the true surface and associated measurement uncertainty at every location in a single measurement. Unlike the traditional method, where the measurement uncertainty is usually obtained by the specifications of the sensor or repeated measurement experiments, the Gaussian process modelling method evaluates the result for the measured surface and determines the measurement uncertainty in a machine learning manner. The accuracy of the Gaussian process modelling method was evaluated through repeated measurement experiments and the results were also compared with the specification of the sensor. The influence of the form error and the measurement noise was also studied thoroughly. The result shows that the Gaussian process-based data modelling method is effective for modelling the measurement uncertainty. The method is a generic method and it is independent of the sensor type which makes it widely applicable to various kinds of dimensional measurement sensors. After obtaining the mean surface and the associated measurement uncertainty of the two

datasets measured from different sensors, the mean surface and the associated measurement uncertainty are fused together with a maximum likelihood-based data fusion method and the fused mean surface and the fused associated measurement uncertainty is determined. Moreover, the uncertainty propagation is clear from the maximum likelihood method since it follows the uncertainty propagation method suggested in the GUM (Guide to the Expression of Uncertainty in Measurement), which makes the uncertainty analysis straightforward. Furthermore, the influence of the systematic error in the fusion process was studied thoroughly and some special situations were identified which should be avoided or should be paid more attention to, where the performance of the fusion result is affected.

(iii) To develop an in-situ metrology system for high dynamic range measurement for precision freeform surfaces on precision machine tools. In order to minimize or even eliminate the repositioning error in an error compensation scenario where re-mounting of the workpiece is required, an in-situ metrology system is much needed but this is not usually equipped on machining facilities. Installing an additional dimensional sensor on the machining facilities is difficult since the coordinate information is not accessible to users and researchers. As a result, an autonomous multi-sensor in-situ metrology system for high dynamic range measurement of freeform surfaces on precision machine tools was developed which fuses the time-space data from the motion sensor, 2D laser scanner and the designed trajectory to obtain a holistic 3D measurement result. The motion sensor and the laser scanner together with the electronics were installed in a fixture which was in turn installed on the machine tool as a sensor module. With a purposely-designed trajectory and a motion sensor such as accelerometer and gyroscope to measure the motion signal, the coordinate information of the sensor module can be determined and so the signal measured by the laser scanner can be transmitted to the machine coordinate system.

With a user developed fixture installed on the machine tool, the alignment is significant since it directly influences the accuracy of the measurement result. A self-alignment method was introduced to align the perpendicularity of the laser scanner to the X-Y plane and the parallelism of the laser scanner to the X-Z plane. The developed system measures the workpiece over a large range which is as large as the motion range of the machine tool and with a high lateral resolution which is determined by the resolution of the laser scanner. This ensures the high dynamic range measurement of the developed system. With the developed system, the in-situ measurement ability of machine tools is enabled without the need to access the control systems of the machine tools, which makes this method more adaptable to a wide range of industrial applications. The performance of the in-situ metrology system was determined by comparing the measurement result with that from a high-precision CMM. Moreover, repeated measurements were also conducted to verify the measurement uncertainty of the system.

(iv) To develop a multi-sensor in-situ surface measurement instrument equipped with the proposed data modelling and data fusion method together with in-situ measurement ability. Finally, a homogenous multi-sensor in-situ metrology system equipped with a laser line sensor and a laser point sensor was developed to demonstrate the effectiveness of implementation of the proposed data fusion method in an in-situ environment. The metrology system combines the two independent in-situ metrology systems installed on a precision machine tool and integrates with the proposed Gaussian process data modelling and maximum likelihood data fusion measurement instrument. The sub-system including the laser line sensor provides high dynamic range measurement results for a large measurement range and high measurement resolution, where the measurement accuracy is limited by the alignment of the sensor and the fixture together with the scanning algorithm. On the contrary, the

sub-system including the laser point sensor provides highly accurate measurement results but the number of sampling points is limited since the measurement principle is point measurement. The overall accuracy of the fused data can be improved by combining both datasets from the two sub-systems. This is the first implementation of a multi-sensor data fusion system for an in-situ measurement scenario and the effectiveness of the data modelling and data fusion is also demonstrated.

The main contributions of this study are summarised as below:

(i) To address the data fusion issue with single-sensor multiple measurement, a Gaussian process and image registration-based stitching method is proposed which has achieved accuracy improvement regarding the rotational stitching error. The method utilizes the Gaussian process data modelling method to model the original sub-surfaces so as to obtain the underlying surface to reduce the influence of measurement noise. The datasets are then projected onto a common plane to form subsequent 2D images and the nearby datasets are then registered by an image registration method. In the proposed method, the traditional 6 degrees-of-freedom (DOF) registration problem is translated to a simplified 3 DOF translational registration problem. As a result, the computational complexity is greatly reduced. Moreover, the accumulated rotational error found in the traditional stitching method is greatly reduced. An intensity edge data fusion method is also implemented to minimize the edge effect in the overlapped region. Generally, the proposed method is a generic stitching method which is suitable for most of the surface measurement instruments which can be extended to a wide range of applications. This is a very valuable contribution for high dynamic range surface measurement in which a large measurement range and high measurement lateral resolution are required. This contribution fills the research gap for the multiple measurement data fusion method

with a single-sensor instrument where the accuracy of the fusion result undergoes improvement regarding the difficult-to-compensate rotational error and large edge effect in the overlapped region.

(ii) To address the data fusion issue with multi-sensor multiple measurement, a generic Gaussian process-based data modelling and maximum likelihood-based data fusion method was developed to further increase the measurement accuracy using fused measurement data from different kinds of sensors. Both the data modelling method and data fusion method are data-oriented which make the method generic and independent of the sensor types. Both the datasets measured by the two sensors are first modelled by the Gaussian process modelling method, while the mean surface and covariance surface are obtained which represent the best estimated underlying surface and the associated measurement uncertainty. The modelling accuracy of the Gaussian process was studied thoroughly by comparing the measurement results with the specifications of the sensors and the result from the repeated measurements. A maximum likelihood-based data fusion was then utilized to fuse the mean surfaces and the associated measurement uncertainties so as to obtain a theoretically best estimated mean surface and reduced associated measurement uncertainty. The uncertainty propagation with the fusion method is traceable and this is very useful for deterministic dimensional measurement. The proposed method was verified experimentally and repeated measurements have also been conducted for verification. The influence of the system was also studied and some special cases which should be avoided or more attention paid to are pointed out in practice, i.e. the systematic error needing to be minimized by careful calibration with known or more accurate datasets.

(iii) An autonomous multi-sensor in-situ metrology system for high dynamic range measurement of freeform surfaces has been developed. The system

measures the freeform surfaces on precision machine tools with the addition of a laser scanner and motion sensor. The measurement range can be as large as the moving axes of the machine tool, while the measurement resolution can be as high as the laser scanner, which is the fundamental of high dynamic range measurement. The innovativeness of the system is that it makes use of the motion sensor, the designed trajectory and the laser scanner to perform independent, holistic measurement of freeform surfaces without the need to interface with the control system of the machine tool. This makes it widely extendable to a large field of industrial applications. A self-alignment method is also proposed to align the sensor module with the machine tool. A prototype of the system was developed for a 7-axis computer controlled ultra-precision polishing machine and a series of experiments was conducted to verify the accuracy and repeatability of the system. The successful establishment of the proposed metrology system provides a new method to extend the measurement ability for the precision machine tool especially those for which the interface is not open to users.

(iv) Taking the developed Gaussian process data fusion and maximum likelihood data fusion method as well as the developed autonomous multi-sensor in-situ measurement method into account, a novel homogeneous multi-sensor in-situ metrology system was developed of its first kind which is composed of two types of sensors including a laser line sensor and a laser point sensor to perform in-situ high dynamic range measurement on a precision machine tool. The sub-systems based on a laser line sensor and a laser point sensor are independent inhomogeneous systems which provide high-resolution measurement data and highly accurate measurement data, respectively. Fusion of the datasets from the laser line sensor and laser point sensor provides a more accurate measurement result with high resolution. The successful establishment of the proposed homogeneous multi-sensor in-situ metrology system demonstrates that the proposed Gaussian process data modelling and maximum

likelihood data fusion method is not only applicable for high-precision off-line measurement instruments, but also suitable for wide industrial applications even in the situation of in-situ measurement.

The present study contributes to a wide range of measurement science and technology and it is also focused on the multi-sensor measurement methods for measuring freeform surfaces. The Gaussian process and image registration-based stitching and data fusion method contributes significantly to a wide range of applicable surface measurement instruments. The multi-sensor measurement method based on the Gaussian process and maximum likelihood principle and the multi-sensor measurement method not only contribute to the research and development for multi-sensor CMM measurement to conduct autonomous in-situ high dynamic range measurement, but also provides a new insight into the science and technology for measurement development on machine tools. The integration of the proposed Gaussian process data modelling and data fusion method together with the in-situ high dynamic range measurement method fills the research gap of the development of in-situ multi-sensor surface measurement instruments.

6.2 Suggestions for future work

Multi-sensor data fusion is emerging in the field of dimensional measurement and the research and development have attracted a lot of research attention. The possibility to integrate different kinds of sensors with different characteristics has been proven to have the ability to improve measurement capability, accuracy, and efficiency, and can even introduce some special functions such as high dynamic range measurement. However, due to the complexity of freeform surface and the measurement process involving various disciplines, there is still a large potential for

further research and development. Some suggestions of future work are discussed as follows:

(i) Different kinds of measurement errors are determined by the integration of different characteristics of the measured surface and the characteristics of different sensors used for the measurement, together with the uncertainty introduced in the measurement process. A multi-sensor CMM equipped with different kinds of sensors provides the ability to select specific kinds of sensors to perform specific kinds of measurement corresponding to the workpiece. A database for the characteristics of different kinds of sensors and the characteristics of different kinds of surface will be suggested to be built and the corresponding model of measurement uncertainty will be established. For example, the sensor can be optical sensors such as laser scanner, imaging sensor, and white light interferometer, or it can be contact sensors such as touch trigger probe, opto-tactile fibre probe, and AFM-based micro probe. The optical sensors may be affected by specular reflection of the workpiece with mirror surface finishing, and the surface roughness and surface gradient, so the measurement uncertainty is not easy to determine. However, they usually possess fast measurement speed and have a large volume of measurement data. The contact sensors are sensitive to soft material, and the factors influencing the accuracy of radius compensation and the measurement speed are usually slow. Nevertheless, the measurement result of the contact is considered to be more reliable and accurate. The establishment of such databases for sensors and workpieces is a large systematic project which requires a lot of rigorous basic research and experiments. However, its establishment will strengthen the foundation for the further development of multi-sensor dimensional measurement. As a result, future work focused on studying the sensor characteristics for various kinds of sensors is suggested.

(ii) Data modelling using the Gaussian process is a promising technology due to its data driven and sensor independent nature. Different target surfaces should have different mean surfaces in Gaussian process modelling which may improve the accuracy and efficiency of the modelling method. Currently, the mean surface is set to be zero mean surface since the measured surface is assumed to be unknown. However, in practice, most of the target surfaces will be well defined by mathematical models. Utilizing the a priori knowledge of the target surface to establish the corresponding mean surface will be suggested for further study which may allow improvements in the modelling result, as well as in modelling efficiency. This is especially useful when the measurement result has a large amount of data, since the computational speed of the Gaussian process is extremely slow when dealing with large datasets. Hence, an a priori knowledge-based Gaussian process modelling method is suggested for future study.

(iii) Systematic error adversely influences the performance of the maximum likelihood-based data fusion method. An automatic detection method for the systematic errors is greatly needed to identify the systematic error and change the weighting in the fusion algorithm so as to improve the overall accuracy of the fused result. The systematic error can be large especially for some optical measurement instruments since they will be severely affected by factors such as surface tilting and specular reflection. If this kind of systematic error is used in the fusion process, the fused result will be greatly affected and the overall performance influenced. This will work with the suggestions in (i) to have a priori knowledge of the sensor and the workpiece to assist the estimation of the possible obtained measurement noise in the result. The noisy data will be further removed or set with an associated weighting depending on the noise level in the modified maximum likelihood-based data fusion algorithm to reflect the handling of the systematic error. With different kinds of

measurement sensor, this implementation is very promising since different kinds of sensors would have different levels of systematic errors and using different weighting will enable significant improvement of the fusion result. Hence, an intelligent sensor selection and data modelling method and development of such kind of measurement system is suggested in future study.

(iv) With a higher sampling rate of the data from the motion sensor and the data from the laser scanner, the resolution of the scanned data will be improved and the accuracy of the measurement result will be increased. This can be realized by using a high-performance micro-controller and a high-speed communication protocol between the micro-controller and computer. Moreover, the whole system can be upgraded to a real-time operating system-based design to avoid the jitter issue to improve the performance of the system. Furthermore, an intelligent tool path generator will be developed to automatically generate the scanning trajectory according to the topography of the workpiece. A more accurate fixture will also be made and a self-calibration method to determine the 6 degrees-of-freedom alignment error will be developed to further improve the accuracy of the measurement result. With the improvement of the accuracy of the in-situ metrology system, the industrial applications will be largely extended and hence future study is suggested.

Appendix A Specification of Werth VideoCheck UA Multi-sensor CMM

Werth VideoCheck UA is an ultra-precision 3D CNC bridge-type coordinate measuring machine. It integrates the multisensory concept which supports combined measurements with several sensors. The specification of Werth VideoCheck UA is listed as below:

- Measuring range: X = 400 mm, Y = 400 mm, Z = 250 mm
- Maximum permissible error (MPE)

a) Unidirectional – MPE

E1: (0.15+L/900) µm

Temperature range: 20±0.1 ºC

Temperature gradient: 0.1 ºC/h

Humidity: 50±5% rel. humidity

b) Unidirectional – MPE

E1: (0.15+L/500) µm

Temperature range: 20±2 ºC

Temperature gradient: 0.5 ºC/h

Humidity: 50±5% rel. humidity

c) Unidirectional – MPE

E1: (0.15+L/120) µm

Temperature range: 16 ºC - 30 ºC

Temperature gradient: 1 ºC/h

Humidity: 50±5% rel. humidity

L = Measuring length in mm

- Sensor image processing IP with telocentric optics

Resolution: 1360×1024 pixels

MPE

a) With lens 5×:

   for P1Z: 1.10 µm

b) With lens 10×:

   For P1Z: 0.75 µm

c) With lens 20×:

   For P1Z: 0.50 µm

- WERTH FIBER PROBE

a) MPE (point-to-point probing)

   0.25 µm

b) MPE (scanning operation)

   1.5 µm

Appendix B Specification of Zygo Nexview

Zygo Nexview is a 3D optical surface profiler. As a coherence scanning interferometer (CSI), it can measure both smooth and rough surfaces with sub-nanometre precision. The main specification of the Zygo Nexview is listed below:

- Vertical scanning range

  150 μm

- Surface topography repeatability

  0.08 nm

- Optical lateral resolution

  0.34 μm (100× objective)

- Step height repeatability

  0.1%

- Field of View

  Objective and zoom selectable from 0.04 to 16 mm

References

Abbott, B. P., Abbott, R., Abbott, T. D., et al. (2016). Observation of Gravitational Waves from a Binary Black Hole Merger. *Physical review letters, 116*(6), 061102.

Aerotech. (2017). Specifications of ANT130-XY Series Two-Axis XY Direct-Drive Nanopositioning Stages. Retrieved from https://www.aerotech.com/product-catalog/stages/linear-x-y-stages/ant130-xy.aspx [Accessed 11 Feb 2017]

Altan, T., Lilly, B., & Yen, Y. C. (2001). Manufacturing of Dies and Molds. *CIRP Annals - Manufacturing Technology, 50*(2), 404-422.

Ampere, A. T. (2004). Recent Developments in Micromilling Using Focused Ion Beam Technology. *Journal of micromechanics and microengineering, 14*(4), R15.

Araki, T., Hirai, T., & Kyotani, T. (2009). Development of F-Theta Lens for UV Lasers. *SEI Technical Review, 69*, 59-65.

Artigas, R. (2011). Imaging Confocal Microscopy. In *Optical Measurement of Surface Topography*, 237-286.

Bechert, D., Bruse, M., Hage, W., et al. (2000). Fluid Mechanics of Biological Surfaces and Their Technological Application. *Naturwissenschaften, 87*(4), 157-171.

Besl, P. J., & McKay, N. D. (1992a). A Method for Registration of 3-D Shapes. *IEEE Transactions on pattern analysis and machine intelligence, 14*(2), 239-256.

Binnig, G., Quate, C. F., & Gerber, C. (1986). Atomic Force Microscope. *Physical review letters, 56*(9), 930.

Binnig, G., & Rohrer, H. (1982). Scanning Tunneling Microscope. *United States Patent*. Appl. No.: 186,923, Filed: Sep. 12, 1980.

Binnig, G., & Rohrer, H. (1983). Scanning Tunneling Microscopy. *Surface science, 126*(1-3), 236-244.

BIPM (2008). Evaluation of measurement data - Guide to the Expression of Uncertainty in Measurement, GUM 1995 with minor corrections. *Joint Committee for Guides in Metrology, JCGM*.

Blackman, G. S., Mate, C. M., & Philpott, M. R. (1990). Atomic Force Microscope Studies of Lubricant Films on Solid Surfaces. *Vacuum, 41*(4), 1283-1286.

Blunt, L., Bills, P., Jiang, X., et al. (2009). The Role of Tribology and Metrology in the Latest Development of Bio-materials. *Wear, 266*(3-4), 424-431.

Bray, M. (1997). Stitching Interferometer for Large Plano Optics using a Standard Interferometer. *Proceedings of the Optical Science, Engineering and Instrumentation*, Oct 31, San Diego, CA, United States, 39-50, electronic version.

Brinkmann, S., Bodschwinna, H., & Lemke, H.-W. (2001). Accessing Roughness in Three-Dimensions using Gaussian Regression Filtering. *International Journal of Machine Tools and Manufacture, 41*(13), 2153-2161.

Brinksmeier, E., Mutlugünes, Y., Klocke, F., et al. (2010). Ultra-precision Grinding. *CIRP Annals - Manufacturing Technology, 59*(2), 652-671.

Buehring, I. K., & Mansfield, D. (1996). Positional Measurement. *European Patent.* Application number: 92910639.1. Date of filing: 29.05.1992.

Bukkapatnam, S. T. S., & Cheng, C. (2010). Forecasting the Evolution of Nonlinear and Nonstationary Systems using Recurrence-based Local Gaussian Process Models. *Physical Review E, 82*(5), 056206.

Cacace, L. (2009). *An Optical Distance Sensor: Tilt robust differential confocal measurement with mm range and nm uncertainty.* PhD Thesis, Technische Universiteit Eindhoven.

Campbell , F. C. (2011). Manufacturing Technology for Aerospace Structural Materials: Elsevier.

Carl Zeiss Industrial Metrology. (2016). User manual for ZEISS O-INSPECT,. Retrieved from http://www.zeiss.com/ [Accessed 24 July 2016].

Cauchick-Miguel, P. A., & King, T. G. (1998). Factors which Influence CMM Touch Trigger Probe Performance. *International Journal of Machine Tools and Manufacture, 38*(4), 363-374.

Charlton, P., & Blunt, L. (2008). Surface and Form Metrology of Polished "freeform" Biological Surfaces. *Wear, 264*(5), 394-399.

Chen, H., Liu, Y.Y., & Wang, Y. J. (2008). A Novel Image Fusion Method Based on Wavelet Packet Transform. *Proceedings of IEEE International Symposium on Knowledge Acquisition and Modeling Workshop*, Dec 21-22, Huazhong Normal Univeristy, Wuhan, China, 462-465, electronic version.

Chen, H., Sheng, W., Xi, N., et al. (2002). Automated Robot Trajectory Planning for Spray Painting of Free-form Surfaces. Automotive Manufacturing. *IEEE International Conference on Robotics and Automation*, 450-455.

Chen, S. S., Cheung, C. F., Zhao, C. Y., et al. (2016). Simulated and Measured Surface Roughness in High Speed Grinding of Silicon Carbide Wafers. *The International Journal of Advanced Manufacturing Technology*. 1-12.

Chen, S., Li, S., & Dai, Y. (2005). Iterative Algorithm for Subaperture Stitching Interferometry for General Surfaces. *JOSA A, 22*(9), 1929-1936.

Chen, S., Li, S., Dai, Y., et al. (2007). Testing of Large Optical Surfaces with Subaperture Stitching. *Applied optics, 46*(17), 3504-3509.

Chen, S., Xue, S., Dai, Y., et al. (2015). Subaperture Stitching Test of Large Steep Convex Spheres. *Optics Express, 23*(22), 29047-29058.

Cheung, C. F., Hu, K., Jiang, X. Q., et al. (2010). Characterization of Surface Defects in Fast Tool Servo Machining of Microlens Array using a Pattern Recognition and Analysis Method. *Measurement, 43*(9), 1240-1249.

Cheung, C. F., Kong, L. B., Ho, L. T., et al. (2011). Modelling and Simulation of Structure Surface Generation using Computer Controlled Ultra-precision Polishing. *Precision Engineering-Journal of the International Societies for Precision Engineering and Nanotechnology, 35*(4), 574-590.

Cheung, C. F., Kong, L. B., Ren, M. J., et al. (2012). Generalized Form Characterization of Ultra-precision Freeform Surfaces. *CIRP Annals-Manufacturing Technology, 61*(1), 527-530.

Cheung, C. F., Ren, M. J., Kong, L. B., et al. (2014). Modelling and Analysis of Uncertainty in the Form Characterization of Ultra-precision Freeform Surfaces on Coordinate Measuring Machines. *CIRP Annals-Manufacturing Technology, 63*(1), 481-484.

Chiang, Y. M., & Chen, F. L. (1999). Sculptured Surface Reconstruction from CMM Measurement Data by a Software Iterative Approach. *International Journal of production Research, 37*(8), 1679-1695.

Colosimo, B. M., Pacella, M., & Senin, N. (2014). Multisensor Data Fusion via Gaussian process Models for Dimensional and Geometric Verification. *Precision Engineering-Journal of the International Societies for Precision Engineering and Nanotechnology*, 40, 199-213.

Curodeau, A., Sachs, E., & Caldarise, S. (2000). Design and Fabrication of Cast Orthopedic Implants with Freeform Surface Textures from 3-D Printed Ceramic Shell. *Journal of biomedical materials research, 53*(5), 525-535.

de Groot, P. (2011a). Coherence Scanning Interferometry. *Optical Measurement of Surface Topography* (pp. 187-208): Springer.

de Groot, P. (2011b). Phase Shifting Interferometry. *Optical Measurement of Surface Topography* (pp. 167-186): Springer.

de Groot, P. (2015). Principles of Interference Microscopy for the Measurement of Surface Topography. *Advances in Optics and Photonics, 7*(1), 1-65.

Donker, R., Widdershoven, I., & Spaan, H. (2010). ISARA 400: Enabling Ultra-precision Coordinate Metrology for Large Parts. *Proceedings of the 10th International Euspen Conference*, May 31-June 4, Delft University of Technology, the Netherlands, electronic version.

Eigler, D. M., & Schweizer, E. K. (1990). Positioning Single Atoms with a Scanning Tunnelling Microscope. *Nature, 344*(6266), 524-526.

Fang, F. Z., Wu, H., Liu, X., et al. (2003). Fabrication of Micro Grooves. *Proc. of ASPE 18th Annual Meeting*, Portland, USA.

Fang, F. Z., Zhang, X. D., Weckenmann, A., et al. (2013). Manufacturing and Measurement of Freeform Optics. *CIRP Annals - Manufacturing Technology, 62*(2), 823-846.

Fleig, J., Dumas, P., Murphy, P. E., et al. (2003). An Automated Subaperture Stitching Interferometer Workstation for Spherical and Aspherical Surfaces. *Optical Science and Technology, SPIE's 48th Annual Meeting.*

Galetto, M., Mastrogiacomo, L., Maisano, D., et al. (2015). Cooperative Fusion of Distributed Multi-sensor LVM (Large Volume Metrology) Systems. *CIRP Annals - Manufacturing Technology, 64*(1), 483-486.

GF AgieCharmilles. (2015). User's manual for MIKRON HPM 600U/HPM 800U. Retrieved from www.gfac.com [Accessed 12, Oct 2015].

Gonzalez, R. C., Woods, R. E., & Eddins, S. L. (2004). Digital image processing using MATLAB: Pearson Education India.

Gustafsson, F. (1996). Determining the Initial States in Forward-backward Filtering. *Signal Processing, IEEE Transactions on, 44*(4), 988-992.

Hale, L. C. (1999). Principles and Techniques for Designing Precision Machines. PhD Thesis , Massachusetts Institute of Technology, Dept. of Mechanical Engineering.

Hansen, M. O. (2015). *Aerodynamics of wind turbines*: Routledge.

Henselmans, R. (2009). Non-contact measurement machine for freeform optics. PhD Thesis, Technische Universiteit Eindhoven,

Hexagon. (2016). Optiv Classic. Retrieved from http://hexagonmi.com/ [Accessed 24 July 2016].

Hocken, R. J., & Pereira, P. H. (2016). *Coordinate measuring machines and systems*: CRC Press.

Huang, J., Wang, Z., Gao, J., et al. (2016). High-Precision Registration of Point Clouds Based on Sphere Feature Constraints. *Sensors (Basel), 17*(1), 72.

Hucho, W. H., & Sovran, G. (1993). Aerodynamics of Road Vehicles. *Annual Review of Fluid Mechanics, 25*(1), 485-537.

IBS Precision Engineering. (2016). User manual of ISARA400 Next generation ultra-precision coordinate measuring machine.

ISO/TS 17450-1. (2005). Geometrical product specifications (GPS) - General concepts - Part 1: Model for geometrical specification and verification.

Jameson, A. (1989). Computational Aerodynamics for Aircraft Design. *Science(Washington), 245*(4916), 361-371.

Jansen, M., Schellekens, P., & Haitjema, H. (2006). Development of a Double Sided Stitching Interferometer for Wafer Characterization. *CIRP Annals-Manufacturing Technology, 55*(1), 555-558.

JCGM. (2008a). Evaluation of measurement data - Guide to the expression of uncertainty in measurement (GUM). In: The Joint Committee for Guides in Metrology (JCGM), Sevres, France.

JCGM. (2008b). JCGM 101:2008 Evaluation of measurement data - Supplement 1 to the "Guide to the expression of uncertainty in measurement" - Propagation of distributions using a Monte Carlo method.

Jiang, J. B., Cheung, C. F., To, S., et al. (2006). Design and Fabrication of Freeform Reflector for Automotive Headlamp. *Proceedings of International Conference on Power Electronics Systems and Applications*, Nov 12-14, Hong Kong Polytechnic Univ. Hong Kong, China, 220-224, electronic version.

Jiang, J. B., To, S., Lee, W. B., et al. (2010). Optical Design of a Freeform TIR lens for LED Streetlight. *Optik-International Journal for Light and Electron Optics, 121*(19), 1761-1765.

Jiang, X. (2011). In Situ Real-time Measurement for Micro-structured Surfaces. *CIRP Annals-Manufacturing Technology, 60*(1), 563-566.

Jiang, X., Scott, P., & Whitehouse, D. (2007). Freeform Surface Characterisation - A Fresh Strategy. *CIRP Annals - Manufacturing Technology, 56*(1), 553-556.

Jiang, X., Scott, P. J., Whitehouse, D. J., et al. (2007). Paradigm Shifts in Surface Metrology. Part I. Historical Philosophy. *Proceedings of the Royal Society A: Mathematical, Physical and Engineering Sciences, 463*(2085), 2049-2070, electronic version.

Jiang, X., Scott, P. J., Whitehouse, D. J., et al. (2007). Paradigm Shifts in Surface Metrology. Part II. The Current Shift. *Proceedings of the Royal Society A: Mathematical, Physical and Engineering Science, 463*(2085), 2071-2099, electronic version.

Jiang, X., & Whitehouse, D. J. (2012). Technological Shifts in Surface Metrology. *CIRP Annals - Manufacturing Technology, 61*(2), 815-836.

Jin, K. H., Yahng, J. S., Park, C. S., et al. (2014). Telecentric F-theta Lens for High-speed Terahertz Reflection Three-dimensional Imaging. *Proceedings of the 39th International Conference on Infrared, Millimeter, and Terahertz waves (IRMMW-THz)*, Sep 14-19, University of Arizona, Speedway Blvd, Tucson, AZ, USA electronic version.

Ju, B. F., Zhu, W. L., Yang, S., et al. (2014). Scanning Tunneling Microscopy-based in Situ Measurement of Fast Tool Servo-assisted Diamond Turning Micro-structures. *Measurement Science and Technology, 25*(5), 055004.

Jureczko, M., Pawlak, M., & Mężyk, A. (2005). Optimisation of Wind Turbine Blades. *Journal of Materials Processing Technology, 167*(2-3), 463-471.

Katz, J. (2006). Aerodynamics of Race Cars. *Annual Review of Fluid Mechanics, 38*, 27-63.

Komoriya, K., & Oyama, E. (1994). Position Estimation of a Mobile Robot using Optical Fiber Gyroscope (OFG). *Journal of Robotics Society of Japan, 14(4), 532-537.*

Kong, L. B., Cheung, C. F., To, S., et al. (2014). A Theoretical and Experimental Investigation of Design and Slow Tool Servo Machining of Freeform Progressive Addition Lenses (PALs) for Optometric Applications. *International Journal of Advanced Manufacturing Technology, 72*(1-4), 33-40.

Kong, L. B., & Cheung, C. F. (2012). Prediction of Surface Generation in Ultra-precision Raster Milling of Optical Freeform Surfaces using an Integrated Kinematics Error Model. *Advances in Engineering Software, 45*(1), 124-136.

Kong, L. B., Cheung, C. F., To, S., et al. (2013). Modeling and Characterization of Generation of 3D Micro-structured Surfaces with Self-cleaning and Optical Functions. *Optik, 124*(17), 2848-2853.

Lamb, D., Baird, D., & Greenspan, M. A. (2002). An Automation System for Industrial 3-D Laser Digitizing. *Proceedings of the International Conference on 3-D Digital Imaging and Modeling*, Ottawa, Canada, July, 148-157, electronic version.

Latt, W. T., Veluvolu, K. C., & Ang, W. T. (2011). Drift-free Position Estimation of Periodic or Quasi-periodic Motion using Inertial Sensors. *Sensors (Basel), 11*(6), 5931-5951.

Leach, R. K., Jones, C. W., Sherlock, B., et al. (2013). The High Dynamic Range Surface Metrology Challenge. *Proceedings of the 28th Annual Meeting of the American Society for Precision Engineering*, Oct 20-25, St. Paul, Minnesota, USA, electronic version.

Leung, O. M., & Goh, M. C. (1992). Oriental Ordering of Polymers by Atomic Force Microscope Tip-Surface Interaction. *Science, 255*(5040), 64.

Li, L., Raasch, T. W., & Yi, A. Y. (2013). Simulation and Measurement of Optical Aberrations of Injection Molded Progressive Addition Lenses. *Applied optics, 52*(24), 6022-6029.

Liang, C. W., Chang, H. S., Lin, P. C., et al. (2013). Vibration Modulated Subaperture Stitching Interferometry. *Optics Express, 21*(15), 18255-18260.

Liu, M. Y., Cheung, C. F., & Chen, S. S. (2016). A Rotational Stitching Method for Measuring Cylindrical Surfaces. *Proceedings of the euspen's 16th International Conference & Exhibition*, May 30-Jun 3, Nottingham, UK, electronic version.

Liu, M. Y., Cheung, C. F., Cheng, C. H., et al. (2016). A Gaussian Process Data Modelling and Maximum Likelihood Data Fusion Method for Multi-Sensor CMM Measurement of Freeform Surfaces. *Applied Sciences, 6*(12).

Liu, M. Y., Cheung, C. F., Ren, M. J., et al. (2015). Estimation of Measurement Uncertainty Caused by Surface Gradient for a White Light Interferometer. *Applied optics, 54*(29), 8670-8677.

Liu, M. Y., Cheung, C. F., Whitehouse, D. J., et al. (2016). An Autonomous Multisensor in Situ Metrology System for Enabling High Dynamic Range Measurement of 3D Surfaces on Precision Machine Tools. *Measurement Science and Technology, 27*(11), 115015.

LMI Technologies. (2016). User's manual for Gocator 3100 series, all-in-one 3D smart snapshot sensors. Retrieved from http://lmi3d.com/ [Accessed 27 March 2016].

Mahmud, M., Joannic, D., Roy, M., et al. (2011). 3D Part Inspection Path Planning of a Laser Scanner with Control on the Uncertainty. *Computer-Aided Design, 43*(4), 345-355.

Marinello, F., Bariani, P., De Chiffre, L., et al. (2007). Development and Analysis of a Software Tool for Stitching Three-dimensional Surface Topography Data Sets. *Measurement Science & Technology, 18*(5), 1404-1412.

McCarthy, M. B., Brown, S. B., Evenden, A., et al. (2011). NPL Freeform Artefact for Verification of Non-contact Measuring Systems. *Proceedings of the IS&T/SPIE Electronic Imaging conference*, Jan 23-27, San Francisco Airport, California, United States, electronic version.

Metropolis, N. (1987). The Beginning of the Monte Carlo Method. *Los Alamos Science, 15*(584), 125-130.

Miñano, J. C., Benítez, P., & Santamaría, A. (2009). Free-form Optics for Illumination. *Optical Review, 16*(2), 99-102.

Murphy, P., Forbes, G., Fleig, J., et al. (2003). Stitching Interferometry: a Flexible Solution for Surface Metrology. *Optics and Photonics News, 14*(5), 38-43.

Murr, L., Quinones, S., Gaytan, S., et al. (2009). Microstructure and Mechanical Behavior of Ti–6Al–4V Produced by Rapid-layer Manufacturing, for Biomedical Applications. *Journal of the Mechanical Behavior of Biomedical Materials, 2*(1), 20-32.

Nikon Metrology NV. (2016). LK V-GP High accuracy gantry CMM. Retrieved from http://www.nikonmetrology.com/ [Accessed 24 July 2016 2016].

Oh, J. S., Song, C. K., Hwang, J., et al. (2013). An Ultra-precision Lathe for Large-area Micro-Structured Roll Molds. *Journal of the Korean Society for Precision Engineering-Journal of the International Societies for Precision Engineering and Nanotechnology, 30*(12), 1303-1312.

Pavliček, P., & Hýbl, O. (2008). White-light Interferometry on Rough Surfaces--measurement Uncertainty Caused by Surface Roughness. *Applied optics, 47*(16), 2941-2949.

Plummer, W. T. (1982). Unusual Optics of the Polaroid SX-70 Land Camera. *Applied optics, 21*(2), 196-202.

Plummer, W. T. (2005). Free-form Optical Components in Some Early Commercial Products. *Proc. SPIE*, 5865.

Preibisch, S., Saalfeld, S., & Tomancak, P. (2009). Globally Optimal Stitching of Tiled 3D Microscopic Image Acquisitions. *Bioinformatics, 25*(11), 1463-1465.

Qian, P. Z., & Wu, C. J. (2008). Bayesian Hierarchical Modeling for Integrating Low-accuracy and High-accuracy Experiments. *Technometrics, 50*(2), 192-204.

Raol, J. R. (2009). *Multi-Sensor Data Fusion with MATLAB*: CRC Press.

Rasmussen, C. E., & Nickisch, H. (2010). Gaussian Processes for Machine Learning (GPML) Toolbox. *The Journal of Machine Learning Research, 11*, 3011-3015.

Reckzeh, D. (2003). Aerodynamic Design of the High-lift-wing for a Megaliner Aircraft. *Aerospace Science and Technology, 7*(2), 107-119.

Ren, M. J., Cheung, C. F., & Kong, L. B. (2012). A Task Specific Uncertainty Analysis Method for Least-squares-based Form Characterization of Ultra-precision Freeform Surfaces. *Measurement Science & Technology, 23*(5), 054005.

Ren, M. J., Cheung, C. F., Kong, L. B., et al. (2012). Invariant-Feature-Pattern-Based Form Characterization for the Measurement of Ultraprecision Freeform Surfaces. *Ieee Transactions on Instrumentation and Measurement, 61*(4), 963-973.

Renishaw. (2014). TP200 user's guide.

Rusu, R. B., & Cousins, S. (2011). 3D is here: Point Cloud Library (PCL). *Proceedings of the IEEE International Conference on Robotics and Automation (ICRA)*, May 9-13, International Conference Center Shanghai, China, 1-4, electronic version.

Savio, E., & De Chiffre, L. (2002). An Artefact for Traceable Freeform Measurements on Coordinate Measuring Machines. *Precision Engineering-Journal of the International Societies for Precision Engineering and Nanotechnology, 26*(1), 58-68.

Savio, E., De Chiffre, L., & Schmitt, R. (2007). Metrology of Freeform Shaped Parts. *CIRP Annals - Manufacturing Technology, 56*(2), 810-835.

Savio, E., Hansen, H. N., & De Chiffre, L. (2002). Approaches to the Calibration of Freeform Artefacts on Coordinate Measuring Machines. *CIRP Annals-Manufacturing Technology, 51*(1), 433-436.

Schmit, J., Creath, K., & Wyant, J. (2007). Surface Profilers, Multiple Wavelength, and White Light Interferometry. *Optical Shop Testing, 667-755*.

Schreiber, H., & Bruning, J. H. (2006). Phase Shifting Interferometry. *Optical Shop Testing, Third Edition*, 547-666.

Schwenke, H., Wäldele, F., Weiskirch, C., et al. (2001). Opto-tactile Sensor for 2D and 3D Measurement of Small Structures on Coordinate Measuring Machines. *CIRP Annals - Manufacturing Technology, 50*(1), 361-364.

Shen, T. S., & Menq, C. H. (2001). Automatic Camera Calibration for a Multiple-sensor Integrated Coordinate Measurement System. *IEEE Transactions on Robotics & Automation, 17*(4), 502-507.

Shore, P., & Morantz, P. (2012). Ultra-precision: Enabling Our Future. *Philosophical Transactions of the Royal Society of London A: Mathematical, Physical and Engineering Sciences, 370*(1973), 3993-4014.

Stephenson, D. J., Veselovac, D., Manley, S., et al. (2001). Ultra-precision Grinding of Hard Steels. *Precision Engineering-Journal of the International Societies for Precision Engineering and Nanotechnology, 25*(4), 336-345.

Takahashi, K., Kwon, H. N., Saruta, K., et al. (2005). A Two-dimensional F-Theta. Micro Optical Lens Scanner with Electrostatic Comb-drive XY-stage. *IEICE Electronics Express, 2*(21), 542-547.

Takeuchi, H., Yosizumi, K., & Tsutsumi, H. (2004). Ultrahigh Accurate 3-D Profilometer using Atomic Force Probe of Measuring Nanometer. *Proc. of the ASPE Winter Top. Meeting*, 285-286.

Taniguchi, N. (1983). Current Status in, and Future Trends of, Ultraprecision Machining and Ultrafine Materials Processing. *CIRP Annals - Manufacturing Technology, 32*(2), 573-582.

Taylor, H. (2016). User manual for PGI Dimension - A Versatile Automated System for Precision Optics Measurement.

Taylor, J. (1997). An Introduction to Error Analysis, the Study of Uncertainties in Physical Measurements (Vol. 1). Sausalito, CA: University Science Books.

Vasile, M. J., Xie, J., & Nassar, R. (1999). Depth Control of Focused Ion-beam Milling from a Numerical Model of the Sputter Process. *Journal of Vacuum Science & Technology B, 17*(6), 3085-3090.

Veers, P. S., Ashwill, T. D., Sutherland, H. J., et al. (2003). Trends in the Design, Manufacture and Evaluation of Wind Turbine Blades. *Wind Energy, 6*(3), 245-259.

Wang, F., Han, Y., Lim, C. S., et al. (2010). Simultaneous Phase and Size Control of Upconversion Nanocrystals through Lanthanide Doping. *nature, 463*(7284), 1061-1065.

Wang, J., Leach, R. K., & Jiang, X. (2015). Review of the Mathematical Foundations of Data Fusion Techniques in Surface Metrology. *Surface Topography: Metrology and Properties, 3*(2), 023001.

Wang, M. W., & Tseng, C. C. (2009). Analysis and Fabrication of a Prism Film with Roll-to-roll Fabrication Process. *Optics Express, 17*(6), 4718-4725.

Wang, Z., Bukkapatnam, S. T., Kumara, S. R., et al. (2014). Change Detection in Precision Manufacturing Processes under Transient Conditions. *CIRP Annals-Manufacturing Technology, 63*(1), 449-452.

Weckenmann, A., Estler, T., Peggs, G., et al. (2004). Probing Systems in Dimensional Metrology. *CIRP Annals-Manufacturing Technology, 53*(2), 657-684.

Weckenmann, A., Jiang, X., Sommer, K. D., et al. (2009). Multisensor Data Fusion in Dimensional Metrology. *CIRP Annals - Manufacturing Technology, 58*(2), 701-721.

Werth Messtechnik GmbH. (2011). User Manual - DMIS Programming.

Werth Messtechnik GmbH. (2016). User Manual for Werth VideoCheck UA. Retrieved from http://www.werth.de/ [Accessed 24 July 2016].

Widdershoven, I., Donker, R. L., & Spaan, H. A. M. (2011). Realization and Calibration of the "Isara 400" Ultra-precision CMM. *Journal of Physics: Conference Series, 311*(1), 012002.

Wiegmann, A., Stavridis, M., Walzel, M., et al. (2011). Accuracy Evaluation for Sub-aperture Interferometry Measurements of a Synchrotron Mirror using Virtual Experiments. *Precision Engineering-Journal of the International Societies for Precision Engineering and Nanotechnology, 35*(2), 183-190.

Williams, C. K., & Rasmussen, C. E. (2006). Gaussian Processes for Machine Learning (Vol. 2): the MIT Press.

Wozniak, A. (2007). New Method for Testing the Dynamic Performance of CMM Scanning Probes. *IEEE Transactions on Instrumentation and Measurement, 56*(6), 2767-2774.

Wyant, J. C., & Schmit, J. (1998). Large Field of View, High Spatial Resolution, Surface Measurements. *International Journal of Machine Tools and Manufacture, 38*(5), 691-698.

Xia, H., Ding, Y., & Mallick, B. K. (2011). Bayesian Hierarchical Model for Combining Misaligned Two-resolution Metrology Data. *IIE Transactions, 43*(4), 242-258.

Xia, H., Ding, Y., & Wang, J. (2008). Gaussian Process Method for Form Error Assessment using Coordinate Measurements. *IIE Transactions, 40*(10), 931-946.

Xie, X., & Li, S. (2015). Ion Beam Figuring Technology. *Handbook of Manufacturing Engineering and Technology*, 1343-1390.

Yan, J., Zhang, Z., Kuriyagawa, T., et al. (2010). Fabricating Micro-structured Surface by using Single-crystalline Diamond Endmill. *The International Journal of Advanced Manufacturing Technology, 51*(9), 957-964.

Yan, Y., Hu, Z., Zhao, X., et al. (2010). Top‐Down Nanomechanical Machining of Three‐Dimensional Nanostructures by Atomic Force Microscopy. *Small, 6*(6), 724-728.

Yang, P., Ye, S.W., & Peng, Y.F. (2017). Three-dimensional Profile Stitching Measurement for Large Aspheric Surface during Grinding Process with Sub-micron Accuracy. *Precision Engineering-Journal of the International Societies for Precision Engineering and Nanotechnology, 47*, 62-71.

Ye, S.W., Yang, P., & Peng, Y.F. (2016). A Profile Measurement Method of Large Aspheric Optical Surface Based on Optimal Stitching Planning. *Precision Engineering-Journal of the International Societies for Precision Engineering and Nanotechnology, 45*, 90-97.

Yin, Y. H., Ren, M. J., Sun, L. J., et al. (2016). Gaussian Process Based Multi-scale Modelling for Precision Measurement of Complex Surfaces. *CIRP Annals-Manufacturing Technology, 65*(1), 487-490.

Zeeko. (2010). User Manual for On-Machine Stitching Interferometer OMSI for Mounting to a Zeeko IRP Polishing Machine.

ZEISS. (2016). ZEISS XENOS CMM - The Reference. Retrieved from http://www.zeiss.com/metrology/products/systems/bridge-type-cmms/xenos.html [Accessed 18 Oct 2016].

Zhang, G. (1989). A Study on the Abbe Principle and Abbe Error. *CIRP Annals-Manufacturing Technology, 38*(1), 525-528.

Zhang, L., Liu, D., Shi, T., et al. (2015). Aspheric Subaperture Stitching Based on System Modeling. *Optics Express, 23*(15), 19176-19188.

Zhang, Q. L., Zhao, Q. L., To, S., et al. (2016). A Further Study of Wheel Normal Grinding of Hemisphere Couples on TiC-based Cermet. *The International Journal of Advanced Manufacturing Technology*, 1-10.

Zhao, Z., Zhao, H., Gu, F., et al. (2014). Non-null Testing for Aspheric Surfaces using Elliptical Sub-aperture Stitching Technique. *Optics Express, 22*(5), 5512-5521.

Zheng, Z., Hao X., & Liu X. (2009). Freeform Surface Lens for LED Uniform Illumination. *Applied optics, 48*(35), 6627-6634.

Zhu, W.L., Yang, S.Y., Ju, B.F., et al. (2015). On-machine Measurement of a Slow Slide Servo Diamond-machined 3D Microstructure with a Curved Substrate. *Measurement Science and Technology*, 26(7), 075003.